Engine Integration of the Flying V

Quantification of Engine Integration Effects using Wind Tunnel Experiments

S.A. van Empelen

Technische Universiteit Delft

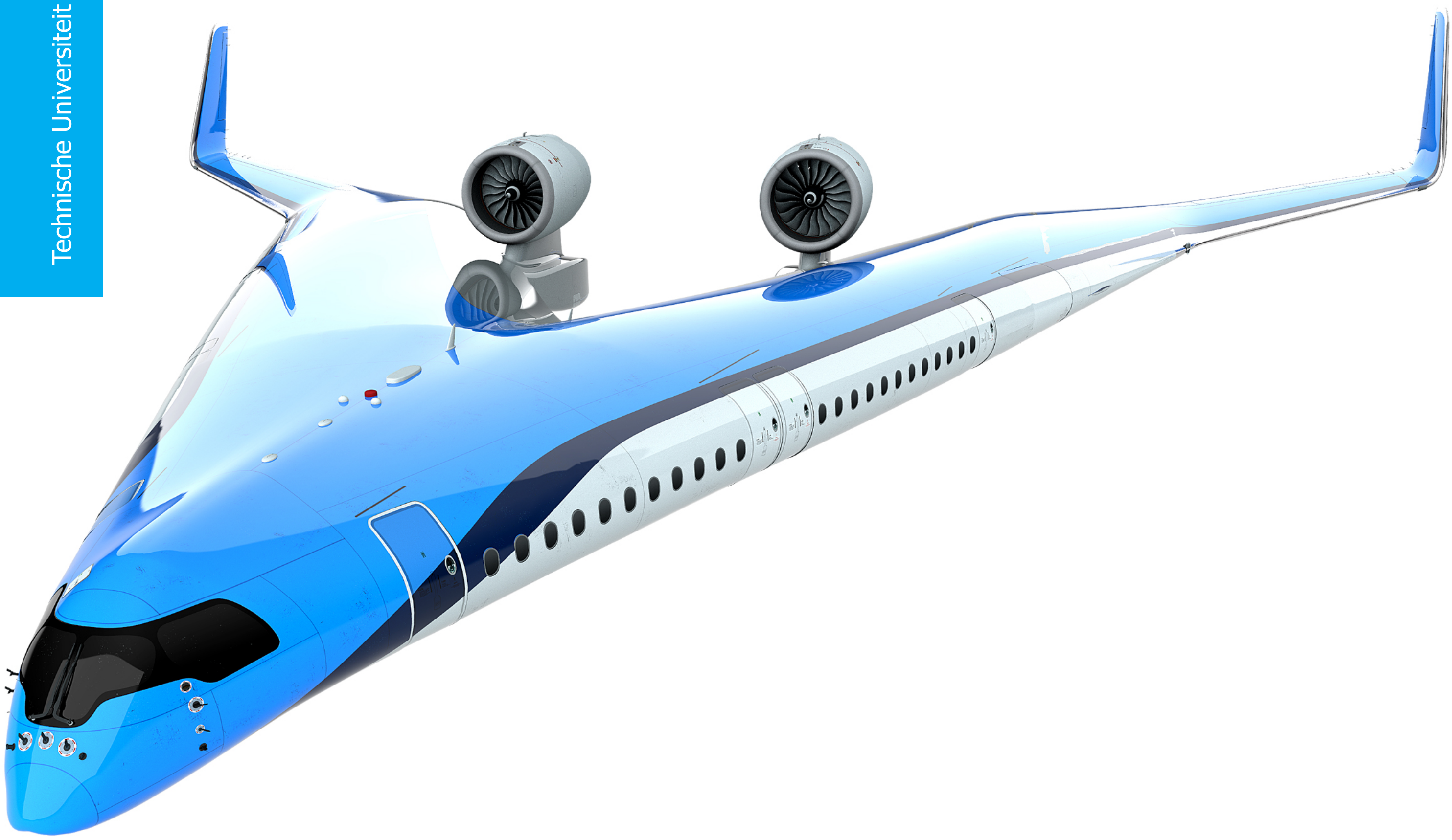

TU Delft
Delft University of Technology
Challenge the future

Engine Integration of the Flying V

Quantification of Engine Integration Effects using Wind Tunnel Experiments

Master Thesis Report

by

S.A. van Empelen

in partial fulfillment of the requirements for the degree of

Master of Science
in Aerospace Engineering

at Delft University of Technology,
to be defended publicly on Tuesday June 2, 2020 at 09:00 AM.

Student Number:	4226844	
Project Duration:	August 2019 - June 2020	
Thesis committee:	Dr. ir. R. Vos,	TU Delft , Supervisor
	Prof. dr. ir. L.L.M. Veldhuis,	TU Delft
	ir. W.A. Timmer,	TU Delft

Delft University of Technology

Abstract

An experimental investigation was done regarding the propulsion and airframe integration issues associated with the novel Flying V configuration. The experimental investigations involved a series of wind tunnel tests with a 4.6% scale half model, conducted in the TU Delft OJF low speed wind tunnel. Balance measurements allowed significant interference effects between the wing and engine to be identified. A nacelle mounted total pressure rake enabled the measurement of engine inlet total pressure, both in TFN and powered conditions.

At landing and take-off velocity ($V = 20m/s$), an interference drag penalty is observed over the full range of positive incidence angles above $5°$, with a maximum of 60 counts (16.5% of isolated wing drag) at an incidence angle of $10°$. At incidence angles lower than $5°$ engine operation is somewhat beneficial, with a maximum contribution to thrust due to interference of approximately 20 counts. Engine inflow is shown to be distorted by the presence of the wing, which could contribute to the observed interference drag. Distortion DC(60) values higher than 0.2 are measured in off design conditions, while measurements at cruise condition show a $DC(60)$ value of 0.08. However, distinguishing between loss of engine thrust and increase in airframe drag is not possible with the used setup. Increased suction around the engine intake contributes to added lift and nose down pitching moment at high thrust setpoints and incidence angles between $5°$ and $12.5°$. An increase in nose up pitching moment is observed from $12.5°$ to $22.5°$.

To put the measured interference in perspective, the direct effects of the quantified interference on trimmed flight conditions are demonstrated. An increased power requirement of up to +8% is observed in trimmed flight conditions between 22m/s and 31m/s, while a maximum reduction of -11% in power requirement is predicted for velocities higher than 32m/s. The change in required control surface deflection for trim due to engine interference is evaluated to be less than $+/-2.5°$ for trimmed level flight. A trimmable flight envelope is demonstrated for maximum climb, level flight and optimum glide with control surface deflections in the range $\delta \in (-10°, 10°)$.

Acknowledgements

With this thesis comes an end to my time at Delft University of Technology. I have enjoyed every step of my journey at the faculty of Aerospace Engineering and have never been happier with my choice of studies.

My thanks go first and foremost to Roelof Vos, for the supervision and support over the past nine months. Thank you for your open and friendly style of coaching. It has been a pleasure to work on such an interesting and relevant project. Credits also to Malcom Brown, Alberto Ruiz Garcia and Daniel Atherstone of the Flying V team. Without their support and experience with the required hardware, this project would not have been possible. A big shoutout also goes to Marco and Jeroen for their time spent helping out in the OJF and sharing of ideas and insights. Your energy has greatly added to the final result.

On a personal note, I would like to thank my girlfriend, family and friends who have supported me over the course of the past nine months. I am very much looking forward to the opportunities that lie ahead!

S.A. van Empelen
Delft, May 2020

Contents

Nomenclature

Abbreviations	
SSFT	Sub-scale Flight Testing
BLI	Boundary Layer Ingestion
CG	Center of Gravity
TFN	Through-flow Nacelle
ESC	Electronic Speed Controller
FW	Flying Wing

Configuration Codes	
W	Wing
N	Nacelle
E	Engine Jet (Power-On)
P	Engine (N and E)
S	Engine Strut

Any combination of the above configuration codes is used to signify the hardware configuration shown in a graph, plot or equation.

Symbol	Definition	Unit
α	Angle of Attack	$[^\circ]$
β	Sideslip angle	$[^\circ]$
ρ	Density	$[kg/m^3]$
μ	Mean value	
s	Sample standard deviation	
σ	Population standard deviation	
δ_0	Mean upwash interference	$[-]$
δ_1	Streamwise gradient of upwash interference	$[-]$
δ_{cs}	Control surface deflection	$[^\circ]$
δ^*	Boundary layer thickness	$[m]$
ν	Fluid kinematic viscosity	$[m^2/s]$
θ	Stream function	$[-]$
A_e	Engine exhaust Area	$[m^2]$
c	Chord length	$[m]$
$\bar{\bar{c}}$	Mean Aerodynamic Chord	$(0.820m)$
$\bar{c}$	Mean Geometric Chord	$(0.820m)$
C	Wind tunnel section Area	$[m^2]$
C_L	Lift coefficient	(L/qS)
C_{L_δ}	Gradient of C_L due to change in δ	$[rad^{-1}]$
C_D	Drag coefficient	(D/qS)
C_M	Pitching moment coefficient	$(M/q\bar{\bar{c}}S)$
C_{M_δ}	Gradient of C_M due to change in δ	$[rad^{-1}]$
C_T	Thrust coefficient	$(T/\rho N^2 D^4)$
D	Propeller Diameter	$[m]$
D	Drag	$[N]$
DC	Distortion Coefficient	$[-]$
$DC(60)$	Distortion Coefficient of a 60 degree sector	$[-]$
F_X	Force in X direction (Body frame)	$[N]$
F_Y	Force in Y direction (Body frame)	$[N]$
F_Z	Force in Z direction (Body frame)	$[N]$
h	Wind tunnel height	$[m]$
H_0	Null Hypothesis	
I	Installation Effect	
If	Interference Effect	
J	Advance ratio	(V/nD)
L	Lift	$[N]$
M_X	Moment around X (Body frame)	$[Nm]$
M_Y	Moment around Y (Body frame)	$[Nm]$
M_Z	Moment around Z (Body frame)	$[Nm]$
M	Mach Number	$[-]$
n	Propeller rotational velocity	$[RPS]$
p_0	Total Pressure	$[Pa]$
p	Static pressure	$[Pa]$
q	Dynamic pressure	$[Pa]$
Re	Reynolds Number	$\rho VL/\mu$
S	Wing Surface Area	$(0.935m^2)$
T_C	Thrust force coefficient	(T/qS)
T	Thrust	$[N]$
u_i	Induced streamwise interference	$[m/s]$
V	Velocity	$[m/s]$
w_i	Induced upwash velocity	$[m/s]$
x_{cg}	CG X position (1.011m from ac nose)	$[m]$

List of Figures

List of Tables

1 Introduction

Non recurring costs of aircraft design are very high, which is one of the reasons to opt for safe and proven design choices. Aircraft configurations of jetliners have therefore remained very similar since the introduction of the Boeing 707, featuring the well-known and understood high aspect ratio wing, horizontal and vertical tail and fuselage body. The historical improvement of $M(L/D)_{max}$ of jetliners shows a trend that is moving towards an asymptote, as depicted in Figure 1.2. Breaking this trend requires the introduction of a concept that is radically different from the tube and wing configuration. Over the past decades many exotic concepts have been proposed, but none have really gained the confidence to generate a breakthrough.[1]

A new take on the flying wing (FW) airplane comes in the form of the Flying V. The concept of the Flying V was first introduced and studied by Benad at Technische Universitat Berlin in collaboration with Airbus [2]. The novel Flying V design minimizes the amount of non-lifting aircraft structure. It consists of two highly swept inner wings with internal cabin structures, outer wings with lower sweep and two large winglets with integrated rudders. Figure 1.1a depicts a render of the original design. Benad made a preliminary estimation of it performance by using the ODILLA vortex lattice method, developed by Airbus. The resulting design is a longitudinally stable Flying V, with an estimated 10% higher L/D compared to an A350-900 in cruise conditions. Moreover, the empty weight is estimated to be 2% lower for an equal wingspan and loading capacity. Finally, no high lift devices are required and engines are shielded from the ground, providing additional benefits to the Flying V concept. The original design was further optimized by Faggiano at Delft University of Technology.[3] Figure 1.1b shows a render of a recent Flying V model in the blue colors of a KLM livery.

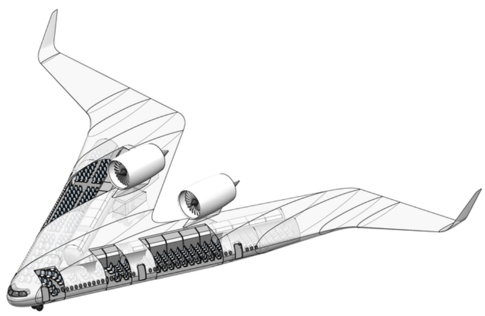

(a) Render of the original Flying V design by J. Benad[1]

(b) A render of the Flying V in KLM livery, parked at the gate[2]

Figure 1.1: Progression of the original Flying V design to the current full scale design by Delft University of Technology

[2]Source: Benad [2]
[2]Source: TU Delft www.tudelft.nl

On a conceptual level flying wing configurations tend to be very attractive.[4] Torenbeek provides a very relevant discussion in his book Advanced Aircraft Design regarding the promises and challenges of Flying Wing aircraft in general. He states that:

> "Advocates of the FW claim its potential of avoiding most of the parasite drag of major components other than the essential wing, thereby obtaining at least 20% gain in the aerodynamic efficiency in one airliner generation. Since the improvement of the range parameter during the jetliner era continues to be very modest (Figure 1.2), the FW should be regarded as an alternative to the traditional general arrangement nicknamed the tube and wing (TAW) configuration that must be considered as a serious challenge. However, in spite of the in-depth research programs between 1990 and 2010, civil airframe manufacturers have not yet embraced the FW layout for their clean sheet designs. Dominant issues that have not yet been solved are (1) how to design a suitable structure for a highly non-cylindrical pressure cabin; (2) how to settle the stability and controllability which have plagued the class of all-wing airplanes; and (3) how to prove that the radical FW concept can pass the certification process successfully. It cannot be excluded that arguments in favour of or against the FW are often based on the superficial suspicion against the introduction of new technology. " – Torenbeek, Advanced Aircraft Design [1]

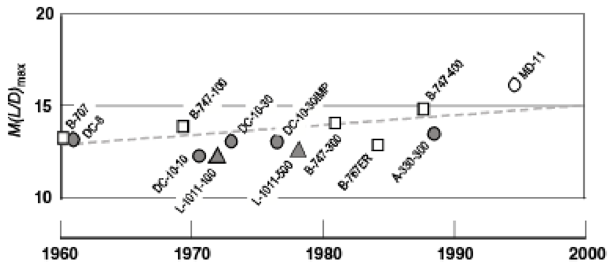

Figure 1.2: Historical LD improvements of jetliners from years 1960 to 2000 [3]

So the gains of a new concept are promising, but there are challenges have to be addressed to make any FW aircraft into a viable concept. These diminish some of the initially envisioned edge a FW aircraft has over conventional designs. When designing a new aircraft for a certain useful volume, and choosing a high subsonic cruise Mach number, the following conclusions can be drawn about any flying wing concept from a low fidelity analysis. First of all, flying wings have less wetted area for a similar useful volume. This is one of the main benefits advocates of FW concepts highlight. The reduction in wetted area should reduce fiction drag of the aircraft to a minimum and therefore result in a significant L/D gain.[4]

Flying wings tend to have a higher wing surface area, leading to a lower wing loading and a lower aspect ratio. This is required, because no trailing edge high lift devices can be incorporated in the design. The lack of any empennage means that the center of pressure the wing coincides with the center of gravity at any trimmed flight condition. Deflection of trailing edge high lift device would result in a large nose down pitching moment, which would have to be trimmed by elevator deflections at the same trailing edge.

Additionally, the lower wing loading results in a higher cruise altitude to reach the CL for optimum L/D or a lower cruise velocity at currently used cruise altitudes. Higher cruise altitude increase the requirements on installed specific thrust. Finally, span loading relieves some of the bending loads on the lifting surface, further reducing weight. This is mostly true for designs that incorporate some outboard loading of the wing.[1] Most of these characteristics can be recognized in the NASA/Boeing joint research into the blended wing body (Figure 1.3a).

[3]Adapted from Torenbeek [1]

(a) The X-48C concept by Boeing and NASA in flight [4]

(b) Photo of the MAVERIC demonstrator model by Airbus [5]

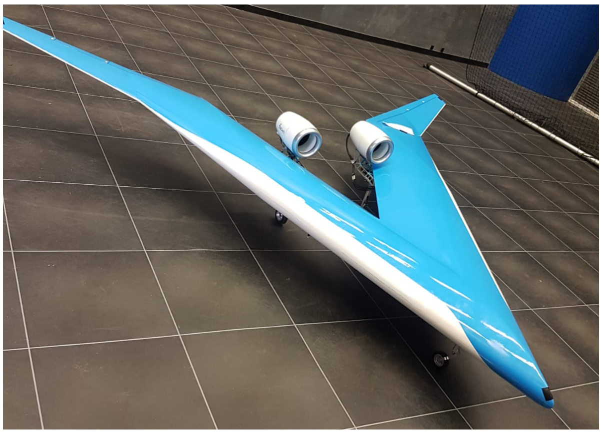

(c) The Flying V SSFT model (without winglets) sitting on the floor of the wind tunnel

Figure 1.3: Pictures of demonstrator models by Airbus, Boeing and Delft University of Technology

A benefit of the Flying V concept is that it tackles structural design of the pressure cabin quite effectively by introducing two oval pressure cabins. The Flying V features a twin fuselage arranged in a V shape, connected at the cockpit. The main benefit of this arrangement is that oval cross sectional tubular fuselages can be used, since they fit a swept back airfoil cross section remarkably efficiently. The oval cross section of these fuselage components allows a relatively simple and light pressure cabin structure to be used when compared to for example a BWB concept.[2][5] Additionally, the Flying V concept makes for easier aircraft family design. Its cabins are relatively straight sections, which can easily be extruded to generate a larger member of the same family.

To aid the acceptance of the Flying V concept, a sub scale flight testing (SSFT) model is built at Delft University of Technology. Flying a demonstrator model is a common method to further investigate a concept. For example, investigations into the blended wing body concept have resulted in the X48 by Boeing (Figure 1.3a) and more recently in the Maveric by Airbus (Figure 1.3b). Figure 1.3c shows a picture of the Flying V SSFT model without its winglets installed. While wind tunnel testing is limited to static measurement conditions, the SSFT model can be used to investigate a wider range of flight characteristics. Some of the objectives of flight testing can be to asses the dynamic interaction of control surfaces, or the control requirements to accommodate asymmetric thrust and to test flight control algorithm designs.[6] Provided that similitude conditions are met, this data can even be valuable to understand the performance of the concept at a larger aircraft scale.[7][8]

[2]Source: Boeing/NASA https://www.nasa.gov/centers/armstrong/multimedia/imagegallery/X-48C/index.html

[5]Photo by Airbus, source: https://www.pilootenvliegtuig.nl/wp-content/uploads/2020/02/MAVERIC-04-1024x611.jpg

To reduce risk and guarantee successful test flights, extensive testing of static conditions in a wind tunnel are required. For example, before the first flight of the X-48 a wide range of tests in the wind tunnel were conducted to investigate the configurations static flight characteristics. These tests included some testing of engine integration, focusing on measurements of flow conditions in the nacelle intake. [9] For the Flying V, wind tunnel tests of the clean wing have been performed to assess the performance, longitudinal static stability and control characteristics of the scaled model. This has resulted in the identification of an aerodynamic model for the clean wing. [3][10][11] However, the effects of engine integration remain untested. While these may result in significant alterations to the flight characteristics of the configuration, integration of the nacelle and engine and their mutual interference have to be investigated.

Research Objective

The scope of this projects is thus to provide further knowledge on the performance of the Flying V SSFT model and enable successful future test flights. The main objective of the specific research can be described as:

> *Quantification of engine integration effects on the Flying V sub-scale flight testing model using wind tunnel experiments.*

The main research question that has to be answered to achieve this purpose is formulated in the following way:

> *How large are the effects of the engine integration on the flight performance characteristics and longitudinal static stability of the Flying V SSFT?*

To enable answering this main question, answers to the following sub questions have to be found:

1. *What are the effects of engine installation on the forces and moments acting on the Flying V SSFT model?*
2. *How large are the interference effects due to the wing, engine nacelle and the engine jet respectively?*
3. *What is the effect of the wing on engine inflow conditions?*
4. *Do the interference between wing and engine result in measurable changes in flight performance characteristics, and if so, what are the effects?*

Thesis Outline

The rest of this work is organized in the following way. First of all, some background information is provided in Chapter 2. This chapter includes some general information regarding the type of engine configuration and expected effects, as well as similar research on which the setup and method are based. The setup and method that were chosen are then described in Chapter 3. Chapter 4 provides verification and validation to show that the obtained results meet requirements for meaningful analysis. The main results are visualized and discussed in Chapter 5. Concluding remarks and a scope of possible further research is given in Chapter 6.

Additional information is given in the appendices. Appendix A visualizes measurement bookkeeping definitions for easier reference. Appendix B provides an overview of the raw measurements to show precision over the measurement domain. Data from the engine electronic speed controller is summarized in Appendix C. Next, an overview of all engine intake measurements is provided in Appendix D. Finally, Appendix E provides an overview of the test matrix; a full overview of all tested conditions.

2

Engine Integration Testing

This Chapter aims to provide the required background theory involved with the engine integration study presented in this work. It provides an overview of the effects that are likely to present themselves in the results. First, Section 2.1 gives a brief overview of the main knowledge that has been gathered during half model testing of the Flying V by Palermo, Viet and Ruiz Garcia. Next, Section 2.2 takes a look at how the propulsion system of the Flying V can be defined, to provide additional insight into the mechanisms of the interaction between engine and airframe. This is divided into a section about the performance characteristics of a ducted fan and some background information about the over-the-wing type engine position. Next, Section 2.2.4 discusses intake measurements, the definition of distortion and their effect of a propulsion system. Finally, Sections 2.3 and 2.4 deal with similar campaigns in industry and wind tunnel corrections respectively.

2.1. Previous Half Model Testing

Studies by Palermo[10], Viet[11] and Ruiz Garcia[12] have focused on identification of characteristics of the clean wing of the Flying V, using the half model that was also tested for this work. To start off, the longitudinal static stability and control characteristics of the Flying V were investigated by Palermo, both numerically and experimentally. Palermo concluded that the configuration's maximum achievable lift coefficient, at which longitudinal stability was achieved, was approximately 0.7 in horizontal steady flight. Figure 2.1 shows pitching moment data for different control surface deflections of the two inboard control surfaces (surfaces one and two), with a reference center of gravity position of $x_{CG} = 1.33m$. Deflection ranges for the inboard (CS1) and outboard (CS2) of these two surfaces are $-10.50°$ to $12.23°$ and $-15.25°$ to $17.85°$ respectively. Control surface effectiveness is clearly relatively constant with angle of attack and linear with control surface deflection. Also, the pitch break around 20 degrees angle of attack remains present, irrespective of control surface deflection δ_{CS}. This imposes a limit on the stable flight regime of the model.[10]

Ruiz Garcia continued the work on aerodynamic model identification and confirmed much of the results by Palermo. The resulting model was used to determine control surface deflections required for trimmed flight conditions. The optimum center of gravity location for the wing was decided to be $x_{CG} = 1.36m$ from the nose of the aircraft, giving the aircraft some longitudinal static stability and maximum deflection of $+/-10°$ required on control surfaces CS1 and CS2 for trim. Finally, the model provided values for the linearized contribution of control surface deflection to lift and pitching moment C_{L_δ} and C_{M_δ}. [12]

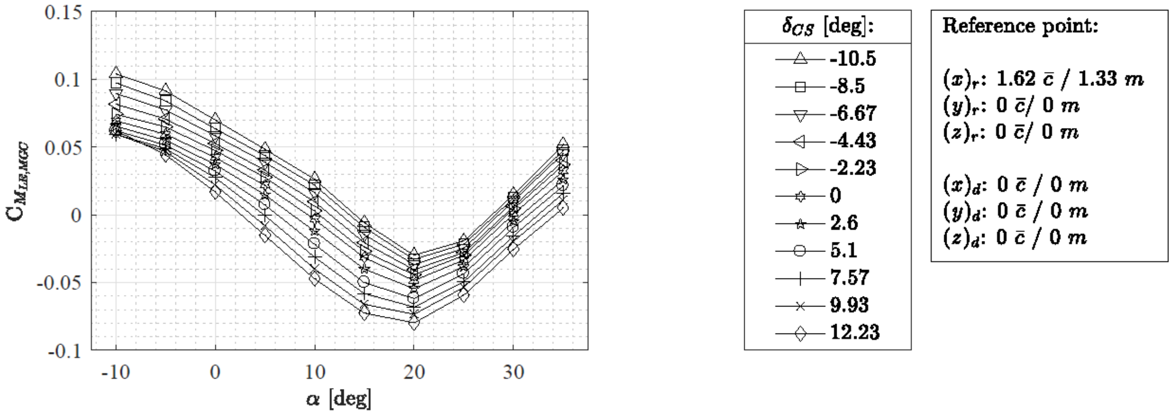

(a) Control surface effectiveness of the most inboard control surface CS_1

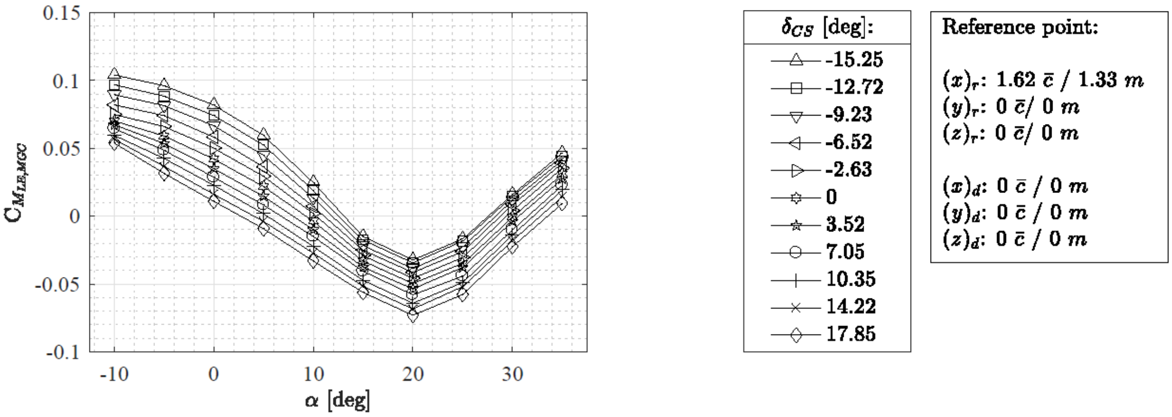

(b) Control surface effectiveness of the center control surface CS_2

Figure 2.1: Pitching moment characteristics of the Flying V wind tunnel half model, for a range of control surface deflections, $x_{CG} = 1.33m$[1]

Viet provided additional wind tunnel data, focusing on flow visualization of the Flying V in high angle of attack conditions. The experimental campaign aimed to map the development of vortex structures on the upper wing upper surface, visualizing them with smoke, tufts and oil flow and aimed find an explanation for the pitch up behaviour of the wing at high angles of incidence. The flow topology drawings of the upper wing surface in Figure 2.2 show how much the nature of the flow on the wing changes with angle of attack. Figure 2.2a shows the surface flow at a moderate $7°$ angle of attack, which is still quite nicely attached. Increasing the incidence angle to $15°$ in Figure 2.2b results in the formation of a trailing edge vortex, and some vortex formation around the leading edge, starting just inboard of the leading edge kink. From the oil flow visualization, Viet concluded that the forward movement of the center of pressure (pitch break) occuring from 20 degrees AoA onwards, can be accounted to the development of a main leading edge vortex (Figure 2.2c). Its starting point moves inboard with increasing angle of attack, increasing the influence the vortex has on the forward part of the inboard wing section. This leads to more lift generated on this section of the wing, and results in a pitch up moment.[11]

The flight envelope for this work is based on the previously recorded behaviour of the Flying V half model. The trimmable flight angle of attack range of the wing at this velocity is limited due to a pitch break at $20°$ AoA. These observations limit the region of interest for integration measurements to an angle of attack range between -5 and 30 degrees. The optimum CG position defined from the spline model representation by Ruiz Garcia ($1.360m$ from the nose of the aircraft) is used as a fixed reference location in the rest of this work. [10][11][12]

[1]Source: Palermo [10]

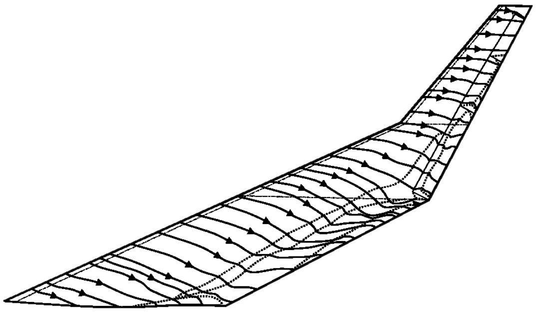

(a) $\alpha = 7^{\circ}$

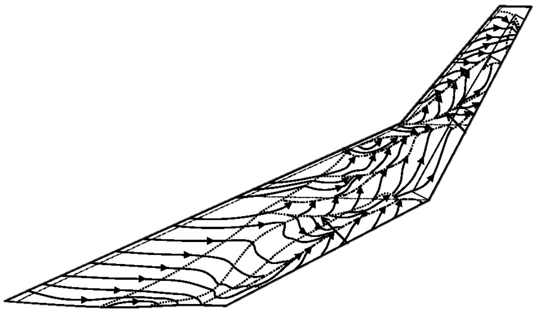

(b) $\alpha = 15^{\circ}$

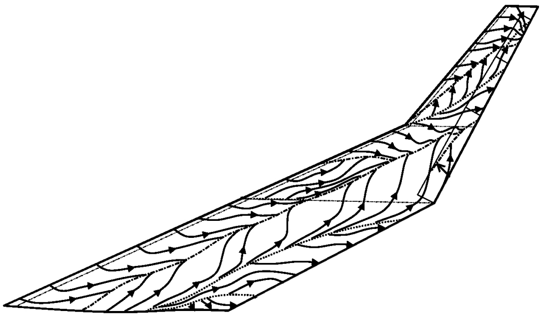

(c) $\alpha = 25^{\circ}$

Figure 2.2: Upper surface flow topology as investigated by Viet using oil flow measurements [2]

2.2. Propulsion System

The propulsion system chosen for the Flying V can be described as an over-the-wing mounted podded engine, with the inlet plane positioned just aft of the local wing chord. In case of the SSFT model, the gas turbine is replaced by an electric ducted fan. This section provides a brief overview of the previous research done on the engine integration of the Flying V concept. Next, some fundamental background information is provided regarding ducted fans. Finally, the main mechanisms that may present themselves in the measured data are discussed.

2.2.1. Previous Study

Engine-airframe integration effects for the full scale Flying V in cruise conditions, have been investigated numerically by Berta Rubio Pascual [13]. For an M = 0.85 cruise velocity at 13000 meters, the aerodynamic performance of forty engine positions were simulated using an Euler pressure-based solver on a three dimensional unstructured grid. This was done with a method similar to physical engine integration testing, with an isolated engine simulation, an isolated airframe simulation and combined simulations to estimate interference levels. Simulation runs were made with the engine simulated both at TFN conditions and with power on conditions. The simulations used a half model representation of the Flying V, with a symmetry plane at the centerline to reduce computational costs.

A region of acceptable engine positions is defined behind the aircraft trailing edge, where interference losses are minimized. Engine positions more forward and above the cabin structure are found to produce supervelocities over the nacelle and airframe structures. The resulting shockwaves on both airframe and cowling result in additional interference drag. The preferred engine position for cruise is depicted in Figure 2.3. It is chosen to be close to the symmetry plane, aft of the inner airframe structure and with the engine centerline only 0.8m above the trailing edge height.

[2]Source: Viet [11]

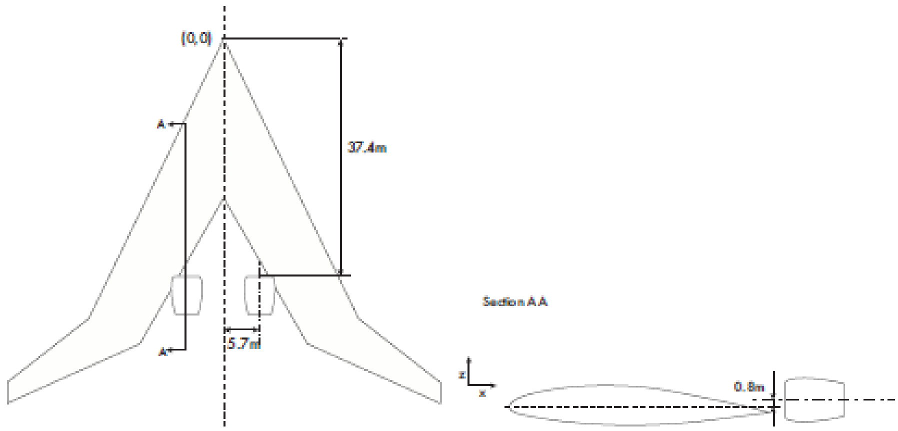

Figure 2.3: Suggested engine position for the Flying V, optimized for transonic cruise conditions [3]

2.2.2. Ducted Fan Performance

Before diving into more configuration specific information, this section discusses the basic characteristics of ducted fans. The addition of the duct around the propeller blades allows the ducted fan to produce significantly higher static thrust than the isolated propeller of equal diameter and power loading. This can be explained by the significantly reduced slipstream contraction downstream of the propeller relative to the isolated propeller, which increases massflow through a ducted fan.[14] The small tip gaps between tips of the fan blade and the wall of the duct, allow the blades to be loaded highly to the end of the blade, reducing tip losses associated with free-air propellers. [15]

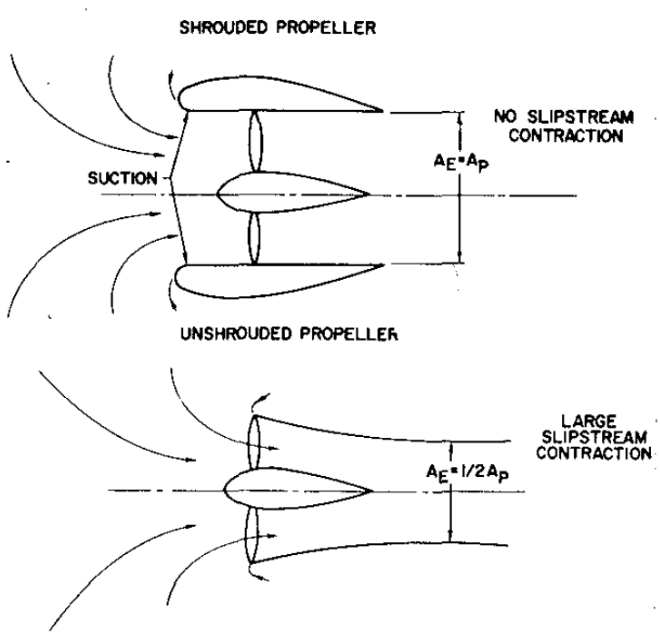

Figure 2.4: Momentum flow field comparison of ducted propeller and unshrouded propeller at static conditions [4]

[3]Source: Rubio Pascual [13]
[4]Source: Black et al. [14]

Figure 2.4 visualizes this effect. In low speed conditions, the increased suction over the forward facing surfaces of the nacelle even induce a forward facing suction, increasing thrust. Because of these effects, the ducted fan diameter required for equal static thrust is only 50%-60% of the equivalent open rotor. The relative increase in performance reduces when flight velocity is increased. The higher initial momentum rapidly reduces the slipstream contraction of the free-air propeller and therefore diminishes the performance gain of the duct. Due to the increased friction of the duct at higher speeds, efficiency even falls below that of the free-air propeller at moderate airspeeds. [14][15]

Drawing a control volume around the ducted fan as depicted in Figure 2.5, allows the derivation of equations for a ducted fan in free stream conditions. [16] The control volume external boundary consists of an inlet plane, outlet plane and a stream tube, while the fan is modeled as an actuator disk. The inlet plane is positioned far enough in front of the propulsion system, such that a uniform inflow velocity V_∞ is present. The external boundary is chosen sufficiently far away from the fan, such that the pressure is equal to the free stream pressure p_∞. Finally, any viscous dissipation due to the friction inside the duct and on the fan are neglected. The outlet plane is depicted as a thick dashed line, on which the jet wake velocity is given as u_j. The outlet pressure of the duct is assumed to be equal to ambient pressure.

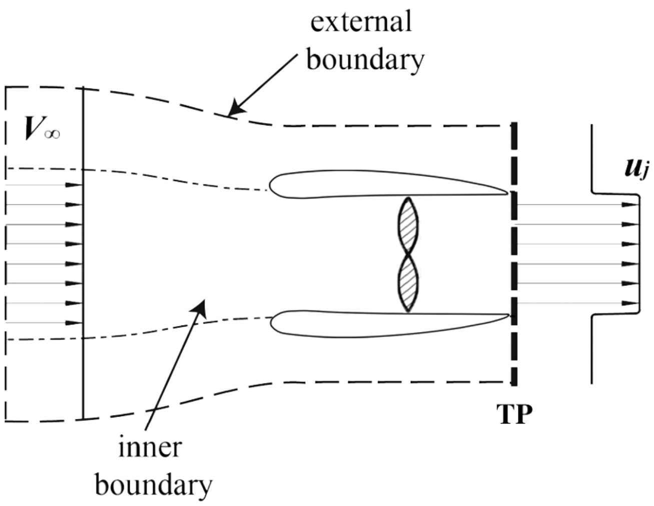

Figure 2.5: Control volume for a free stream ducted fan

The power input to the control volume by the propulsion system (P_{in}) can be expressed as the time rate of change of the kinetic energy difference between the inlet plane and the outlet plane (Equation 2.1). [16]

$$P_{in} = \iint_{TP} \rho u_j \frac{1}{2}(u_j^2 - V_\infty^2) dS \tag{2.1}$$

The thrust (T) generated by the propulsion system is equal to the momentum change between inlet and outlet flow (Equation 2.2). Morover, the rate of kinetic energy ($\dot{E}_{kin,w}$, relative to freestream velocity V_∞) leaving the control volume is given in Equation 2.3. [16]

$$T = \iint_{TP} \rho u_j (u_j - V_\infty) dS \tag{2.2}$$

$$\dot{E}_{kin,w} = \iint_{TP} \rho u_j \frac{1}{2}(u_j - V_\infty)^2 dS \tag{2.3}$$

Finally, the two power output terms (thrust power TV_∞ and time rate of kinetic energy over the exit plane $\dot{E}_{kin,w}$) balance the power input of the actuator (P_{in}). This allows the Froude propulsive efficiency (η_p) to represent the efficiency of the power conversion, in other words the fraction of useful (thrust power) to total input power, as shown in Equation 2.5.[16]

$$P_{in} = TV_\infty + \dot{E}_{kin,w} \tag{2.4}$$

$$\eta_p = \frac{TV_\infty}{P_{in}} = \frac{TV_\infty}{TV_\infty + \dot{E}_{kin,w}} \tag{2.5}$$

Mendenhall and Spangler [17] show how the performance of a ducted fan geometry can be predicted mathematically, provided that no interference with other airframe components is considered. They describe a model consisting of two solutions: an axial flow solution for the fan-duct-centerbody combination and an angle of attack dependent solution for the duct. It estimates blade loading using the blade pitch and geometry, blade element theory, and uses the local variation of blade loading to estimate the shedded vorticity in the wake. Source and sink distributions are used to model the presence of the duct and centerbody. To solve the system of equations requires an iterative solution, which is further deemed outside the scope of this work. What should be noted though, is that the performance of a ducted fan can be modelled relatively accurately by the superposition of an axial solution of the fan-duct-centerbody, and an inflow angle dependent solution for the duct, effectively decoupling the analysis. [17]

Trancossi [18] shows that the inflow and exhaust velocity of small ducted fans can quite accurately be modeled, by simplification of the aforementioned equations and the assumption of incompressible flow. Using the conservation of mass between reference stations in the control volume, the ratio between velocities within the inner boundary of Figure 2.5 can be computed (Eq. 2.6). In this equation A_e is the duct exit surface area, and u_e the average exhaust velocity. A_i and u_i represent the intake area and the intake velocity repectively.

$$\dot{m} = \rho A_e u_e = \rho A_i u_i \tag{2.6}$$

Equation 2.2 can be simplified using the fact that ρ is now a constant over the exhaust plane.

$$T = \dot{m}(u_e - V_\infty) = \rho A_e u_e (u_e - V_\infty) \tag{2.7}$$

Rewriting this equation for u_e allows the computation of exhaust velocity from measured thrust, as shown in Eq. 2.8. Equation 2.6 can finally be used to relate the exhaust velocity to inlet velocity using the ratio of their surface areas.

$$u_e = \frac{V_\infty + \sqrt{(V_\infty^2 + \frac{4T}{(\rho A_e)})}}{2} \tag{2.8}$$

Two dimensional CFD analysis (RANS with a $k-\epsilon$ turbulence model) of a small ducted propeller with a diameter of 56mm (half the diameter of the propeller used in this work) was performed by Trancossi. [18] Disc loading of the propeller analyzed is similar to the propeller used in this work. The results by Trancossi show a maximum difference of 5% in exhaust velocity, between the CFD results and values computed using incompressible flow relations. This validates the assumptions of incompressible flow for the study at hand, and allows the computation of massflow and dynamic pressure from measured thrust and known duct geometry.

Finally, it can be shown that propeller thrust is a function of the following parameters: propeller diameter D, propeller rotational speed n, fluid density ρ, fluid kinematic viscosity ν, fluid bulk elasticity modulus K and free stream velocity V_∞. Dimensional analysis shows that the performance can be rewritten as a function of a couple of dimensionless parameters. In the following analysis, M is a unit of mass, L is a unit of length and T is a unit of time. [19]

$$
\begin{aligned}
& T = f(D;n;\rho;\nu;K;V_\infty) = constant * D^a n^b \rho^c \nu^d K^e {V_\infty}^f \\
& [MLT^{-2}] = [(L)^a (T)^{-b} (ML^{-3})^c (L^2T^{-1})^d (ML^{-}1T^{-2})^e (LT^{-}1)^f] \\
(M) \quad & 1 = c + e \\
(L) \quad & 1 = a - 3c + 2d - e + f \\
(T) \quad & 2 = b + d + 2e + f
\end{aligned}
$$

Rewriting to make everything a function of d,e and f results in the following expression:

$$
\begin{aligned}
& a = 4 - 2e - 2d - f \\
& b = 2 - d - 2e - f \\
& c = 1 - e \\
& T = constant * D^{4-2e-2d-f} n^{2-d-2e-f} \rho^{1-e} \nu^d K^e {V_\infty}^f \\
& T = constant * \rho n^2 D^4 * f\left[\left(\frac{\nu}{D^2 n}\right);\left(\frac{K}{\rho D^2 n^2}\right);\left(\frac{V_\infty}{Dn}\right);\right]
\end{aligned}
$$

In the resulting expression, the first term $\frac{\nu}{D^2 n}$ is proportional to the Reynolds number of the blade: $\frac{1}{Re_{tip}}$. Because $K/\rho = a^2$, the second expression can be rewritten as $\frac{a^2}{D^2 n^2} \propto \frac{1}{{M_{tip}}^2}$ and is thus proportional to the tip mach number of the fan. The final term is better known as the advance ratio of the propeller, $J = \frac{V_\infty}{Dn}$.[19]
Assuming that the effect of Reynolds number and Mach number changes to the blade have a relatively small effect over the range of advance ratios used during the experiment, allows a model for thrust to be constructed that only depends on advance ratio. This observation will be used to model thrust coefficients $T_C = T/q_\infty$ and propeller thrust coefficient $C_T = T/(\rho n^2 D^4)$ for analysis. Rewriting results in the following expressions, with the coefficients a,b,c,d and e to be determined based on measurement results. Note that the variables a-e used here do not correspond to the variables a-f used above.

$$T_C = a * J^{-2} + b * J^2 + c \tag{2.9}$$
$$C_T = d * J + e; \tag{2.10}$$

2.2.3. Effect of engine position

Historically, the engine locations under the wing and to the side of the fuselage have been chosen as the favourite solutions in aircraft design. Placing engines on top of the wing has not been popular option. For transonic aircraft this is mostly due to shockwave formation on the junction of any pylon and the wing upper surface, leading to an increase in wave drag in cruise condition. The main benefits of an over the wing nacelle are the reduced clearance requirements for large bypass ratio engines and the possible reduction of noise perceived on the ground. Engines mounted above the wing have only been used on some aircraft such as the Fokker VFW 615 and the Honda Business Jet and mostly due to special requirements. [20] For example, simulations by Savoni et al. show the high lift capabilities of a short range jetliner with very high bypass ratio engines, where the engine position above the wing is specifically chosen to allow for STOL and relatively low noise.[21] In the case of the Flying V, the engine location above and behind the wing is motivated by center of gravity requirements and the excessive landing gear length required to meet ground clearance requirements for the engine below the wing.

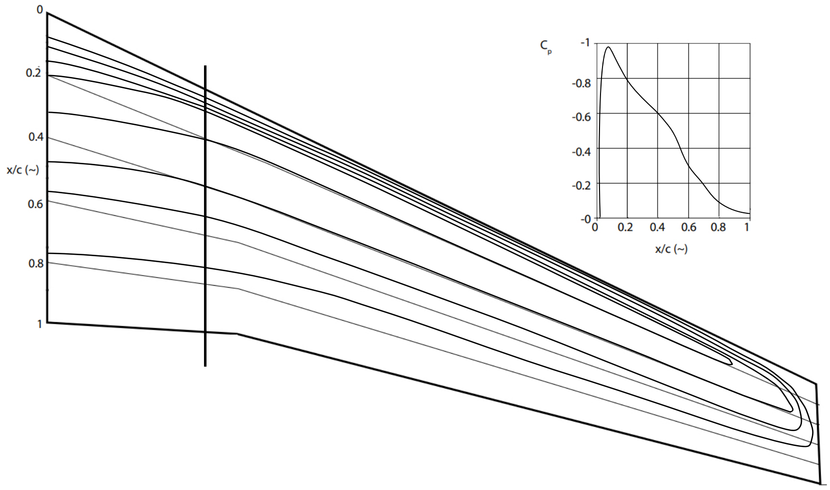

(a) Suction surface pressure distribution of a clean wing

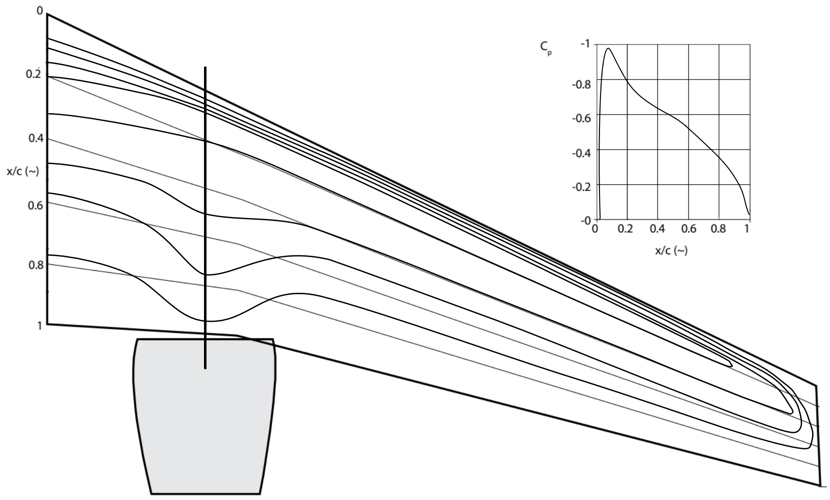

(b) Suction surface pressure distribution of a wing under influence of an over the wing mounted engine, with a capture ratio > 1

Figure 2.6: Notional effect of an over the wing mounted nacelle on surface pressure distribution

To understand the effect of the engine position relative to the wing, some mechanisms that play a role in the interaction between those two elements are discussed. First let us take a look at the effect of the engine on the wing. Figure 2.6 shows how the suction surface pressure distribution may be changed due to thrust for an engine positioned above and behind the wing, with the lower inlet lip close to the wing trailing edge. Figure 2.6a provides a reference pressure distribution on a generic swept wing. The pressure distribution along the chord resembles the simulated chordwise pressure distribution of the clean Flying V wing at the engine spanwise station and 15° angle of attack (Simulated by Palermo [10]). Note that the flow remains attached up to this incidence angle according to the simulation.

Figure 2.6b shows a notional effect of an engine running at a thrust setting with a capture ratio greater than one. The resulting suction of the engine shifts the local pressure distribution, lowering surface pressure close to the engine intake. Effectively, this increases the lift produced locally and reduces the pressure recovery gradient. The improved pressure gradient increases the local margin to stall, allowing the wing section close to the engine to reach a higher angle of attack before the flow separates. Finally, due to most of the additional suction action on the aft part of the wing, pressure drag will also be increased. However, if separation is prevented, the increase in pressure drag will probably still provide a net benefit.

Now let us take a look at another mutual effect of the engine and the wing. The wing boundary layer of the Flying V is assumed to be fully turbulent due to zig-zag tape applied at $0.05c$. Taking the approximate turbulent boundary layer solution of a flat plate as an estimate, gives a very first order estimation for the boundary layer thickness at the wing/engine interface. The Reynolds number is taken as $Re = 1 * 10^6$ and the flat plate length x is taken as the approximate local chord length of 1m. In the following, Re_δ is the Reynolds number based on the boundary layer thickness and δ^* is the boundary layer thickness. [22]

$$Re_x = 10^6$$
$$x = 1m$$
$$Re_\delta \approx 0.16 Re_x^{\frac{6}{7}}$$
$$\delta^* \approx 2.5cm$$

The flat plate boundary layer thickness under the assumed conditions is $2.1cm$. Under less favorable pressure gradients the boundary layer thickness will grow more rapidly, possibly even detaching from the surface. With a minimum distance of $1.7cm$ between the nacelle and the wing surface, it is therefore very likely that the engine will ingest (some) low momentum flow originating from the wing surface at higher angles of attack.

Testing by Sabo and Drela suggests that boundary layer ingestion can significantly reduce the amount of power required for a given amount of thrust. This is accounted to the more efficient propulsion resulting from the acceleration of lower momentum flow and the reduction in strength of the low momentum wake leaving the airframe. The setup used to investigate the effect involved an electrically powered ducted fan and a NACA 0020 revolving body. Power savings of up to 25% were found for this non lifting body at engine positions situated closely behind the body.[23]

A very similar, more fundamental explanation is given by Lv et al.[16] and later by Hall et al. [24]. In these works the the benefit of using wake ingestion is explained using a power balance method. Imagine the wake of a wing entering the control volume of Figure 2.5. Ideally, the thrust of the propulsor just fills the wake of the wing to produce the thrust required, resulting in a velocity $u_j = V_\infty$. For a more general case, the required thrust can be produced with a lower exhaust velocity, reducing the amount of kinetic energy lost in the exhaust jet. However, the positioning of the engine could also induce some additional drag. In the numerical investigation done by Lv et al., profile drag increased significantly under the influence of a closely coupled propulsions system. The main source was an increase in pressure drag, but also due to increased friction drag. As depicted in Figure 2.7, under suction the boundary layer shape changes, resulting in an increased friction drag. [16]

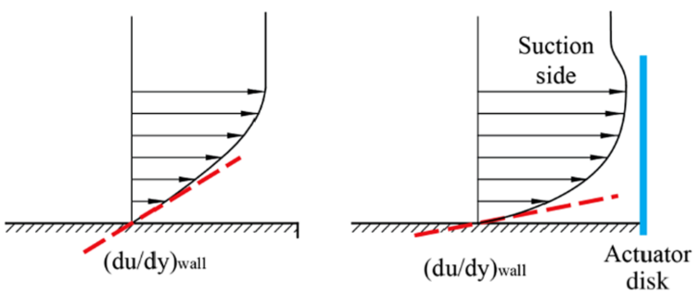

Figure 2.7: Change of friction drag under the influence of an actuator [5]

[5]Source: Lv et al. [16]

2.2.4. Inlet Conditions

While the engine has its effects on the performance of the wing, the wing also affects the conditions in which the engine operates. The flow surrounding the engine is altered, changing the inflow angle of the engine and the condition of the air in the intake. In an ideal world, the effect of the wing on the engine inflow is small, as is well described by the quote below.

While the positive effects of wake ingestion may look promising, the effect of non-uniform inflow on the propulsor is not taken into account in most research. A distorted inflow may have detrimental effects on fan performance in the propulsor. For example, boundary layer ingestion was first seen as possible positive effect by Boeing for their BWB program. However, the initial BLI design was later changed to a regular podded over the wing engine due to unacceptable drag penalties incurred by the required boundary layer bleed, when engine performance was taken into account. [25] Wind tunnel tests of a scale model in 2016 show the podded engines that was chosen over any researched boundary layer ingestion designs for which the results were published in 2006.[26][27]

> "The ideal intake delivers a total pressure field at the engine face that is not only high in terms of its average value, but is also uniform. Although a low average (low pressure recovery) can reduce thrust and often efficiency, distortions in the pressure field can lead to fan and compressor blade fatigue, can reduce the surge margin of highly loaded sections of the compressor, and often also increase noise." - Sobester, Tradeoffs in Jet Inlet Design: A Historical Perspective [28]

Looking at distortion from a blade element theory point of view gives some more insight of the effect of distortion on the fan (Figure 2.8a). For a blade element spinning with a rotational velocity ω at distance r from the axis of rotation, the angular velocity is ωr. The effective angle of attack α of this blade element depends on its pitch B, the inflow velocity V and any induced angle of attack α_i due to the rest of the lifting blade. Any change in inflow velocity δV will directly affect the effective angle of attack of this blade element, altering its contributions dT and dF to the thrust produced and torque required respectively. A reduction of inflow velocity will increase α for a given rotational velocity, thereby probably increasing dF. Depending on the stall margin of the blade, thrust may be gained or lost. However, assuming that the blade was operating in optimum design conditions, any alteration to α will lead to a decrease in efficiency.

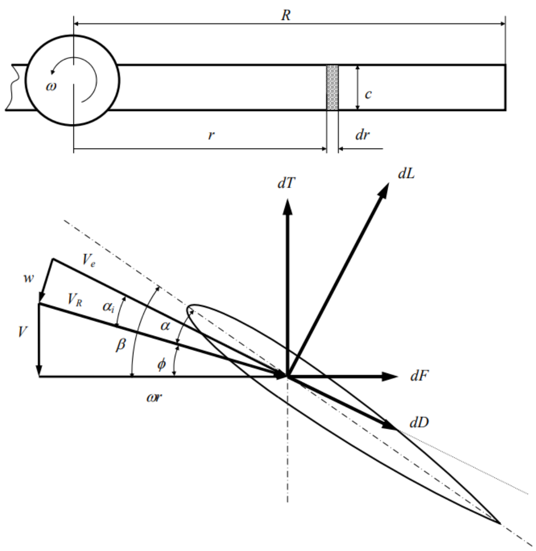

(a) Schematic of blade element theory [6]

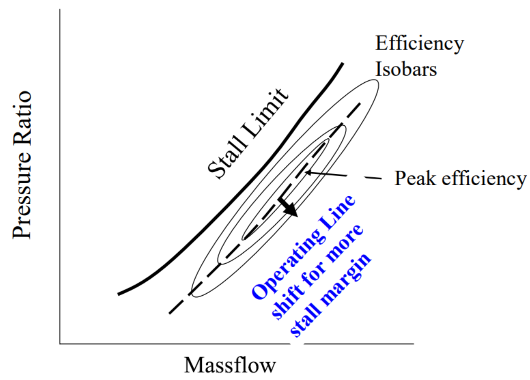

(b) Efficiency loss resulting from engine inlet distortion [7]

Figure 2.8: The effect of inflow distortion on the operating point of the fan

[6] Source: Cavcar [29]
[7] Source: Kawai et al.[27]

This conclusion is also reached when looking at the propeller as a very low pressure ratio compressor. Figure 2.8b shows a generic compressor map. A reduction in inlet velocity will locally move the operating point closer to the stall limit of the blade section, reducing the stall margin. Also, while the dashed operating line is drawn at the highest efficiency, any shift will result in a lower than optimum operating efficiency. For significant distortion, part of the fan disk may stall. Local pockets of distortion will also lead to cyclic loading of the blades, leading to fatigue.[28]

Two types of distortion are mostly tested: total pressure distortion and swirl distortion. Total pressure distortion is defined as the loss of total pressure on the measurement plane and swirl distortion as the offset in inflow angle. An engines resistance to distortion can be tested using a specially designed screen that generates a known amount of distortion at the engine inlet. [30] Total pressure distortion can be measured using a relatively simple rake. Swirl distortion requires a more complex rake featuring directional pressure probes to capture flow direction. [9][26][31].

$$C_{p_0} = \frac{p_0}{p_{0_\infty}} \tag{2.11}$$

$$DC = \frac{(p_{0_\infty} - p_0)}{\bar{q}} \tag{2.12}$$

$$DC(60) = \frac{(\bar{p_0} - \bar{p}_{0_{(60)}})}{\bar{q}} \tag{2.13}$$

Three definitions are used to describe the total pressure distortion measured in this work. The total pressure recovery is described as the fraction of local total pressure and free stream total pressure C_{p_0} (Eq. 2.11). The local distortion is plotted as the difference between the total pressure in free stream and local total pressure, over the local dynamic pressure DC (Eq. 2.12). Finally, the average distortion over a 60 degree arc $DC(60)$ is used to judge radial distortion on the intake. Its definition in Equation 2.13 shows that instead of the free stream total pressure, the average total pressure on the plane is used as a reference. Therefore, this definition of $DC(60)$ may be low even while all of the inlet plane receives a lower than free stream total pressure flow. Rather, it provides a value for the difference between the $60°$ sector and the average in the plane, as seen in Figure 2.9, which provides an indication whether the blade will suffer from fatigue or not. [32] To reduce the cyclic loading of the blade, many new boundary layer ingestion designs opt for an engine positioned in a central location at the end of the fuselage, resulting in a low radial distortion while ingestion the boundary layer. [33]

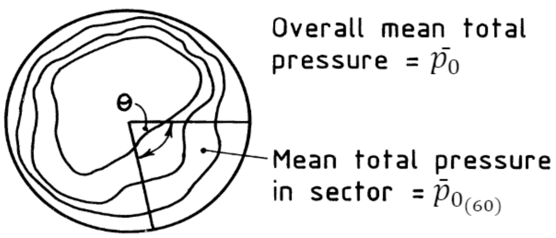

Figure 2.9: Graphic representation of the definition of $DC(60)$[8]

Concluding the previous two sections, it depends on the combination of geometry, propulsor and condition under investigation whether the net effect of the interaction between wing and propulsor provides a positive or negative performance result. Wake ingestion may result in a reduced power required to generate thrust, however increases in pressure and friction drag diminish some of the benefit. Also, if the energy conversion of the propulsor is reduced due to distortion, the net result is even less favourable.

[8]Source: Seddon and Goldsmith[32]

2.3. Similar Campaign

Engine integration research is more often conducted to investigate transonic flight conditions than low speed flight conditions. However, similar low-speed research has been conducted on a blended wing body configuration at NASA. For the NASA Environmentally Responsible Aviation (ERA) project, a low speed campaign was done in the NFAC 40x80ft wind tunnel, to investigate overall performance of a 5.75% scaled model of Boeing's Preferred System Concept (PSC) Blended Wing Body aircraft. This model had a wingspan of 4.0 meters and testing was done at Reynolds numbers varying between $Re = 2.2 * 10^6$ $(28m/s)$ and $Re = 5.5 * 10^6$ $(70m/s)$. A photo of the setup is shown in Figure 2.10a. [9][26]

The campaign had three objectives. The main goal of the campaign was to demonstrate engine operability at low speed design and off-design conditions, characterizing the adverse propulsion airframe induced inlet flow distortion. The second was to aid the development of a leading edge Kruger flap, to achieve higher maximum lift coefficients. The third goal was to quantify power-on effects to increase pitching moment and allow take off rotation. This shows that the comparable aircraft class and engine positioning of the BWB design results in challenges similar to the challenges for the Flying V concept. The engine testing procedure for the BWB model was divided into three phases; a flow-through nacelle inlet test, an ejector powered nacelle inlet test, and a turbine powered simulator (TPS) test. The purpose of the flow-through nacelle and ejector powered engine phases was to map inlet distortion due to engine airframe interaction, both in terms of total pressure and swirl. Turbine powered tests were used to quantify the power-on integration effects. Mapping inlet distortion with a TPS test is not possible, due to the discrepancy in inlet massflow between the actual engine and the TPS.[9][26]

Total pressure distortion is relatively easy and cheap to measure. The standard SAE-ARP-1420-B provides guidelines on the measurement equipment required.[31] It describes a 40 pressure probe rake with eight arms featuring five probes each. The arms are spaced at $45°$ intervals on the inlet, with the probes spaced to provide equal area distribution per probe along the length of the arm. The inlet measurements by NASA featured such a 40 probe rake design, which is shown in Figure 2.10b.

(a) Photo of the NASA/Boeing BWB design in the NFAC 40x80 Foot wind tunnel [9]

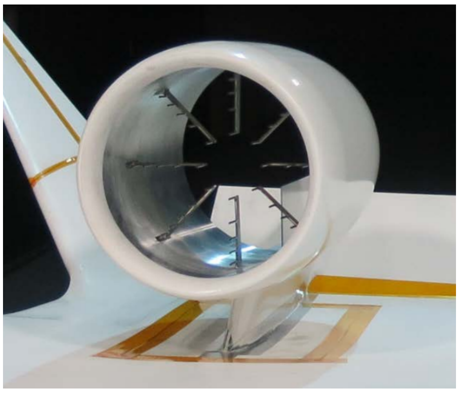

(b) Inlet total pressure probe rake on the NASA ERA BWB wind tunnel model [10]

Figure 2.10: Photos of the instrumentation and setup used to test a 5.75% BWB scale model by NASA

Swirl distortion measurements requires more complex equipment: either a rake with five hole directional probes, or a traversing system capable of spanning the whole inlet area with (multiple) probe(s) and with minimal intrusive interference. In the NASA BWB test, the right ejector powered nacelle featured a special three arm swirl rake, capable of measuring the direction of the incoming flow, with five hole pressure probes. The rake had the ability to rotate over 120 degrees with 15 degree increments, providing a total of 120 measurement points with 5 probes per arm and three arms. [26] [34][35]
Results from the flow-through inlet distortion measurements phase of the campaign are shown in Figure 2.11 below. Note that the exact values for α and β are not provided, though the general idea is clear.

[9]Adapted from Dickey et al.[26]
[10]Source: Dickey et al. [26]

The engine inlet of the BWB design suffers from low energy inflow due to engine airframe interaction at a combination of high incidence angles and sideslip. Notably, the effect of sideslip is quite large in this respect. Unfortunately, testing different angles of sideslip is not possible with the half model setup used in this work.[21]

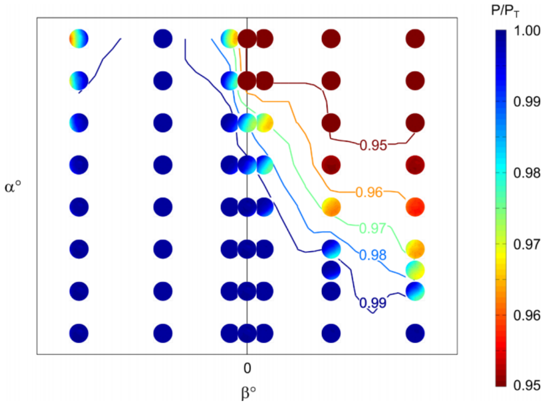

Figure 2.11: Total pressure inlet results for the NASA/Boeing BWB wind tunnel test [11]

2.3.1. Bookkeeping Method

Most facilities offering propulsion system integration testing use turbine powered simulators to quantify these effects. Most of the TPS testing is aimed towards high speed integration effects. Most of these effects are compressibility and shock wave related and are not expected to show up at low speed, large angle of attack flight. Major research institutions that published about engine integration studies done at their facilities include DLR[36][37], the German-Dutch Wind Tunnels [38][39] and Aircraft Research Association Limited in Bedford England (ARA)[40] and ONERA in France [41]. While the integration effects presented in these works do not exactly match low speed testing effects, the thrust/drag accounting methods are very relevant as a reference for this work.

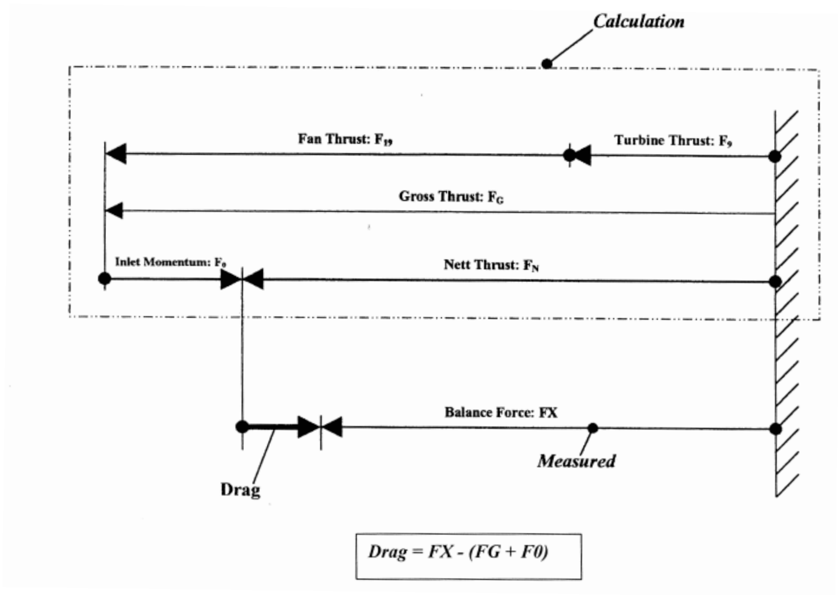

Figure 2.12: Schematic of Thrust-Drag accounting for turbine powered wind tunnel testing [12]

[11] Source: Vicroy et al.[9]
[12] Source: Campomanes [42]

General features of aerodynamic interference can be split up into geometry effects and the power effects, which can be measured separately. Both of them affect the flow around the aircraft, however they might be more easily understood when split up. This is where testing with a TFN (or at idle power setpoint) comes in. It allows the pure geometry effects to be investigated and visualized before the addition of thrust. [38]

The bookkeeping method that allows high accuracy in TPS testing revolves around isolated calibration of the engine beforehand. In the calibration setup, internal flow of the TPS unit is recorded at simulated combination of power setpoint and Mach numbers, using a vacuum chamber on the TPS outlet to statically create the required pressure difference between inlet and outlet planes. This isolated calibration procedure allows nacelle flow correction coefficients to be determined, which are used to correct thrust in wing-on conditions. During wing-on testing, the nacelle is mounted directly to the wing. However, using internal measurements of pressure and total temperature, the engine produced thrust can accurately be determined based on isentropic flow calculations and the previously determined correction coefficients. This allows all the different acting forces to be specified, including a distinction between fan thrust, turbine thrust and inlet momentum. A schematic of such a thrust drag bookkeeping scheme is depicted in Figure 2.12.[37][38][40]

A suitable approach to an experimental engine integration study for the Flying V is a simplified version of the methods described. Since no separate engine balance, nor internal pressure and total temperature probes are included in the setup, the most basic form of thrust/drag bookkeeping method is used for this campaign. Forces are recorded for all component combinations, in all test conditions. This lead to the bookkeeping scheme definitions that are visualized in Appendix A. [42] The chosen method is limited in the sense that no distinction can be made between a loss of thrust and an increase in drag, though it is deemed sufficient to achieve the purpose of this investigation.

2.4. Wind Tunnel Corrections

Normally, the full scale aircraft under investigation operate at a much higher Reynolds number than could ever be achieved in a wind tunnel. Some tunnels provide cryogenic or pressurized conditions to try and close the gap as much as possible, but actual flight Reynolds numbers are still not achieved. However, when investigating the characteristics of an SSFT model we are in the favourable situation of exactly matching Reynolds numbers and length scales. [43] Nevertheless, measurements of a lifting surface in a wind tunnel result in different results than would be obtained from the same geometry in open air. The effect is nicely described by a quote from Barlow et al. below.

> "Very early in the century experimenters using open throat wind tunnels found their tunnels giving very pessimistic results. The measured minimum drag and rate of change of drag with lift were too large, and the slope of the lift curve was too small. The minimum-drag effect was largely due to the very low Reynolds numbers then found in low-speed tunnels, but the other two effects were due to the tunnel boundaries." – Barlow et al. p. 377 [43]

The effect of the finite tunnel size on wind tunnel measurements has to be accounted for to get a better idea of aircraft performance in free flight conditions. Both the classical corrections for open sections documented in AGARDograph 109 [44] and Chapter 2 of AGARDograph 336 [45], as well as a new method of correction by Horsten and Veldhuis [46] based on a vortex lattice code are used to make a basic estimation of the wing performance in free flight. The respective procedures are described in Sections 2.4.1 and 2.4.2. As will become clear, the corrections only hold some value at low to moderate incidence angles. Moreover, secondary effects such as engine effects are not considered in the following corrections.

2.4.1. Conventional Corrections

Conventional primary wind tunnel corrections for open test sections include a lift interference correction and a blockage correction. The nature of these corrections are based on the assumptions of linear potential flow, perturbation flow at the tunnel boundaries, a small model with respect to the size of the tunnel and a tunnel with constant cross section extending far upstream and downstream of the model and with either no flow normal to the wall (closed section) or a constant pressure at the boundary location (open section). [43][44][45] As long as the region between the tunnel boundary is large enough, both the effect of the model on the boundary and the effect of the boundary on the model can me modelled as perturbations.

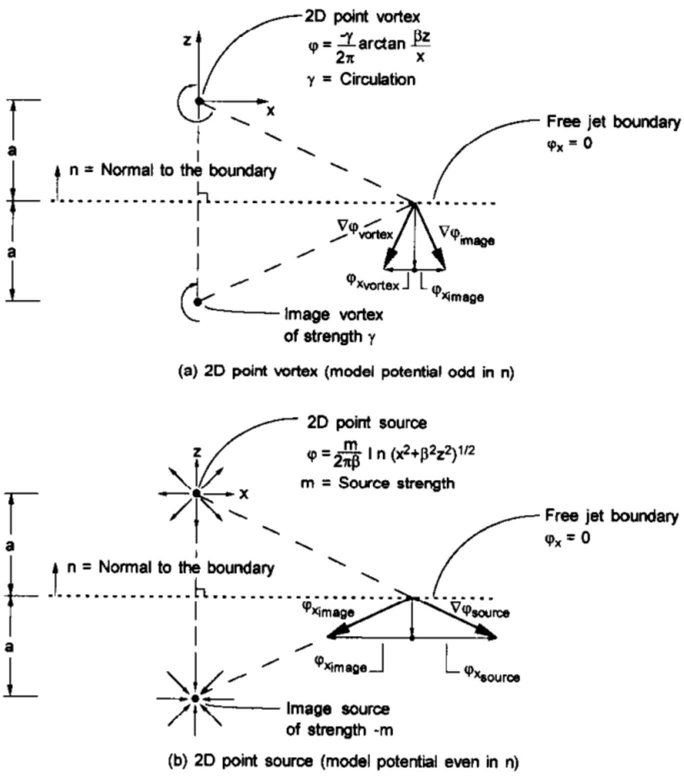

Figure 2.13: Method of images for an open jet wind tunnel boundary [13]

As mentioned, the boundary condition of an open jet wind tunnel is defined as zero pressure gradient in streamwise direction at the jet boundary, as given in Equation 2.14.[45] Combined with the assumption that the boundary extends with constant cross section to infinity upstream and downstream, this allows an infinite set of images to be used to approximate the effect of the boundary on the flow inside the test section. The method of images for an open jet tunnel is shown in Figure 2.13. The figure shows that the effect of the boundary can be modeled as a set of image vortices, sources and sinks, which mirror the effect of the object in the test section to cancel each other at the boundary.

$$\frac{\delta \phi}{\delta x} = 0 \tag{2.14}$$

[13]Source: AGARDograph 336 [45]

Corrections due to lift

The main corrections required are a direct effect of the lift generated by the wing. Representing the wing as a finite span horseshoe vortex provides an approximation of the effect of finite wingspan, assuming a small enough wing. For an open jet, its image vortices can be seen to produce a lower apparent angle of attack at the center of lift. Additionally the trailing vortex images create a slight upwash before the lifting body and a downwash behind it. The resulting curvature of the flow streamlines introduces an apparent negative camber to the airfoil in an open jet flow. Thus, for a lifting body, the moment coefficient, lift and observed angle of attack are decreased in an open jet wind tunnel. Or in other words, the geometric angle of attack in the tunnel is larger than the corresponding angle of attack in free flight. To arrive at the corrections for the half model setup, the equivalent reflected setup shown in Figure 2.14 is treated. In the reflected setup, the small center fillets are ignored to form the octagon in the figure below. According to Agard 109, this should not be a problem for any first order corrections. [44]

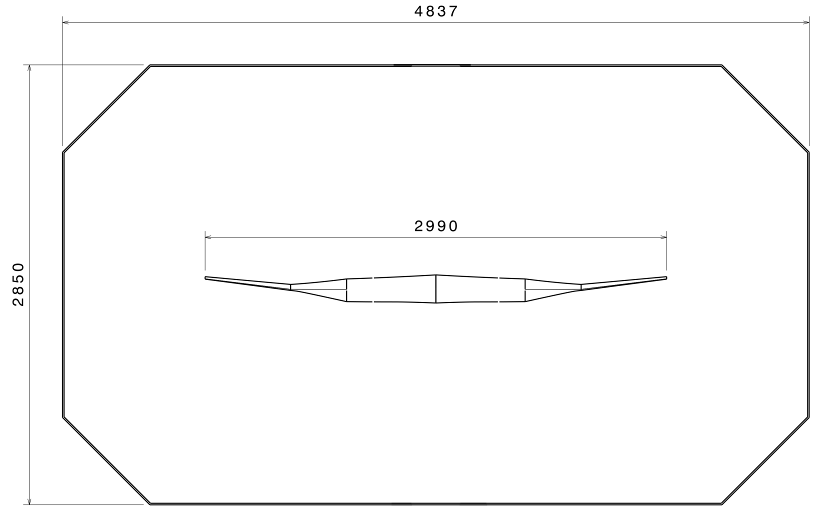

Figure 2.14: Reflected setup of the half model for wind tunnel correction

For analysis, the upwash interference is commonly non-dimensionalized as the upwash interference parameter δ, defined below (Eq. 2.16, 2.17). In this definition C represents the wind tunnel cross sectional area of the reflected setup and S the reference wing surface area. [43] The streamwise gradient of the upwash interference parameter is most commonly denoted as δ_1. In its definition below, β is the compressibility correction factor ($\beta^2 = 1 - M^2$)), and h the reference length tunnel height. Empirical values for δ_0 and δ_1 can be found in the graphs from Agard 109 and Agard 339 depicted on the next page.[44][45]

$$\Delta\alpha = \frac{w_i}{V_\infty} \tag{2.15}$$

$$\delta_0 = \Delta\alpha\frac{C}{SC_L} \tag{2.16}$$

$$\delta_1 = \frac{\partial\delta}{\partial\left(\frac{x}{\beta h}\right)} \tag{2.17}$$

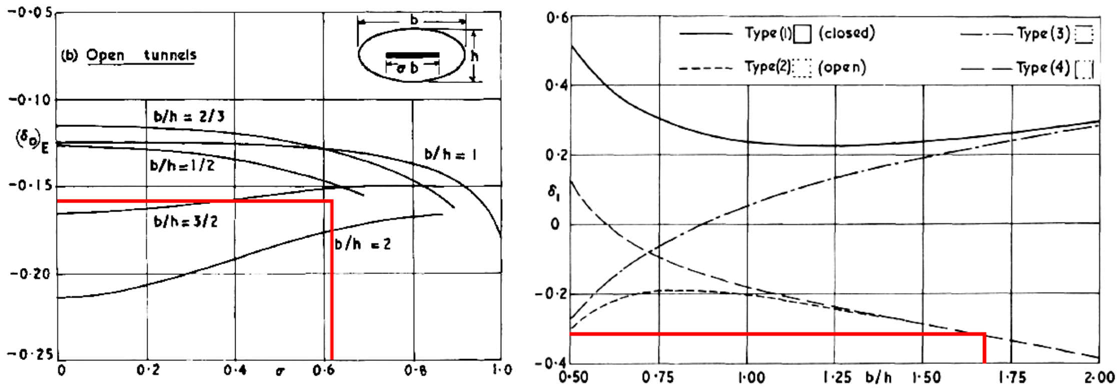

(a) Downwash interference parameter δ_0 for elliptically loaded wings in elliptical open test sections [14]

(b) Streamwise interference parameter δ_1 for open test sections [15]

Figure 2.15: Interference parameters δ_0 and δ_1 as estimated from literature

The resulting values for δ_0 and δ_1 are estimated to be:

$$\delta_0 = -0.16, \qquad \delta_1 = -0.3$$

Primary corrections for the offset in angle of attack result in a corrected effective angle of attack and drag coefficient. When assuming small correction to effective angle of attack, this results in the following correction formulas. In the following, the subscripts $_{corr}$ and $_{unc}$ denote the corrected and uncorrected data respectively and δ_0 is the average upwash interference of the planform.[44] [45]

$$C_{L_{corr}} = C_{L_{unc}} \cos\Delta\alpha - C_{D_{unc}} \sin\Delta\alpha \approx C_{L_{unc}} \tag{2.18}$$
$$C_{D_{corr}} = C_{D_{unc}} \cos\Delta\alpha + C_{L_{unc}} \sin\Delta\alpha \approx C_{D_{unc}} + C_{L_{unc}}\Delta\alpha \tag{2.19}$$
$$\Delta\alpha = \delta_0 \frac{S}{C} C_{L_{unc}} \tag{2.20}$$

The significant sweep of the planform warrants an additional correction for streamline curvature effects. This effect is most conveniently accounted for as an additional offset in angle of attack $\Delta\alpha_{sc}$ due to streamline curvature δ_1 and a change in pitching moment ΔC_M, while leaving the corrected lift and drag coefficients unaltered. Agard 109 provides the following relations that take into account some of the shape parameters of the planform to determine the magnitude of the pitching moment correction. In this relation below, $\bar{\bar{c}}$ is the mean aerodynamic chord, $\bar{c}$ the mean geometric chord, and $\Lambda_{0.5}$ the averaged half chord sweep angle.

$$\Delta C_D = \delta_0 \frac{S C_L^2}{C} \tag{2.21}$$
$$\Delta\alpha_{sc} = \frac{\bar{\bar{c}}\delta_1}{2\beta h} \frac{S C_L}{C} \tag{2.22}$$
$$\alpha_{corr} = \alpha_{unc} + \Delta\alpha + \Delta\alpha_{sc} \tag{2.23}$$
$$\Delta C_M = \frac{\bar{c}\delta_1}{16\beta h}\left[\left(\frac{\bar{\bar{c}}}{\bar{c}}\right)^2 + \frac{1}{3}(A\tan\Lambda_{0.5})^2\left(2 - \frac{\bar{\bar{c}}}{\bar{c}}\right)\right]\frac{S C_L}{C}\frac{\partial C_L}{\partial\alpha} \tag{2.24}$$

Evaluation of the above expressions shows that the correction to pitching moment is very limited. At an angle of attack of 10 degrees, the correction $\Delta C_{M_{\alpha 10}} = -7.9\mathrm{e}{-5}$ is of an order of magnitude smaller than the highest standard deviation observed in the measurements set (as shown in Appendix B). The correction to effective angle of attack is more significant though, with a value of $\Delta\alpha_{\alpha 10} = -0.142°$.

[14] Adapted from AGARDograph 109 [44]

[15] Adapted from AGARDograph 109 [44]

Blockage corrections

Secondly, solid blockage is the blockage of the mean flow due to the presence of the model. In an open jet solid blockage effects cause the body forces to be lower than those observed in free flight conditions, inversely to a solid boundary test section, where the increased dynamic pressure increases the model forces. This effect can be explained when imagining the image source doublets that represent the boundary effect in an open jet flow. These act in opposite direction to the wind tunnel flow.[43]

The non-dimensional interference velocity is defined as $\epsilon = \frac{u_i}{U_\infty}$, while the effect of solid blockage is most often denoted as ϵ_s. A blockage correction for elliptical open test sections is used to estimate the effect of solid blockage in the tested setup (Equation 2.25). In the relation below, T_R is a tunnel shape parameter and V_s the volume of the wing. T_R is estimated from Figure 2.16, using the width to height ratio of the reflected tunnel setup:

$$T_R = -0.325$$

$$\epsilon_s = (T_R + 0.029)\left(\frac{1}{C}\right)^{3/2}\frac{V_s}{\beta^3} \tag{2.25}$$

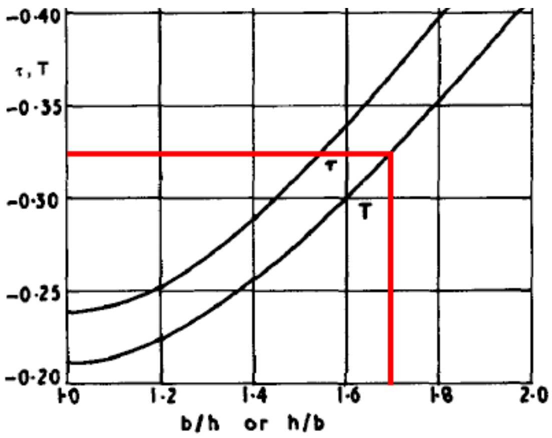

Figure 2.16: Estimation of tunnel shape parameter T_R for open rectangular tunnels [16]

The resulting value for solid blockage is $\epsilon_s = -0.0012$. The change of effective freestream parameters can be computed, using the linearised corrections for small ϵ. The following equations provide correction relations for velocity, dynamic pressure and Reynolds number. [45]

$$\epsilon_s = -0.0012$$

$$V_{corr} = V_{unc}(1 + \epsilon) \tag{2.26}$$

$$q_{corr} = q_{unc}[1 + (2 - M_{unc}{}^2)\epsilon] \tag{2.27}$$

$$Re_{corr} = Re_{unc}[1 + (1 - 0.7M_{unc}{}^2)\epsilon] \tag{2.28}$$

The solid blockage correction to velocity is thus only a reduction of -0.12% of the uncorrected freestream velocity. The corresponding correction to dynamic pressure at the test Mach number of M_{unc} 0.061 is -0.25%. In absolute terms this is a correction to dynamic pressure of -0.6Pa. Finally the Reynolds number is reduced by the same fraction as freestream velocity, since $M_{unc}{}^2 << 1$. The corrections to the aforementioned values are within the measurement accuracy range of the experiment. It is therefore concluded that solid blockage can be safely neglected in the results.

[16] Adapted from AGARDograph 336 [45]

Any wake blockage and buoyancy effects can also be assumed negligible for open test sections, since the wake can freely expand before the collector behind the test section.[45] The spanwise downwash distortion to local angle of attack along the span of the lifting surface is assumed negligible. In an open jet wind tunnel the angle of attack near the tip is reduced compared to free flight, making tip stall start at a higher geometric angle of attack. According to Barlow et al. the effect should be negligible for surfaces that span less than 0.8 of the tunnel, which is why these effects are further ignored for the tested setup. [43]

2.4.2. Vortex Lattice Method

With the advance of computing power, more advanced methods for wind tunnel corrections became available. Most notably, panel methods have been used for a long time, due to their low computing cost and applicability to solid wall wind tunnels. [44] Mokhtar and Britcher present results obtained for a full scale Wright Flyer replica in the Langley Full-Scale Tunnel, which has a $3/4$ open test section. Their method of correction involves modelling the aircraft using a panel method, as well as a simplified representation using horseshoe vortex singularities. Corrections are derived using an iterative process. First, the solid wall interference is estimated using a zero normal velocity wall boundary condition. Next, the shape of the test section is morphed, to find a shape closer to the open-jet wall boundary condition. These steps are iterated until the solution converges. [47][48] The blended wing-body study by NASA, discussed in Section 2.3, suggests the use of higher fidelity CFD calculations for more accurate correction. [9]

Such involved methods are considered outside the scope of this work. A simpler method to correct the performance of the wing to freestream conditions is described by Horsten and Veldhuis. [46] They describe that the lift and drag curve slopes obtained from vortex lattice code "Athena Vortex-Lattice" (AVL) can be used to estimate the gradient of the wall interference. Pseudo-viscosity is included in the solution through 2D estimations by XFoil. In this routine, the inviscid solution of AVL is used to estimate spanwise effective angle of attack distribution, which is used as an input for 2D airfoil code XFoil. XFoil then provides an estimation of viscous effects of five wing sections. At each wing section, the difference between local Reynolds number viscous and inviscid 2D airfoil calculations is used to calculate a local additional wing twist required to reduce the local inviscid lift coefficient to the viscous value. The resulting "warped" wing is used as an input in AVL to obtain a pseudo viscous solution for wing lift, and a spanwise effective angle of attack distribution for drag estimation. The drag is estimated as the sum of induced drag from the vortex lattice code and the linearly interpolated values for viscous drag from XFoil. As an example, the spanwise inviscid and "viscous" lift distributions obtained from this routine at $\alpha = 5°$ is shown in Figure 2.17.

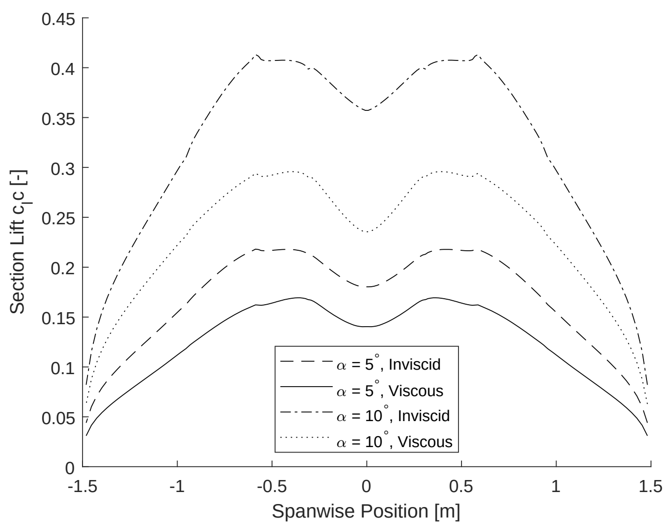

Figure 2.17: Spanwise loading of the Flying V, as predicted by both the inviscid and viscous AVL/XFoil routines

The resulting estimated lift and drag curves can be used to estimate the freestream aircraft performance. Let $C_{i_{und_1}}$ be the undisturbed (free stream) coefficient computed from the above routine, C_{i_1} be the measured value and $\Delta C_{i_{int_1}}$ be the interference at a given angle of attack α_1. The measurement is corrected for interference according to 2.29. The correction for the next measurement point at $\alpha = \alpha_2$ is computed from the result at this point, and the interference gradient, as shown below.

$$C_{i_{und_1}} = C_{i_1} - \Delta C_{i_{int_1}} \tag{2.29}$$
$$C_{i_2} = C_{i_{und_2}} + \Delta C_{i_{int_2}} \tag{2.30}$$
$$C_{i_2} = C_{i_1} + \frac{\partial C_{i_{und_1}}}{\partial \alpha}(\alpha_2 - \alpha_1) + \Delta C_{i_{int_1}} + \frac{\partial \Delta C_{i_{int_1}}}{\partial \alpha}(\alpha_2 - \alpha_1) \tag{2.31}$$

The gradient of the interference can be computed directly, with $C_{i_1} and C_{i_2}$ being measured values, and the gradient $\frac{\partial C_{i_{und_1}}}{\partial \alpha}$ known from the vortex lattice routine.

$$\frac{\partial \Delta C_{i_{int_1}}}{\partial \alpha} = \frac{(C_{i_2} - C_{i_1}) - \frac{\partial C_{i_{und_1}}}{\partial \alpha}(\alpha_2 - \alpha_1)}{(\alpha_2 - \alpha_1)} \tag{2.32}$$

Finally, this gives the interference and the corrected value at α_2:

$$\Delta C_{i_{int_2}} = \Delta C_{i_{int_1}} + \frac{\partial \Delta C_{i_{int_1}}}{\partial \alpha}(\alpha_2 - \alpha_1) \tag{2.33}$$
$$C_{i_{und_2}} = C_{i_2} - \Delta C_{i_{int_2}} \tag{2.34}$$

Zero incidence angle is recommended as a starting point, since the initial interference either has to be known, or is assumed to be small. Since most of the interference originates from lift, the interference at $\alpha = 0°$ is assumed to be small. It has to be taken in to account that small step sizes in alpha are required to reduce error in the estimation. Therefore, the results from measurements, XFoil, as well as those from AVL were represented as a spline to obtain values at steps of 0.01α. Moreover, the estimation is only valid as long as the combination of XFoil and AVL give a reasonably good estimation of the required gradients.[46] When 3D viscous effects start to dominate the flow over the wing this is surely not the case, as we will see in the next section.

2.4.3. Application of Corrections

The uncorrected and corrected results are summarized in Figure 2.18. Immediately, it can be observed that the lift curve slope is indeed improved. Both correction methods agree reasonably well on the initial C_{L_α} value, which is increased from $1.88 rad^{-1}$ to $2.12 rad^{-1}$, an increase of 12.7%. Lift to drag ratio is also significantly improved, with the vortex lattice correction predicting still less drag than the classical correction estimates. As an example, let us take the lift to drag ratio improvement at two lift coefficients. One representative for cruise, and another for optimum climb performance. A lift coefficient of 0.17 results in a level flight velocity of $35 m/s$. Maximum climb performance, is achieved at maximum C_L^3/C_D^2 and a corresponding lift coefficient of approximately 0.3. For these lift coefficients, not taking into account any control surface deflections required for trimmed flight, the L/D improvements predicted through correction are provided in the table below.

C_L	**Correction Method**	**L/D**
0.17	Uncorrected	8.8
0.17	Classical	9.5 (+8.2 %)
0.17	Vortex Lattice	10.3 (+17.0 %)
0.3	Uncorrected	9.7
0.3	Classical	11.4 (+17.5 %)
0.3	Vortex Lattice	12.6 (+29.9 %)

Table 2.1: L/D improvements estimated by corrected wind tunnel data

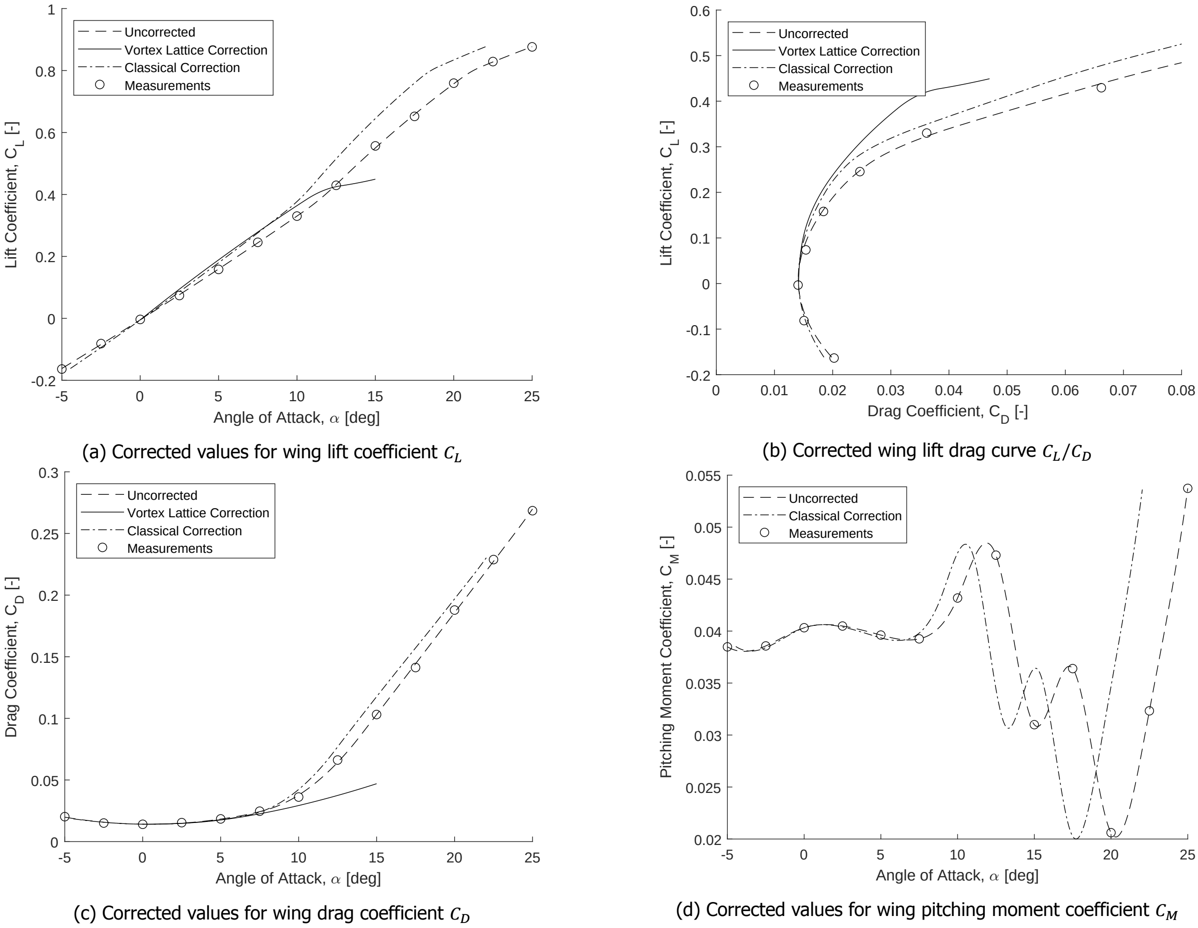

(a) Corrected values for wing lift coefficient C_L

(b) Corrected wing lift drag curve C_L/C_D

(c) Corrected values for wing drag coefficient C_D

(d) Corrected values for wing pitching moment coefficient C_M

Figure 2.18: Primary corrections for effective angle, lift, drag and pitching moment coefficients, using a vortex lattice routine and conventional correction methods

Figure 2.18d shows that the pitching moment behaviour is not affected significantly by any correction (ΔC_M) in pitching moment magnitude. However, the existing pitching moment behaviour is stretched due to the angle of attack correction. Qualitatively, it can therefore be concluded that the freestream angle of incidence at which the pitch break occurs is reduced, but the exact angle is relatively uncertain.

Quantitatively any corrections above $\alpha = 10°$ become increasingly doubtful. The assumptions required for classical correction do not hold when large scale separation starts to present itself on the wing. The vortex lattice routine earlier, while the drag approximation starts to depart from both the corrected and uncorrected drag curves around $\alpha = 7.5°$. From this incidence angle, 3D viscous effects and vortex lift start to dominate the performance of the wing, rendering a fully 2D lift and drag analysis worthless. Because the validity of the presented wind tunnel corrections can not be guaranteed over the full angle of attack range of interest, it is decided to not correct the obtained results for engine integration. Assuming that the discrepancy in effective angle of attack between wing-on and wing-off is small also greatly simplifies the analysis. Stretching behaviour similar to the pitching moment graph can be expected for any interference effects, resulting in lower absolute freestream angles of attack for the wind tunnel geometric angles presented in the rest of this work.

With test flights scheduled in the near future, more data becomes available for validation purposes. While comparing wind tunnel results to flight test data is a great method to gain further insight into validity of the correction methods, correlation to flight data will come with its own set of challenges. For example, the completeness of the flight model has to be taken into account and compared to the wind tunnel model. The SSFT model will have an undercarriage and possibly a different surface finish. Also the conditions in which data are obtained during flight testing have to be considered. For example, obtaining CLmax in a slightly sinking free flight condition can overestimate the actual value of CLmax.[43]

3
Setup and Method

The previous Chapter has highlighted the current status of relevant research done on the Flying V, expected trends of effects due to wind tunnel effects, available measurement techniques and common practice regarding engine integration testing. This Chapter combines this information and describes the hardware and method used to gather the data presented in this thesis. The components of the setup (Half model wing, nacelle, engine, engine mount and rake) are further detailed in their respective sections of this Chapter.

3.1. Experimental Setup

Combining the experience gathered by Palermo, Viet and Ruiz Garcia on the testing of the half model Flying V, adding common practice of engine integration testing and taking into account the available resources at Delft University of Technology results in the setup discussed in this Section. First the wind tunnel is discussed, followed by a detailed description of the half model and the used measurement equipment and methods. Finally an overview is provided of the test matrix and wind tunnel runs in Section 3.2.

3.1.1. Test Facilities

The experimental campaign is conducted in the TU Delft Open Jet Facility (OJF). The OJF is a closed loop, low speed wind tunnel with an octagonal test section of 2.85 by 2.85 meters and a maximum flow velocity of approximately 35 m/s. The airflow is driven by a large fan, powered by a 500kW electric motor. To reduce velocity deviations and turbulence of the flow, the flow is forced through several dense wire meshes, before blowing into the test section through a contracting nozzle. Finally, any added heat is removed from the flow after the test section by a 350kW radiator system, which keeps the flow at a constant temperature.[49] A schematic of the OJF wind tunnel is provided in Figure 3.1.

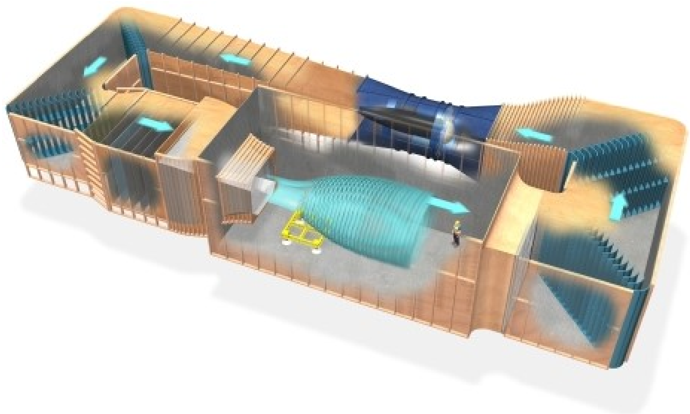

Figure 3.1: Schematic of the Delft University of Technology OJF wind tunnel facility [1]

3.1.2. Model Description

The wind tunnel half model of the Flying V is a glass fibre composite wing, with a semi span of approximately 1.5m. The planform dimensions are provided in Figure 3.2 The wind tunnel model represents exactly half of the Flying V SSFT model, which is a 4.6% geometrically scaled model of the full scale design.[10] Geometric scaling is required to fulfil similitude requirements for scaled flight testing. To investigate flight characteristics at low flight velocities (low Mach numbers), at least Reynolds number $\left(\frac{\rho V l}{\mu}\right)$ as well as Froude number $\left(\frac{V^2}{lg}\right)$ must be duplicated to achieve similitude of relative flow viscosity and gravitational and inertial effects. In these equations l represents some reference length, for example mean aerodynamic chord length. [50] Turbulator strips are positioned at 5% chord to ensure turbulent boundary layer flow over most of the wing surface. At the time of testing the SSFT is scheduled to be flown with turbulator tape at these chordwise positions. Therefore, the engine integration is tested in this configuration.

The use of half models has one main drawback; the presence of a developing boundary layer on the splitting plane. The presence of this boundary layer induces root flow conditions different from the full-span model, altering the spanwise lift distribution of the model. Since the lifting surface starts immediately in the case of the Flying V, this introduces a significant source of uncertainty to the experiment. Additionally, the current setup does not feature a peniche between the model and the splitting plane. Rather, a slight gap is present between the splitting plane and the root of the model. Research by Eder et al. [51] suggests that this could actually lead to results that are more consistent with a full-span model. Skinner and Zare-Behtash [52] also conclude that testing with an offset leads to more consistent results, regardless of the relative height of the stand-off gap. However, due to the difference in configurations tested, this is uncertain to be true for the Flying V half model.

Even though half models have their aforementioned drawbacks, Kooi et al. confirm they may be used specifically when the higher achieved Reynolds number benefits an integration study.[38] This may be the case when Reynolds number effects influence power plant installation effects or control surface effectiveness. With the Flying V expected to show significantly different vortical flow structures over the suction side of the airframe at varying Reynolds numbers, matching free flight and wind tunnel Reynolds numbers becomes a major priority. A smaller full span scaled model would require the tunnel to be ran at correspondingly higher velocity to achieve equal Reynolds number flow. [43] With a tunnel maximum velocity of 35m/s, the half model testing done at 20m/s and limited resources, continuing work on the half model is favoured over a smaller full span model.

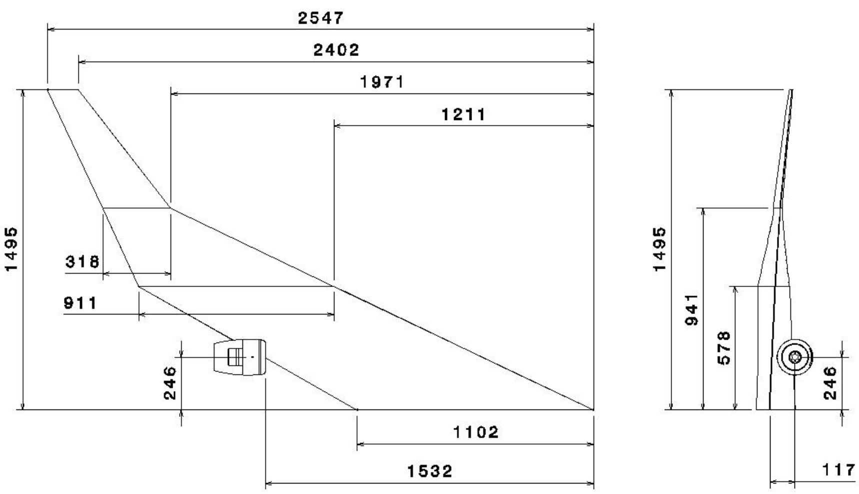

Figure 3.2: Dimensions of the Flying V half model, as previously used by Palermo, Viet and RuizGarcia. Now including engine position as proposed for the flight testing model. (Top view on the left, rear view on the right)

[1]Source: TU Delft [49]

3.1.3. Nacelle and Rake

The nacelle is an axissymmetric design, with a slightly diverging inlet. The throat area A_i is $0.010m^2$, which diverges to the actuator disk surface area of $0.0113m^2$ and then stays constant towards the outlet. A cross sectional view of the nacelle can be found in Figure 3.3. The nacelle is constructed from a double layered carbon fibre composite, to provide plenty of stiffness to the structure. To measure the nacelle in through-flow conditions, the engine is replaced by an aluminium cylinder of equal inner diameter.

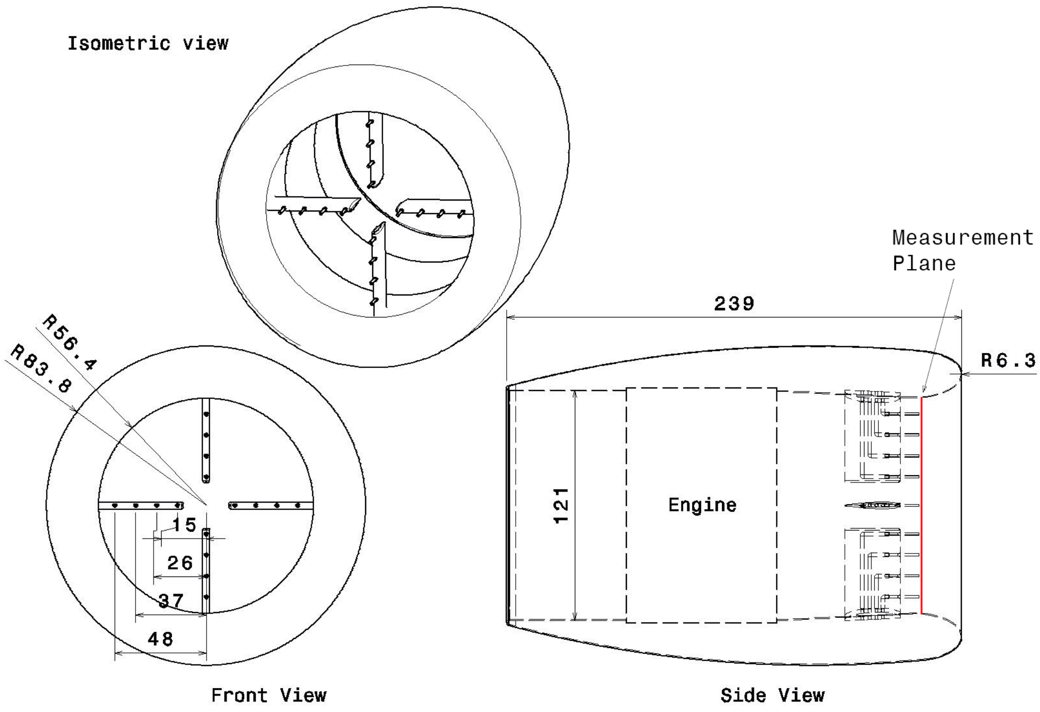

Figure 3.3: Drawing of the nacelle and installed rake. Note that the measurement plane of the rake is located at the throat of the engine intake.

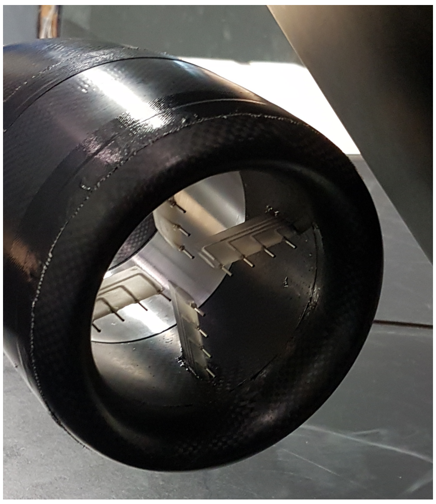

(a) Photo of the nacelle and installed rake as installed in the setup

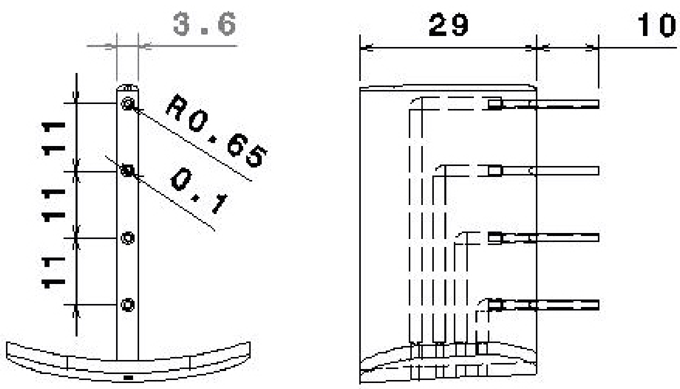

(b) Isolated drawing of one of the four rake vanes, including pitot probes and positioning dimensions

Figure 3.4: Detailed figures of the nacelle mounted total pressure rake

Total pressure is measured on the throat plane using a rake. Sixteen probes capture pressure data in a single measurement, while turning of the rake allows the full inlet surface pressure to be recorded through a series of measurements. Tubes in the nacelle are connected to a pressure transducer system, featuring sixteen 600Pa relative pressure sensors. The reference pressure used during the experiment is the static pressure of the test chamber, which is measured outside the wind tunnel jet. The signal of the transducers is captured with Labview and averaged over ten seconds.

The rake consists of two integral parts; steel capillary tubes as probes, and 3D printed, symmetrical wing profiles to host the probe tubes. Small channels in the profiles allow the measured pressure to be transferred to tubing within the nacelle and continue to the pressure transducer system. SLA 3D printing technology allows the printing of pressure channels, even in these small profiles, minimizing blockage of the nacelle. Capillary tubes with an outer diameter of 1.3mm and a wall thickness of 0.1mm are used as total pressure pitot tubes. These tubes offer maximum resistance to angular inflow due to low wall thickness to tube diameter ratio. According to Barlow et al. [43], inflow angles up to $20°$ from the probe axis should produce negligible effects on total pressure measurements for this thin walled tube type, as shown in Figure 3.5. A detailed drawing of one of the four rakes in shown in Figure 3.4b. A drawing of the nacelle and rake assembly is shown in Figure 3.3.

In hindsight, it should be noted that the pressure probes could have been positioned closer to the nacelle wall for more complete information. Circumferential resolution sufficed, while radial resolution could be improved. Quite a large outer section of the inlet face remains without information, while pressure measurements as close as 2x the tube outer diameter from the wall are generally possible without any wall interference effects. [43]

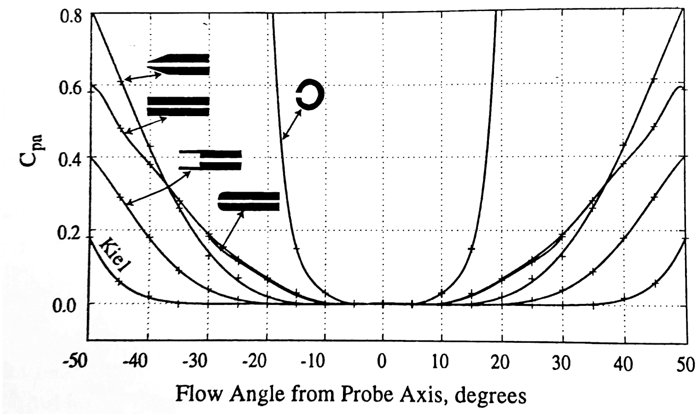

Figure 3.5: Pressure loss for different types of total pressure probes under sideslip [2]

3.1.4. Engine

The engine system selected for the SSFT Flying V are two electrically powered ducted fans designed for use on scale model aircraft (Schuebeler DS-86-AXI HDS®, Figure 3.6). One of these electric fans is used during the wind tunnel campaign. It features 10 blades, a fan diameter of 120mm and a fan swept area of $90cm^2$. The fan is immediately followed by three stator vanes to reduce swirl of the exhaust flow.

The motor of the fan is powered by 44.4V LiPo batteries in the flight testing model. During previous testing, the engine has shown to require relatively high currents for a single battery supply, causing the battery to overheat within a few minutes of running at full thrust. Thus, during wind tunnel testing the use of a power supply is deemed more time efficient. Even though this limits the maximum power at which the engine can be employed. Finally, overheating of the engine has to be prevented, which is most conveniently monitored by installing a thermocouple on the motor driving the fan. The information is summarized below.

[2]Source: Barlow et al. [43]

Fan diameter	120mm
Max. RPM	33,500
Design voltage	44.4-50.4V (12S LiPo)
Max current	180A
Max. Thrust	86N
Weight	1190g
Max. Motor Diameter	56mm

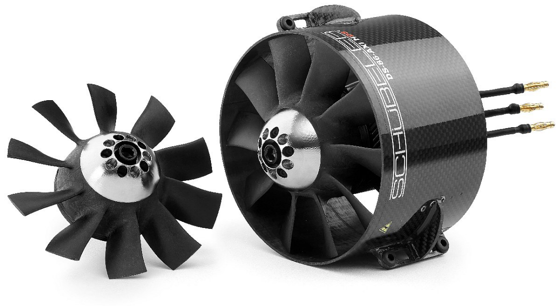

Figure 3.6: Picture of the electric fan used in the wind tunnel campaign [3]

Electronic Speed Controller

Fan speed is controlled by an electronic speed controller. The specific type is a TMM 25063-3, developed by MGM controllers. It controls the speed of the motor through the switching frequency of the three phase power signal. While the motor is sensorless, the rotational velocity of the motor is estimated through the back emf of the spinning motor. This value is logged by the ESC and stored on internal flash memory. The lack of an encoder does not allow any feedback control to be implemented in the setup and even though the logged rotational velocity was verified with a stroboscope, it provides a significant source of uncertainty. In the current experiment, the thrust setpoint of the ESC was set through a PWM signal from an Arduino Uno. DC power is supplied through a power supply of type TDK-Lambda GEN-60-85-3P400, capable of providing a maximum current of $85A$ at $60V$. Its control is set to provide a constant voltage of $50V$. The maximum thrust setpoint is limited by the power that can be supplied by the supply.

Engine Support Strut

For this campaign is is decided to mount the engine on a support strut and connect it to the main supporting elements under the reflection plane. The engine is not mounted directly to the wing to allow for multiple engine positions to be tested and keep the wing surface intact.

The engine support strut consists of a steel beam structure, with a 3D printed aerodynamic fairing. The fairing is based on the symmetric NACA 0012 profile, with a hollow leading edge to pass phase cables to power the engine, and a hollow trailing edge to house the pressure tubing for rake measurements. These are passed from the nacelle, through the fairing, to below the reflection plane, where the ESC and pressure transducers are situated. The engine mount in this setup connects to the ”top” surface of the nacelle, as far away and downstream from the wing as possible, to minimize upstream interference effects. Figure 3.9a shows a drawing of the engine and strut next to the wing.

3.1.5. Setup Overview

A complete overview of the wind tunnel setup is given in Figures 3.7 and 3.8. A six axis strain gauge balance is mounted on a turn table, which is bolted to the base support table. Forces are transferred from the wing and engine to the balance through a stiff aluminium beam structure. The splitting plane is positioned flush with the nozzle mouth to protect the balance reading from further airflow. The reflection plane is positioned in clean air to provide it with a fresh boundary layer. Notice the large aerodynamic shield required to protect the wing and engine mounting structure from the airflow between the reflection plane and the splitting plane, while allowing rotation of the setup. Reference values of the setup are provided in the table below. X locations are provided from the root leading edge of the wing. The Y location of the balance is assumed in line with the CG Y location of the wing. The airframe model with nacelles and nacelle supporting strut, mounted in the TU Delft OJF windtunnel, is shown in Figure 3.9a.

[3]Source: https://www.schuebeler-jets.de/

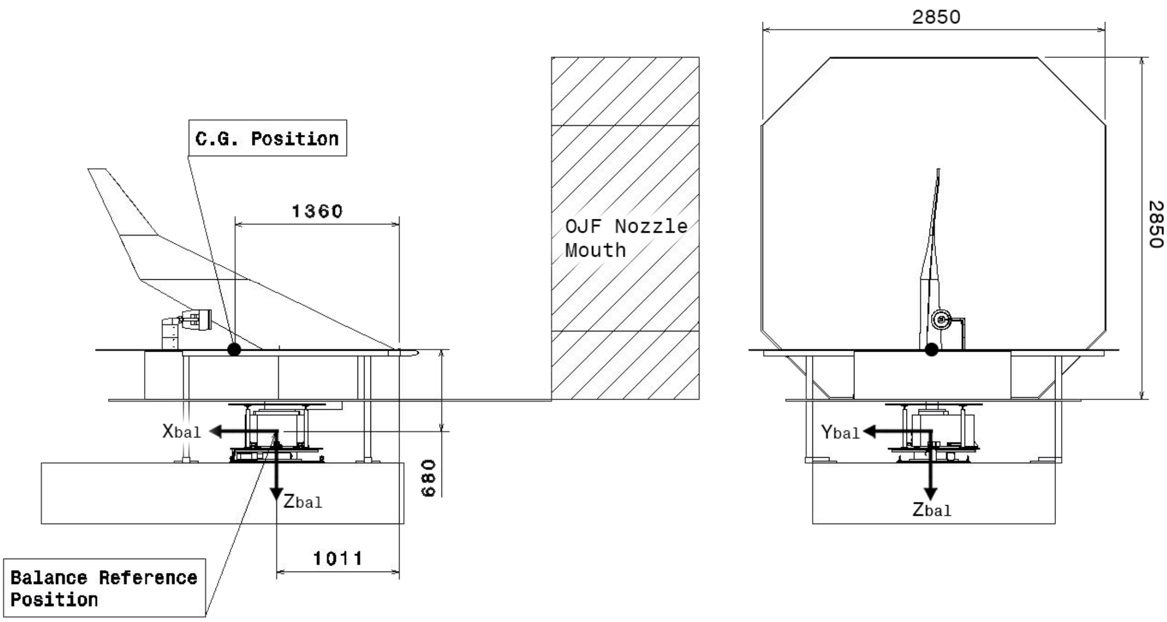

Figure 3.7: Side view and rear view of the complete wind tunnel setup

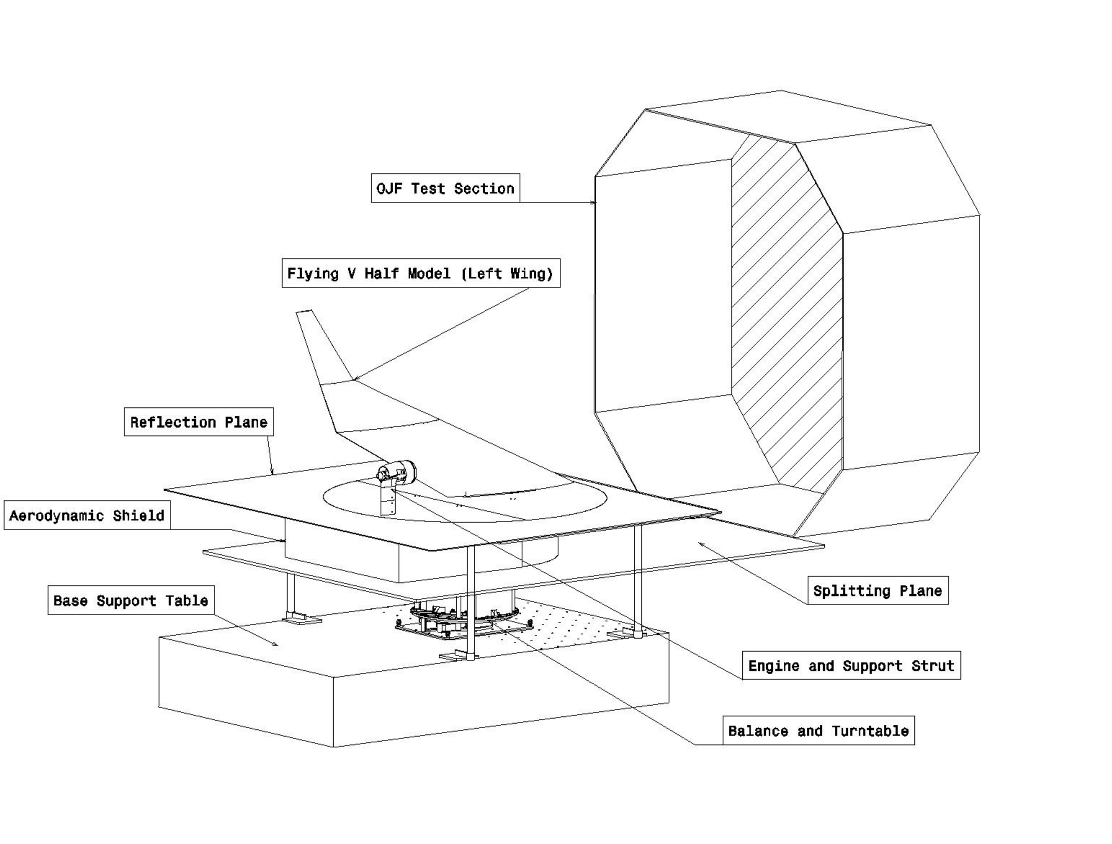

Figure 3.8: Overview of the complete wind tunnel setup

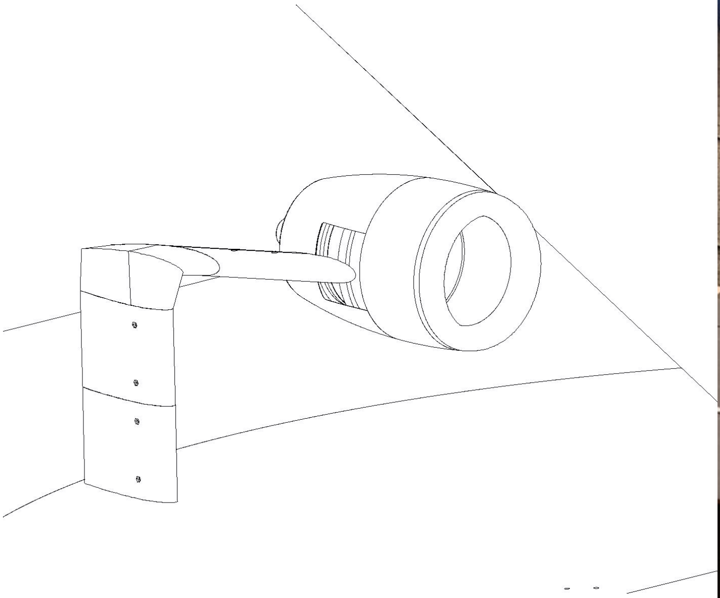

(a) Close-up of the Engine and strut installed next to the wing

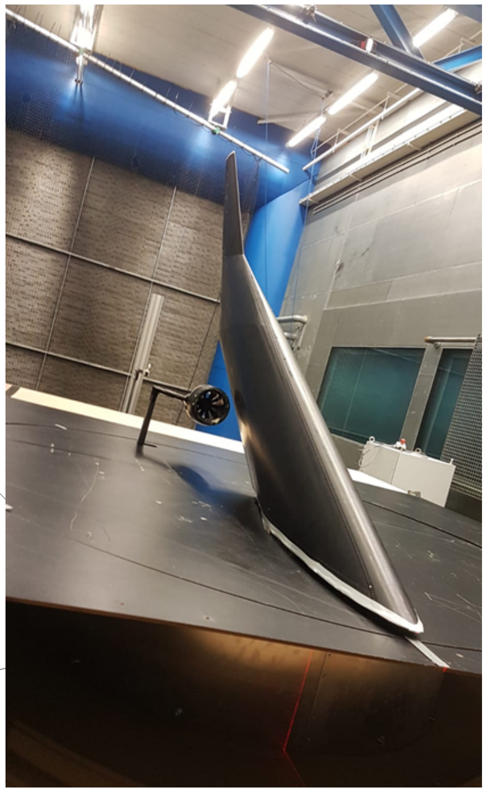

(b) Photo of the setup in the OJF

Figure 3.9: Closeup schematic of the engine and strut, photo of the wind tunnel setup

Variable	Symbol	Value
Wing surface Area	S	0.935 $[m^2]$
Mean Aerodynamic Chord	$\bar{\bar{c}}$	0.820 $[m]$
Center of gravity X location	x_{cg}	1.360 $[m]$
Balance X location	x_{bal}	1.011 $[m]$

Table 3.1: Reference values of the half model setup

3.2. Method

The test matrix is heavily based on the previously recorded behaviour of the Flying V half model. Research done by Palermo, Viet and Ruiz Garcia provided the clean wing trimmable angle of attack range and optimum CG at 20m/s freestream velocity. The trimmable flight angle of attack range of the wing at this velocity is limited due to a pitch break at 20° AoA, as further highlighted in Section 2.2.1. The optimum CG position defined from the spline model representation by Ruiz Garcia ($1.360m$ from the nose of the aircraft) is used for all moment coefficient plots in this work. These observations limit the region of interest for integration measurements to an angle of attack range between -5° and 30°.[10][11][12]

From work by Ruiz Garcia [12] it can be concluded that measurements are relatively constant within the tested velocity domain. It is therefore decided to limit the size of the test matrix by testing at two free stream velocities. The choice is made to use a tunnel speed of $20m/s$ as the main measurements of the campaign, since this is close to the intended takeoff and landing velocity of the SSFT model ($Re \approx 1e^6$). Thus, measurements could be used to judge takeoff performance of the SSFT model. Measurements at a tunnel velocity of $15m/s$ are used for additional information close to minimum flight speed and to investigate some dependency on free stream velocity. Unfortunately testing the complete angle of attack range at higher Reynolds numbers is not possible. Balance load limits are reached within this flight envelope at higher wind tunnel velocities.

3.2.1. Balance measurements

The balance measurement campaign consists of the following steps:

1. The first step the campaign is to calibrate the engine. To be able to separate effects as much as possible, the calibration is split into three steps.
   - First the support on which the isolated engine is mounted is tested to quantify its contribution to lift, drag and pitching moment.
   - The engine is easily disassembled from the nacelle to obtain a TFN. This TFN is tested for the trimmable flight range ($-5°$ to $30°$ with $2.5°$ step) to measure its lift and drag contributions.
   - These tests are repeated with the fan installed and at a range of thrust setpoints to investigate thrust effects on the isolated engine. Thrust is controlled through the PWM duty cycle of the signal going to the ESC. A range of from idle to maximum thrust is used: 20% Duty cycle to 70% Duty cycle, with a step size of 5%. The resolution of the angle of attack range however, is reduced to $5°$ limiting the overall amount of testing time.
2. With engine calibration done, clean configuration half model tests will be done to repeat some of the work done by Palermo, Viet and Ruiz Garcia for verification and validation purposes. The modified setup is expected to provide similar balance results, and the root flow should not be altered to allow meaningful engine integration on the inboard section. No control surface deflections will be taken into account. These surfaces are assumed to be far enough outboard to not influence the inboard flow field, allowing the effects to be superimposed later. Runs at a range of $-5°$ to $30°$ angle of attack, with a step size of $2.5°$ are done. This should provide a good baseline polar for the clean configuration, while providing some additional information around the pitch break.
3. TFN integrated half model tests will follow to quantify the installation and interference effects of the nacelle. The same range of incidence angles is used for this test as that of the isolated wing.
4. Tests with the wing and engine in power-on conditions are finally used to quantify the thrust effects of the integration. Again, the step size between incidence angles is increased to $5°$ to reduce the size of the test matrix.

3.2.2. Bookkeeping

The bookkeeping definitions given in this section are followed throughout the rest of this work. Results of different measurement runs are combined to investigate the interaction between components. This section describes the bookkeeping done to arrive at the installation and interference effects of the propulsion system. Before stating any definitions, it is important to be aware of the notation used. The letters used in the equations below each represent a component, the definitions of the letters are summarized in Table 3.2. Letter combinations denote a measurement condition. For example, WENS is a measurement result including the wing, engine in power on conditions and the engine strut, while WNS defines the results obtained from the wing, nacelle and strut in TFN conditions. Following this definition, WEN is the notation of the aircraft in power-on conditions.

Table 3.2: Bookkeeping Nomenclature

W	Wing
N	Nacelle
S	Engine Strut
E	Jet (Power-on)
P	Total Engine (N+E)

Bookkeeping Engine Strut

As a first bookkeeping step, the engine strut that is included in the setup has to be subtracted from any measurement to obtain the forces acting on the aircraft only. The forces and moments acting on the strut are subtracted from measurements taken on the isolated nacelle and engine. This is done for both idle and powered conditions to arrive at the forces and moments acting on the isolated nacelle and engine respectively (Equations 3.1 and 3.2).

$$N = NS - S \tag{3.1}$$

$$EN = ENS - S \tag{3.2}$$

Next, something similar can be done for the strut in wing-on conditions. In the following definitions, it is assumed that the downstream effects of the wing on the strut are much larger than the upstream effect of the strut on the wing. This allows the forces of the engine strut, **under influence of the wake of the wing** S_w, to be taken as:

$$S_w = WS - W \tag{3.3}$$

Then, these newly defined forces acting on the engine strut are subtracted from the wing-on measurements of TFN and engine in the following way (Equations 3.4 and 3.5) resulting in the forces and moments acting on the Wing/TFN and Wing/Engine combinations.

$$WN = WNS - S_w = WNS - (WS - W) \tag{3.4}$$

$$WEN = WENS - S_w = WENS - (WS - W) \tag{3.5}$$

Installation and Integration Definitions

Combining the previously determined definitions, it is possible to obtain the installation and interference effects of the wing, nacelle and jet. The installation effect at TFN conditions is defined as the addition drag due to the installation of the engine at flow-through nacelle (idle) conditions. [42] The installation effect of a nacelle or propulsion system is defined as the measurements of wing and engine, minus the measurements of the isolated wing. It can be subdivided into the installation effect of the nacelle (3.6) and the addition of thrust (3.7). Together they form the total installation effect of the engine (3.8).[42]

Nacelle Installation

$$I_N = WN - W \tag{3.6}$$

Jet Installation

$$I_E = WEN - WN \tag{3.7}$$

Engine Installation

$$I_P = WEN - W = I_N + I_E \tag{3.8}$$

The interference effects of a nacelle or propulsion system are defined as the difference between the installed system and the measurements of the isolated components. It can be subdivided into the interference effect of the nacelle (3.9) and the interference effect of the jet (3.10). Addition results in the interference effect of the engine (3.11). [42]

Nacelle Interference

$$If_N = WN - (W + N) \tag{3.9}$$

Jet Interference Effect

$$If_E = (WEN - WN) - (EN - N) \tag{3.10}$$

Engine Interference

$$If_P = WEN - (W + EN) \tag{3.11}$$

Inlet measurements

A total pressure rake is used to map inlet distortion on the nacelle inlet. This should give a good idea whether the idle engine is blanketed by the wing at high angles of attack, or actually receives relatively clean air.

Measurements are conducted at three incidence angles; $5°$,$15°$ and $25°$. At these angles the inlet pressure is recorded for full thrust, idle and TFN nacelle conditions at a free-stream velocity of $20 m/s$. These measurements should provide some insight into differences between TFN and full thrust conditions and complement the understanding of the balance measurements. Also, at an incidence angle of $5°$ and $30 m/s$, power-on and idle conditions are tested to represent cruise. SAE-ARP-1420 suggests that angular intervals of $45°$ is the minimum requirement, proposing the standard rake of eight times five probes. [31] Therefore, it is decided to test at 22.5 degree spaced angles with the rake, to obtain adequate coverage of measurement points over the full surface, even with the four times four probe rake describes in Section 3.1.3. At the same time, blockage within the nacelle is reduced by introducing fewer probes at each measurement interval. The measurement stations are visualized in Figure 3.10.

Repeatability of all the experiments is checked by performing measurements five times at each point in the test matrix. The wind tunnel flow velocity is recorded by a pitot tube before the throat of the tunnel for total pressure and a separate static pressure measurement. This serves as the reference pressure for the recorded values in the nacelle.

Typically the rake has good accuracy for flow velocities at the intended normal flow direction and rapid response to fluctuations in flow velocity. The dynamic pressure recordings were averaged over ten seconds to obtain a mean total pressure recording. At high deflection angles the accuracy of the obtained data may reduce. Also, the presence of the rake itself has some effect on the flow in the test section. Therefore, no combined balance and rake measurements were used. [43]

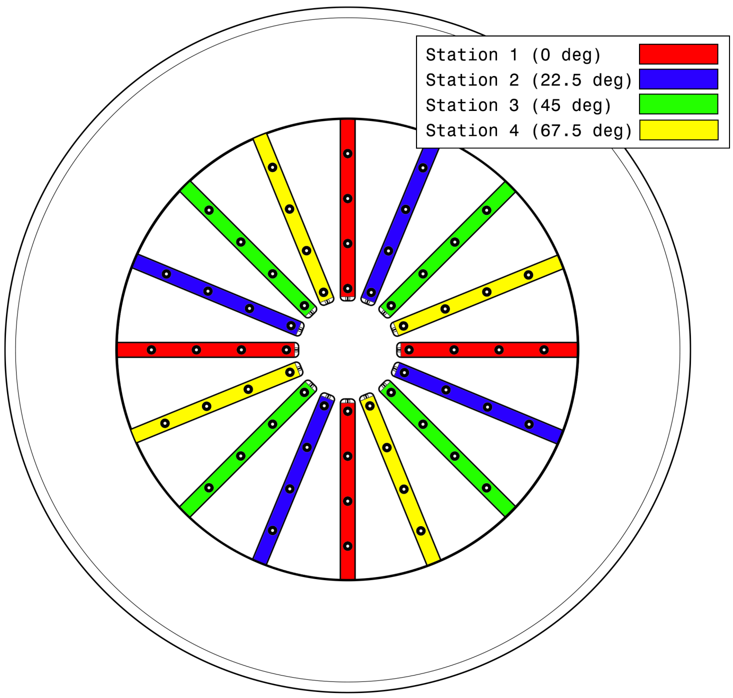

Figure 3.10: Measurement stations of the pressure recordings visualized from the front view of the nacelle

3.3. Frame of Reference

Three reference frames are used in this work; the balance, body and aerodynamic frames of reference. Balance measurements ($\vec{F}_{bal}$,$\vec{M}_{bal}$) are recorded in the balance frame of reference. The transformation matrix from the balance frame to the body-fixed reference frame is:

$$T_{B,bal} = \begin{bmatrix} -1 & 0 & 0 \\ 0 & 0 & 1 \\ 0 & 1 & 0 \end{bmatrix} \tag{3.12}$$

Transformation between the balance and body frames of reference results in body forces and moments ($\vec{F}_B$ and $\vec{M}_B$), with $s_{B,bal}$ the vector between the balance origin and wing center of gravity reference point. Only the offset in X direction is used, and can be found in Table 3.1.

$$\vec{F}_B = T_{B,bal}\vec{F}_{bal} \tag{3.13}$$

$$\vec{M}_B = T_{B,bal}\vec{M}_{bal} + s_{B,bal}\vec{F}_{bal} \tag{3.14}$$

The non-dimensional characteristic numbers lift, drag, pitching moment coefficient are presented in aerodynamic (Kinematic) reference frame. Transformation between frames of reference is visualized in Figure 3.11. Since only angle of incidence α is varied during this campaign, the equations from body frame of reference to non-dimensionalized coefficients in aerodynamic frame of reference can be simplified to:

$$C_L = (-F_z\cos(\alpha) + F_x\sin(\alpha))/qS \tag{3.15}$$

$$C_D = (-F_x\cos(\alpha) - F_z\sin(\alpha))/qS \tag{3.16}$$

$$C_M = M_y/qS\bar{c} \tag{3.17}$$

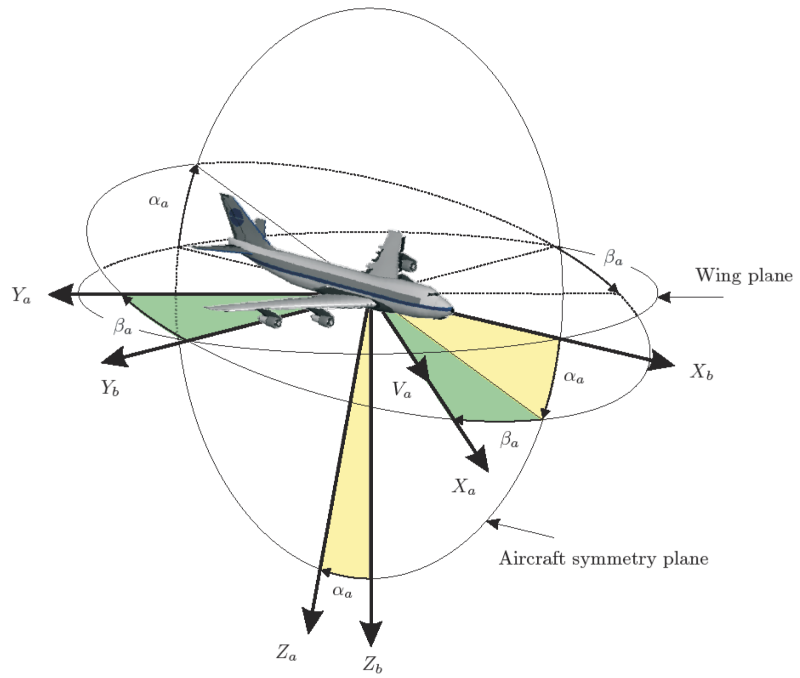

Figure 3.11: Aerodynamic Reference Frame in relation to Body-fixed Reference Frame[4]

[4]Source: TU Delft

4
Verification and Validation

Before taking a closer look at the obtained results, this Chapter provides an overview of the limitations of the obtained results. First of all, note that the average of the raw measurements and their standard deviations can be found in Appendix B. Section 4.1 provides an overview of the sources of uncertainty and their impact on the data. Next, Section 4.2 and 4.3 discuss how the obtained results were verified and models were validated.

4.1. Uncertainty Analysis

Experimental investigations always involve a level of uncertainty. The following sources of uncertainty are identified for the conducted experiments:

- The setup is assumed infinitely stiff. However, during measurements the wing flexes and vibrates, more so at higher incidence angles. Also with the engine mounted on a strut instead of directly to the wing, positioning of the engine relative to the wing changes due to wing flexing.
- The wind tunnel inflow is not perfectly uniform. The OJF wind tunnel is shown to have a flow uniformity (velocity deviations from mean velocity) of 0.5% and a turbulence level of 0.24%.[53]
- Measurement equipment precision and accuracy is limited. Balance measurements are recorded to a precision of $0.01N$. Calibration of the balance has shown that the standard deviation of force and balance measurements is also in the order of $\mathcal{O}(10^{-2})N$.
- Additionally the balance shows a slight drift in measurement value over time. Corrections are done using linear interpolation between bias measurements at the start and end of a set of measurements.
- On a long term basis, the precision of setup is quite limited. The setup is aligned with the wind tunnel using laser sheet, utilizing the leading edge split line as a reference. Due to the procedure followed, the offset could be a combination of dihedral and angle offset. This manual procedure could produce an error in incidence angle of the order of $\mathcal{O}(10^{-1})^{\circ}$.
- Engine speed changes slightly due to change in internal resistance of the electronic speed controller and power cables with temperature. This could be improved by installing an encoder and implementing control feedback to achieve an exact speed setpoint. It is therefore decided that in its current state, the engine setup is not suitable to investigate small differences in power consumption due to wing wake ingestion. Instead, the power required is assumed constant with RPM. The power figures given in Appendix C should be treated as rough estimates.
- Phase cables to the engine had to be most carefully installed to not transfer part of the forces that should be measured by the balance.
- ESC data could not be captured for the full test matrix, due to limited memory capacity and the absence of an option to further reduce the sample rate of the controller in software.

- Finally there is the imperfect representation of the full span model by the half model representation. Whilst argued to be a valid choice for the presented research (Section 2.1), the altered root flow conditions introduce an unknown error to the recorded behaviour.

4.2. Verification

The increased blockage under the reflection plane was investigated using smoke flow. It was found that the increased under table blockage did not induce a large upwash in front of the splitting plane leading edge and that the flow over the table leading edge was nicely attached. Combined with the consistency relative to previously obtained results it was concluded that the increased shield size did not have a large impact on obtained results.

Propeller rotational speed was verified using a stroboscope and white paint on the propeller blades. The propeller was run at the different speed setpoints used in the test matrix and the stroboscope was adjusted to match the frequency of rotation. Comparison with the data recorded by the ESC revealed that any measurement errors between the stroboscope and speed controller were negligible. The values recorded by the ESC are therefore taken as the exact rotational velocity of the fan in the rest of this work.

The nacelle inlet total pressure measurements were verified using free steam total pressure recorded by the wind tunnel. The undisturbed inflow of a through flow nacelle at $\alpha = 0$ should have a stagnation pressure equal to the free stream. While the pressures in the inlet are recorded as pressure differential to the test chamber static pressure, the measured differential should be equal to the dynamic pressure of the wind tunnel jet. Figure 4.1 pressure displays the observed difference in total pressure between the TFN at zero incidence and the recorded free stream total pressure, averaged over the four runs to sweep the inlet plane.

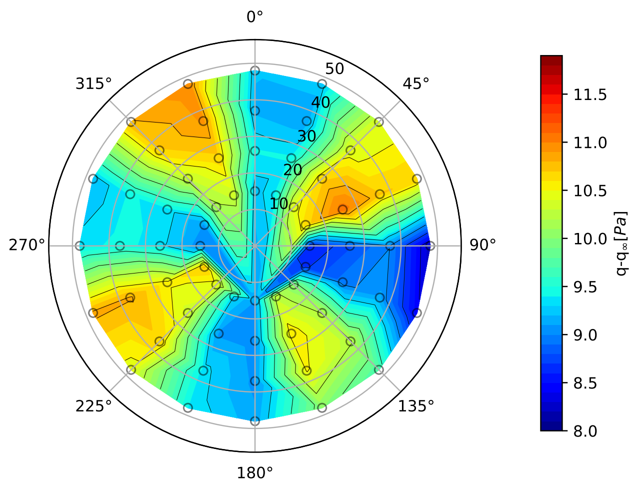

Figure 4.1: Difference between dynamic pressure measured on the inlet plane and the dynamic pressure measured by equipment in the wind tunnel

It can be observed that the pressure is recorded with a maximum difference of approximately $3Pa$ over the inlet plane. This difference can mostly be accounted to the difference between wind tunnel conditions in subsequent runs, when the rake is turned to its next angular position. The average difference in total pressure on the inlet plane and in the free stream is approximately $10Pa$. It can therefore be concluded that the total pressure is recorded with high precision, though with an offset of approximately $10Pa$ to the wind tunnel recording at a free stream velocity of $20m/s$. The results are corrected for this discrepancy. The maximum recorded pressure loss is $420Pa$. Thus, the difference of $3Pa$ due to altering conditions between runs is regarded as negligible compared to the distortion effects that are measured.

4.3. Validation

Analysis by both Palermo [10] and Ruiz Garcia [12] has shown that short term repeatability of the setup is quite good and confidence intervals are generally small. However, no investigation to this point has been done to check its long term repeatability. The plots of Figures 4.2a, 4.2b and 4.2c are obtained from clean wing wind tunnel runs, with the control surfaces undeflected. The raw data of these experiments was treated in the same way to arrive at the displayed results. The three sigma (short term) confidence intervals of the measurements obtained by the author are shown in the plots for comparison, with the sample standard deviation taken as:

$$s = \sqrt{\frac{\sum_1^n (x_i - \bar{x})^2}{n-1}} \tag{4.1}$$

In which, x_i is a measurement value, $\bar{x}$ is the sample mean and n is the number of samples. It has to be noted that five samples were taken at each measurement point in this campaign, compared to the three samples taken by both Ruiz Garcia and Palermo in their respective campaigns. The additional measurements were deemed necessary to obtain more confidence in the relatively small interference effects.

Moreover, with the bookkeeping required to arrive at installed engine conditions, the addition and subtraction of uncertainties has to be taken into account. When assuming that two measurement conditions (a and b) are completely independent, the standard deviation of the added (or subtracted) results can be computed as the square root of the two sample variances (Eq. 4.2). Therefore, as a result of the bookkeeping, the uncertainty of the obtained result grows.

$$s = \sqrt{s_a^2 + s_b^2} \tag{4.2}$$

From the plots of Figure 4.2 a couple of conclusions can be drawn. First of all, short term repeatability seems very good. Taking out any outliers results in the short term standard deviations of the order $\mathcal{O}(10^{-3})$ for lift, drag and pitching moment coefficient. From the lift curve of Figure 4.2a it can be suggested that there is a slight angular offset between runs. The closeness between the lift/drag curve of Figure 4.2b confirms that this may be the case. However, the slope of the pitching moment behaviour also seems to be slightly higher at lower angles, with the additional resolution showing two local increases in pitching moment at $\alpha = 12.5°$ and $\alpha = 17.5°$. While the trend of all measurement campaigns is clearly the same, and the absolute values in terms of lift and drag are very close, in most cases the repeatability on the short term is much better than the long term one. In other words, the precision of the experiment is great, while the accuracy between campaigns is much more limited.

Long term repeatability is limited due to slight changes to hardware and unavoidable error introduced when setting up the experiment. When setting up the experiment, the wing is lined up with the wind tunnel flow direction using a laser sheet. The laser sheet is positioned manually on the wind tunnel centerline, on which the leading edge split line of the wind tunnel model is placed. However, when there is an offset in dihedral of the wing, this consequently results in a mismatch of angle of attack when lining it up with the laser sheet. The construction of the setup thus introduces unavoidable errors in this respect and care has to be taken to compare only runs with as few changes to the setup as possible. The wing was mounted and dismounted only when required due to the test matrix. Finally, also the setup of engine position has some effect on the obtained results. Therefore, while the long term repeatability of engine positioning was not tested, it has to be assumed that its uncertainty is in the same order of magnitude as that of the wing.

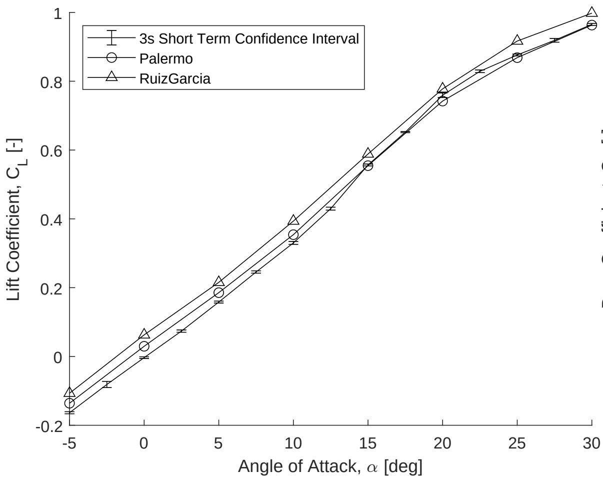

(a) C_L - Repeatability of the Flying V half model setup

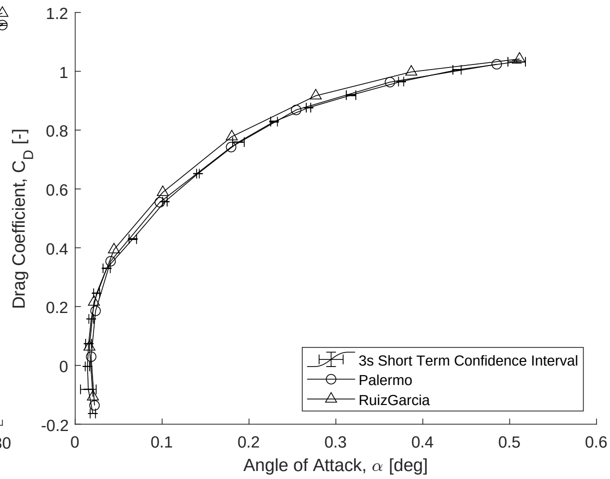

(b) C_L/C_D - Repeatability of the Flying V half model setup

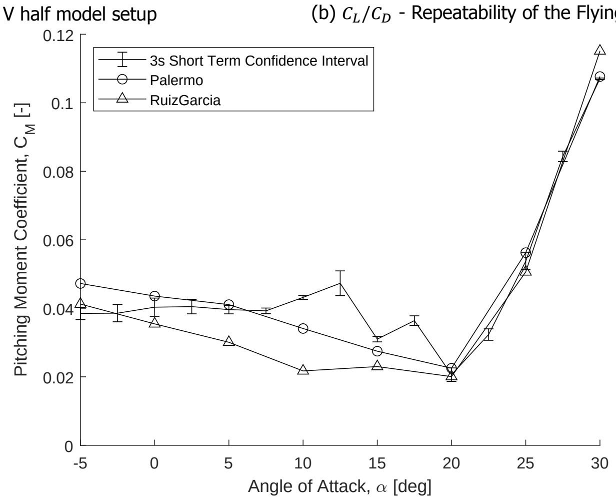

(c) C_M - Repeatability of the Flying V half model setup

Figure 4.2: Comparison of previously obtained (Palermo [10] and Ruiz Garcia [12]) clean-wing results to the results of the present campaign

Significance of interference effects

The interference effects between airframe, engine and engine jet are quite small. Therefore, an important question to answer is: are the observed differences statistically significant? This section aims to explain the method used to determine. It shows whether there is value in the obtained results and where the measurement precision was not high enough to trust the recorded differences.

To investigate whether the measured installation and interference effects are significantly different to uninstalled effects, a two tail t-test for two random samples with unknown variance is performed. In essence, this test gives an approximation for the probability that two sample means are significantly different, by estimating the normal distribution of the difference between the sample means. Since the total population variance and means (σ and μ) are unknown (only the sample variance and mean are known), the sample variance and sample size (S and n) are used to estimate the t-statistic. Next, the Student's t-distribution with the corresponding degrees of freedom is used to determine the statistical significance of the difference between the means. To establish a region of validity, a two tail test, with significance level 0.1 (95% certainty of a real difference between the means) is chosen.

For this analysis, it is assumed that all conditions for inference are met. In other words, the samples are assumed to be random and independent and taken from a normally distributed population.[54] This is extremely important, because the assumed Student's t-distribution would otherwise be invalidated. For measurement samples, these assumptions generally hold. Note that, in this case, an increasing number of samples taken brings the Student's t-distribution closer and closer to the normal distribution the random sample was taken from, with the first five degrees of freedom making the greatest relative steps.

To determine how significant the difference between results is, one can test the following hypothesis. For the null hypothesis H_0 it is assumed that the population mean of the first measurement condition is equal to the second measurement condition. The corresponding alternative hypothesis H_a states that the means of the two populations are not equal. The probability distribution between these two hypotheses is a measure for the significance of the difference between measurement conditions.

$$H_0 : \mu_a = \mu_b, \qquad H_a : \mu_a \neq \mu_b \tag{4.3}$$

Assuming the null hypothesis results in the following definition for the t-test with unknown population means and variances. [54]

$$t = \frac{\bar{x_a} - \bar{x_b}}{\sqrt{\frac{s_a^2}{n_a} + \frac{s_b^2}{n_b}}} \tag{4.4}$$

Using the definition of a Student's t-distribution cumulative distribution function, the probability of the null hypothesis being true is tested. Equation 4.6 shows the Student's t-distribution function for $v = n-1 = 4$ degrees of freedom, with $F(t)$ the cumulative distribution function and $f(u)$ the probability density function.[54]

$$F(t) = \int_{-\infty}^{t} f(u)du \tag{4.5}$$

$$F(t) = \frac{1}{2} + \frac{3}{8}\frac{t}{\sqrt{1+\frac{t^2}{4}}}\left[1 - \frac{1}{12}\frac{t^2}{1+\frac{t^2}{4}}\right] \tag{4.6}$$

Finally, the probability of the null hypothesis being true is then given as:

$$P(u \leq |t|) = 2(1 - F(|t|)) \tag{4.7}$$

$$P(u \leq |t|) = 1 - \frac{3}{4}\frac{|t|}{\sqrt{1+\frac{|t|^2}{4}}}\left[1 - \frac{1}{12}\frac{|t|^2}{1+\frac{|t|^2}{4}}\right] \tag{4.8}$$

To reject H_0 with 95% certainty ($\alpha = 0.10$), and therefore claim that the measurements are significantly different, a two tail t-test has an absolute critical t value $|t_{crit}|$ of 2.776. For any t-value higher than 2.776 the measurements are seen as significantly different, either in positive or negative direction compared to the reference condition. The plots on (Figures 4.3a up to and including 4.4c) show the t-statistic for interference effect measurements for powered testing at 20 m/s. The dashed red lines indicate the contour of $|t_{crit}| = 2.776$. This indicates that the areas with higher t-statistic values, enclosed by the domain boundaries and the red dashed lines, contain a significant difference with 95% certainty. From these figures the conclusion can be made that there are definitely interference effects that are large enough to be deemed significant, even for the limited accuracy and precision of the setup.

Engine Interference

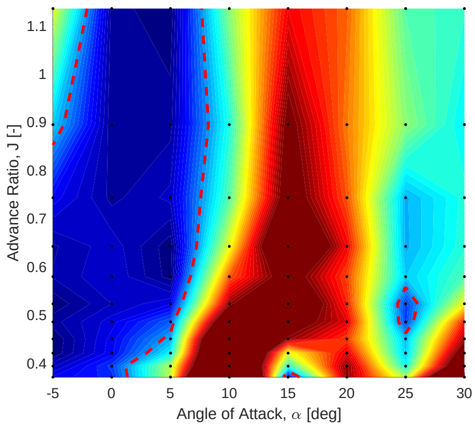

(a) T-statistic for Engine Interference ΔC_L measurements

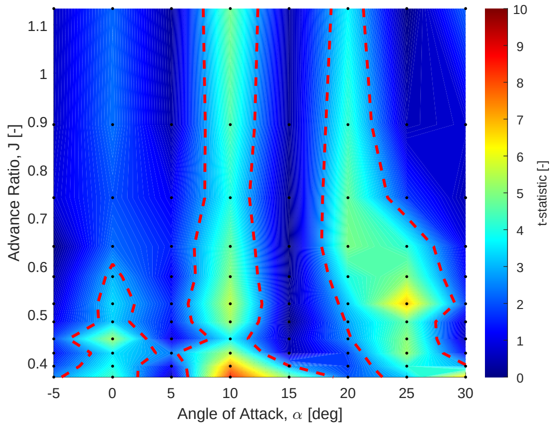

(b) T-statistic for Engine Interference ΔC_D measurements

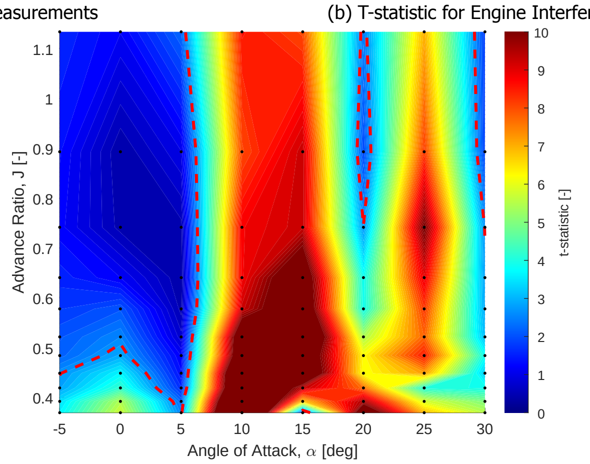

(c) T-statistic for Engine Interference ΔC_M measurements

Figure 4.3: Surface plots showing the t-statistic for engine interference ΔC_L (a), ΔC_D (b) and ΔC_M (c), for combinations of J and α

Jet Interference

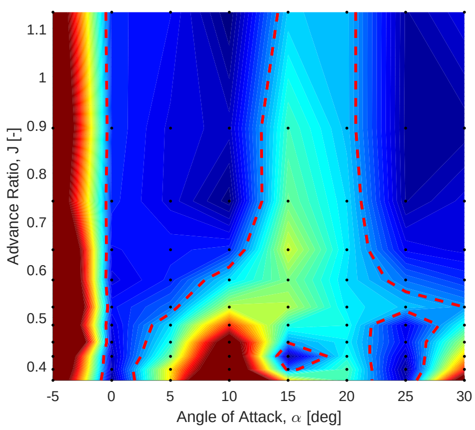

(a) Surface plot showing the t-statistic for ΔC_L measurements, for combinations of J and α (jet effect, power-on conditions)

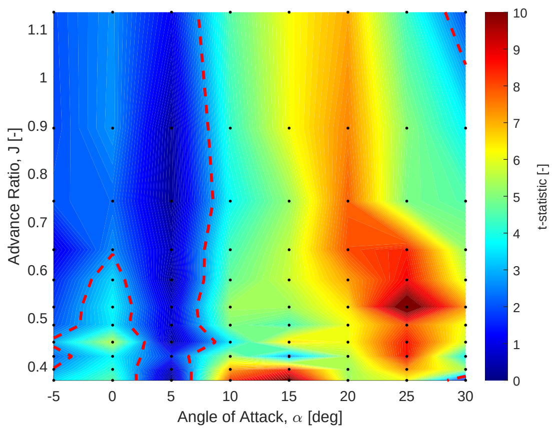

(b) Surface plot showing the t-statistic for ΔC_D measurements, for combinations of J and α (jet effect, power-on conditions)

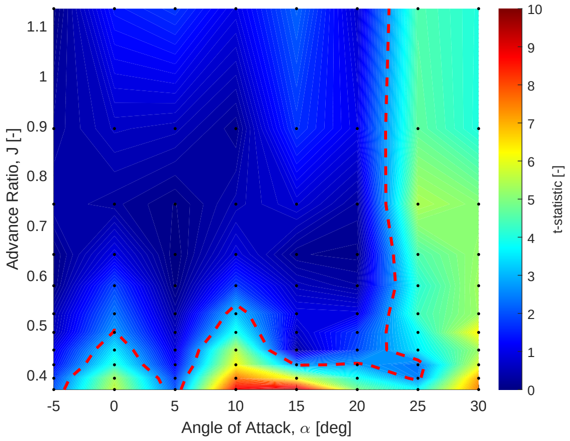

(c) Surface plot showing the t-statistic for ΔC_M measurements, for combinations of J and α (jet effect, power-on conditions)

Figure 4.4: Surface plots showing the t-statistic for jet interference ΔC_L (a), ΔC_D (b) and ΔC_M (c), for combinations of J and α

4.4. Validation of Engine Model and Performance

The figures below show that the basic engine model that was fitted to the data at a velocity of 20 m/s is not very sensitive to changes in velocity. At least for this small velocity change, extension of the curves to include advance ratios of the measurements at 15m/s show a very good fit. This indicates that the model based only on advance ratio works well enough for the intended purpose and that no Mach or Reynolds number dependent terms (Section 2.2.2) are required.

It can be concluded that the fan has a stable enough rotational velocity to be used for integration measurements. And the relations can be used to estimate both the thrust force, as well as the thrust coefficient of the engine at a given advance ratio. The thrust force coefficient is indirectly used to subtract engine contribution in the bookkeeping scheme. The thrust coefficient is used to approximate inlet velocity for distortion measurements.

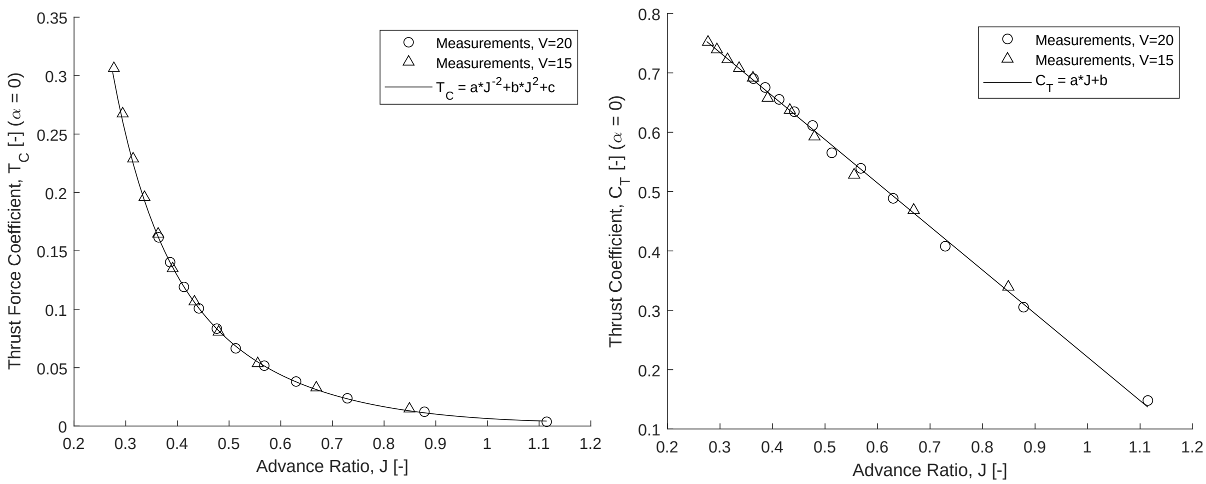

(a) Thrust coefficient T_C as a function of advance ratio J

(b) Thrust coefficient C_T as a function of advance ratio J

Figure 4.5: Engine thrust models as a function of advance ratio J

5

Results

This chapter shows the most important results obtained during wind tunnel testing. The chapter builds up in Sections 5.1 to 5.4 from the unpowered testing of the wing and wing plus nacelle, to the isolated engine testing and finally on to the powered airframe. Section 5.5 provides the results from rake measurements of the engine inlet. Finally, Section 5.6 shows how large the effect of the measured integration effects are on the flight characteristics of the Flying V.

All of the results presented here are obtained using the bookkeeping definitions provided in Appendix A, where all the bookkeeping equations are visualized for easier understanding. Note that in this work, absolute performance numbers and installation contributions are surface plotted as a ”jet” colour range from blue to yellow to red. Relative numbers (interference) are plotted with a colour range with negative values blue and positive values red.

5.1. Wing

Figure 5.1a shows the relation between lift and drag for the Flying V wing. The curve of the model shows a clear kink around $\alpha = 10$ degrees. At low incidence angles, the common quadratic relation between CL and CD can be used to describe the aerodynamic performance of the airframe. It is clear though, that while fitting well at the lower incidence angles, the offset at high angle of attack becomes large. At higher lift coefficients, the curve starts to follow the slope of the $C_L \tan(\alpha)$ relation between lift and drag more closely. This is the variation expected when the lift force is perpendicular to the wing chord, due to leading edge suction being reduced. [55]

Figure 5.1b shows the results obtained by Jones and Cohen for a swept wing model with $60°$ sweep, at $Re = 8*10^6$. Even though the Flying V has a higher aspect ratio, judged from the slope of the quadratic lift drag curve, the similarities between the results of the Flying V and their results are remarkable. Jones and Cohen explain the departure at approximately $C_L = 0.3$ from the classical lift drag relation as the onset of flow separation on a swept wing, which leads to a reduced leading edge suction and lift force perpendicular to the chord. [55] They state that this value corresponds to a lift coefficient of 1.2 with respect to the normal component of the stream velocity. Therefore it is roughly equal to the normal stalling lift coefficient in straight flow. While lift does steadily increase after the ”onset of stall”, this point could also be seen as the point from which vortex lift starts to play a significant role in the total lift production of the wing. Oil flow measurements by Viet [11] confirm this idea, as can be seen from the surface flow topology in Section 2.1. For the Flying V, the angle of incidence corresponding to this lift coefficient is approximately $10°$. Note also the comparably higher lift coefficient at which a pitch break occurs in the Flying V results.

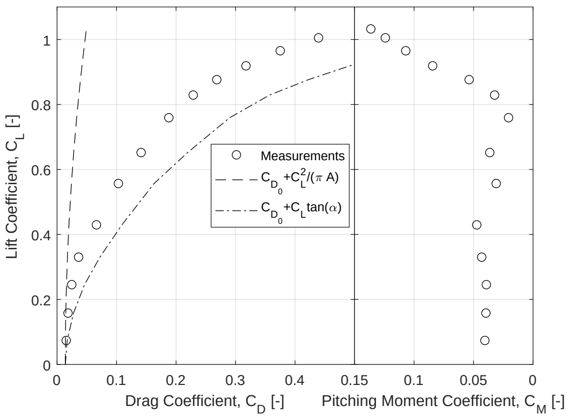

(a) Force measurements indicating "flow separation" on the Flying V, $Re = 1 * 10^6$, $x_{CG} = 1.36m$

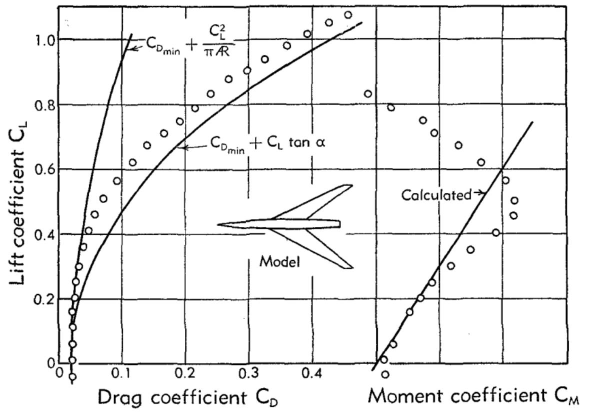

(b) Force measurements indicating flow separation on model with large angle of sweep, $Re = 8 * 10^6$ [1]

5.2. Wing + Nacelle

This section shows the balance results obtained for the wing plus nacelle in through flow conditions at 20m/s. The results at 15m/s are included in Appendix B. First the installation effects of the nacelle are shown, after which the interference effects are given. For the nacelle, these effects seem to be very closely related.

5.2.1. Nacelle Installation

In general, the contribution of the nacelle to total airframe lift and drag is small. The installation contribution I_N of the nacelle is hardly distinguishable from the lift and drag curves of the isolated wing. Only when I_N is plotted separately in Figure 5.2b, its contribution to lift and drag become clear. The circulation of the wing seems to result in a downwash on the nacelle at moderate incidence angles, effectively producing slightly negative inflow angle of attack to the nacelle, thus giving it a negative lift contribution. Figure 5.2a shows that the nacelle has a destabilizing effect from $\alpha = 5°$ to $\alpha = 10°$ and a slight stabilizing effect at high angles of attack beyond the pitch break.

$$I_N = WN - W \tag{5.1}$$

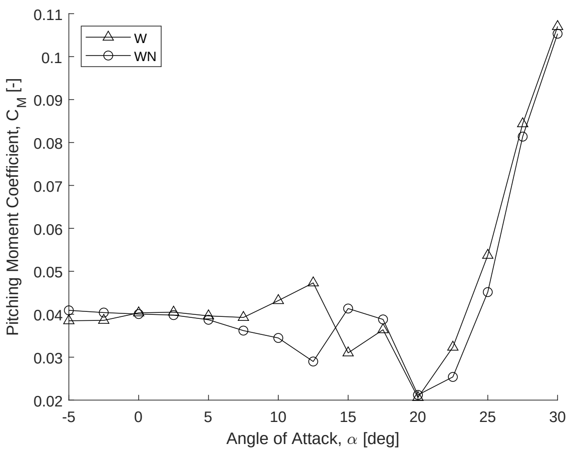

(a) Comparison of C_M vs α for the isolated Wing and the Wing+TFN

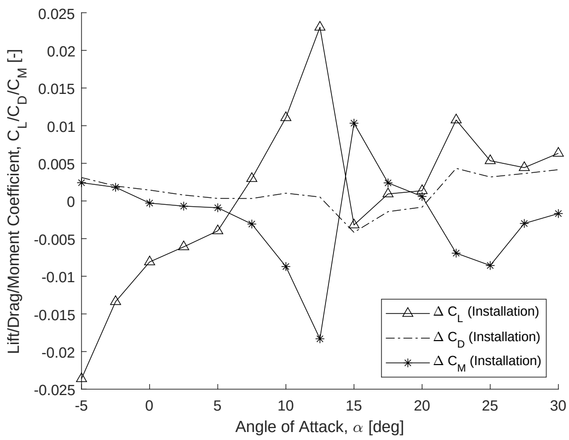

(b) Effect of Nacelle installation

Figure 5.2: Nacelle installation effect I_N

[1] Adapted from: Jones and Cohen[55]

5.2.2. Nacelle Interference

Comparing the installation (Figure 5.2b) and interference (5.3b and5.3c) contributions of the nacelle, it becomes clear that the the interference effects between wing and nacelle dominate the additional forces generated by the nacelle in wing-on condition. I.e. $(WN-(WS-S))-(W+(NS-S)) \ = WN-W$.

The forces generated by the isolated nacelle are plotted in Figure 5.3a for comparison. These forces and moments are identical for both freestream velocities. The nacelle lift and drag contribution in clean air are small at small angles. Therefore, most of the installation effects of the nacelle are a direct effect of the interference between the nacelle and wing elements. The nacelle induces a gradually increasing amount of extra lift in the range between $\alpha = 5°$ and $\alpha = 12.5°$, which then quickly reduces in value and remains small for values of $\alpha = 15°$ and up. The nose down pitching moment induced is proportional to the increased amount of lift. Measurements at $15m/s$ and $20m/s$ show that nacelle interference trends are similar at low incidence angles, but show a very different trend at high angle of attack.

$$If_N = WN - (W + N) \tag{5.2}$$

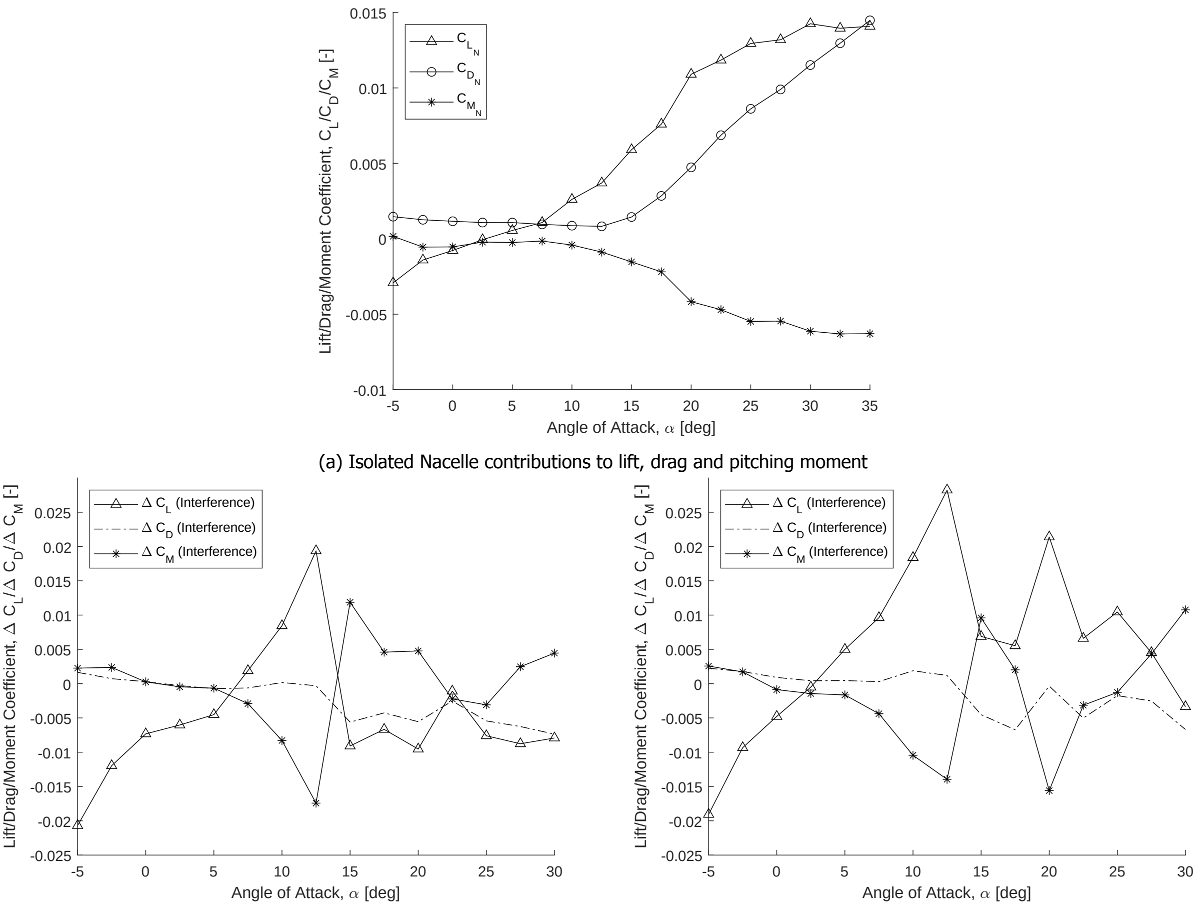

(a) Isolated Nacelle contributions to lift, drag and pitching moment

(b) Wing - nacelle interference effects 20m/s

(c) Wing - nacelle interference effects 15m/s

Figure 5.3: Nacelle interference effect If_N

5.3. Isolated Jet

Measurements of the isolated engine are used to model the thrust generated by the ducted fan. Do note that in this case we are only modeling the jet. Subtracting the measurements of the nacelle and strut from tests in power-on conditions, provides an estimation for the thrust generated (Eq. 5.3). In this way the drag of the nacelle, including any added internal drag in power-on conditions, is directly accounted for as a loss of thrust. Using only the measurements at zero incidence angle allows the construction of an engine model as a function of J, which is further discussed below.

$$E = ENS - NS \tag{5.3}$$

The common definitions of (propeller) thrust coefficient T_C and C_T, as well as advance ratio J are repeated in Equations 5.4, 5.5 and 5.6 below. [19]

$$T_C = \frac{T}{qS} \tag{5.4}$$

$$C_T = \frac{T}{\rho n^2 D^4} \tag{5.5}$$

$$J = \frac{V_\infty}{nD} \tag{5.6}$$

Dimensional analysis in 2.2.2 reveals that CT is a function of Reynolds number, tip Mach number and advance ratio.[19] Plotting the measured data shows that for the used range of power setpoints, CT is linear with J. Reynolds number and tip Mach number can thus safely be disregarded when only using the model at a single free stream velocity. Least squares allows fitting of the model to the data. The resulting models for T_C and C_T are given in Equations 5.9 and 5.7, and plotted in Figures 5.4a and 5.4b. Both the models have an R-squared value larger than 0.99 and a probability value $p << 0.001$ suggesting a very good fit.

$$C_T = aJ + b \tag{5.7}$$

$$C_T = -0.721J + 0.954 \tag{5.8}$$

$$T_C = cJ^{-2} + dJ^2 + e \tag{5.9}$$

$$T_C = 0.025J^{-2} + 0.011J^2 - 0.0297 \tag{5.10}$$

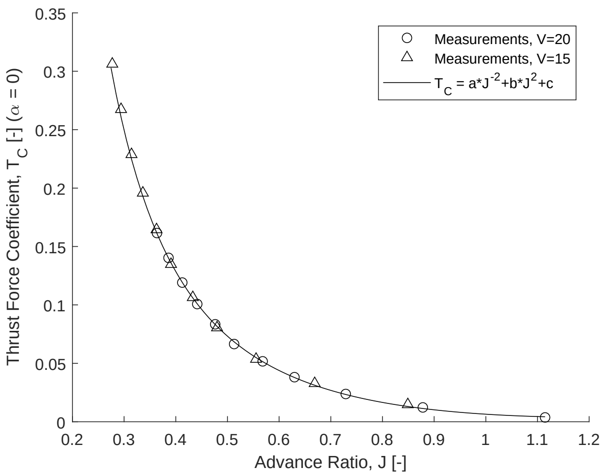

(a) Thrust coefficient T_C as a function of advance ratio J

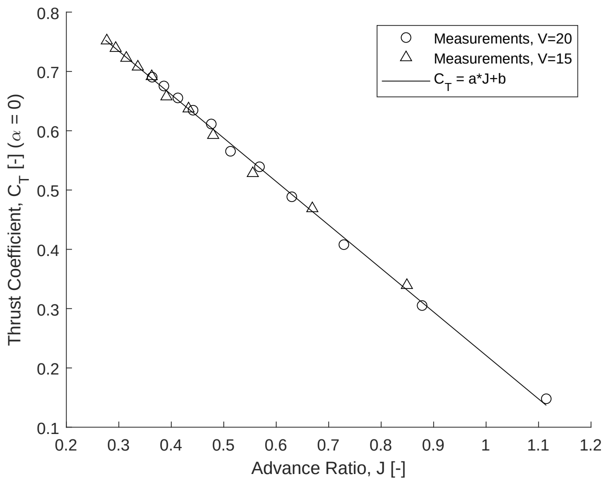

(b) Thrust coefficient C_T as a function of advance ratio J

Figure 5.4: Engine thrust models as a function of advance ratio J

5.4. Wing + Engine

This section describes the main balance results of the campaign, the performance of the powered airframe. Now, to aid the observations made in this section, the results obtained at both free stream velocities are included. Equation 5.11 shows how the presented numbers were obtained from raw measurements using bookkeeping. Figures 5.5a, 5.5c and 5.5e respectively show the lift, drag an moment coefficient at $20m/s$, with a single line per power setpoint. Results at $15m/s$ are shown in Figures 5.6a, 5.6c and 5.6e. It has to be taken into account that the choice is made to add the thrust and drag in drag values, so that negative drag occurs for high power setpoints. (The interference drag penalty that may occur can be observed in their respective plots, later in this chapter) The surface plots (5.5b,5.5d,5.5f,5.6b,5.6d,5.6f) give an overview of the results in the α vs J domain.

$$WEN = WENS - (WS - W) \tag{5.11}$$

Comparing the results obtained at $15m/s$ and $20m/s$ shows that forces and moments match very nicely for equal incidence angle and advance ratio! Lower advance ratios were obtained at $15m/s$ and the observed effects are more pronounced for this relatively higher thrust. From the figures it can be seen that the slope of the lift curve increases for lower J (increasing thrust). Moreover, the drag curves shift left nicely for higher thrust. Finally, the engine induces a gradually increasing nose-down pitching moment for lower J. However the change in C_M is not equal between different incidence angles and power settings. At $15m/s$ and low advance ratios a significantly higher nose down pitching moment is generated than at $20m/s$ and maximum thrust. A minimum C_M of close to -0.04 is generated at $\alpha = 15$ and an advance ratio $J = 0.28$. Irrespective of engine setpoint, the powered aircraft still shows unstable pitch behaviour at $\alpha > 20°$.

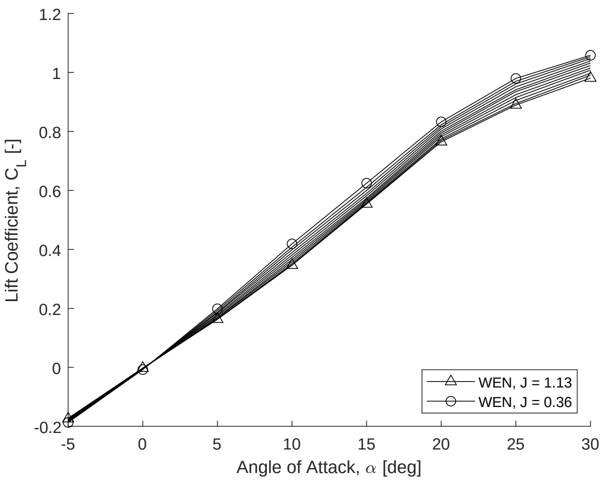

(a) C_L vs α for the wing+engine in power-on conditions

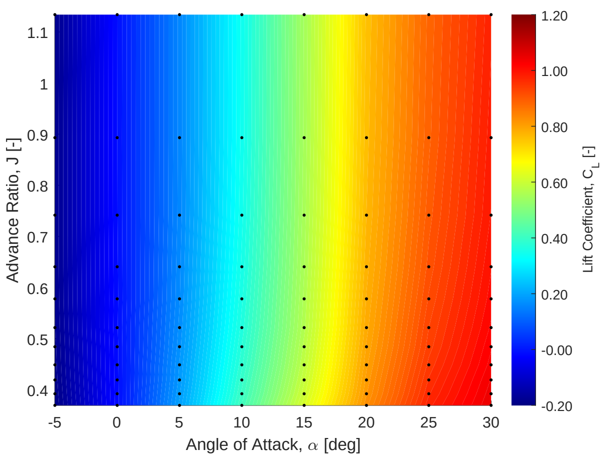

(b) Surface plot showing C_L for combinations of J and α (wing+engine, power-on conditions)

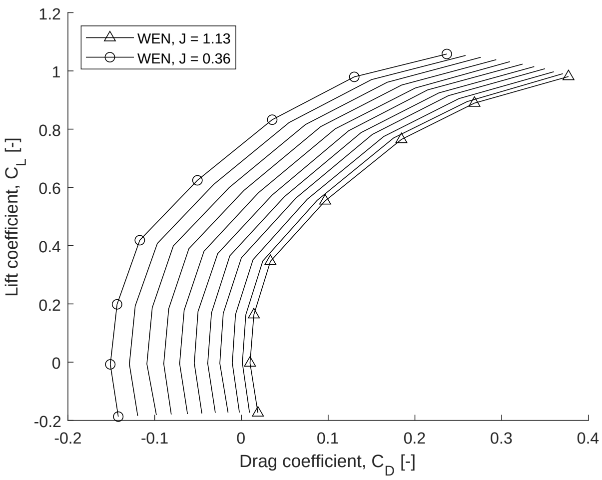

(c) C_L vs C_D for the wing+engine in power-on conditions

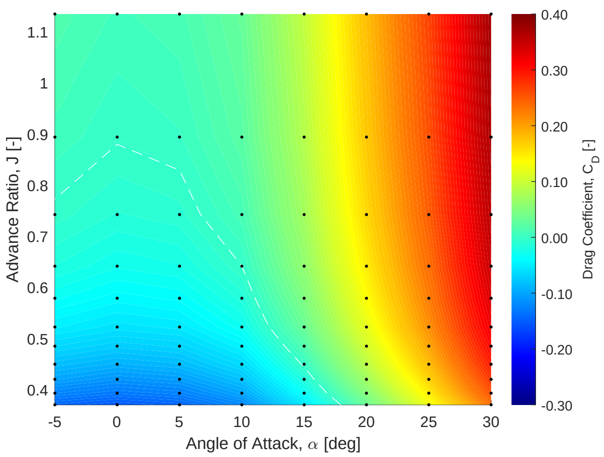

(d) Surface plot showing C_D for combinations of J and α (wing+engine, power-on conditions)

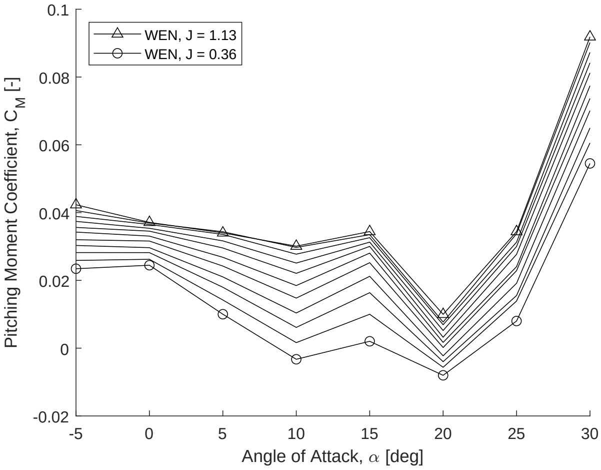

(e) C_M vs α for the wing+engine in power-on conditions

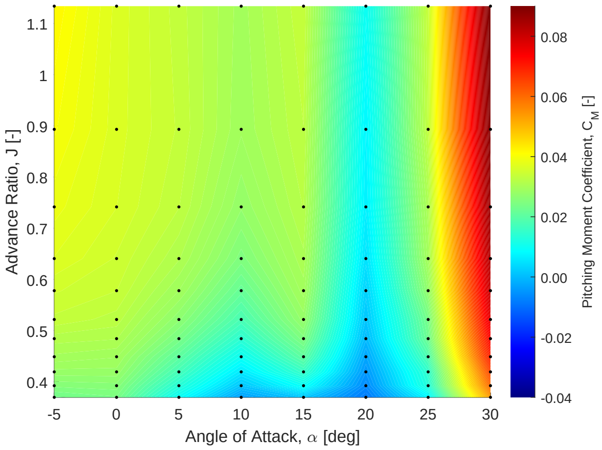

(f) Surface plot showing C_M for combinations of J and α (wing+engine, power-on conditions), white dashed line highlights T=D

Figure 5.5: Powered airframe lift, drag and pitching moment ($V_\infty = 20m/s$, $x_{CG} = 1.36m$)

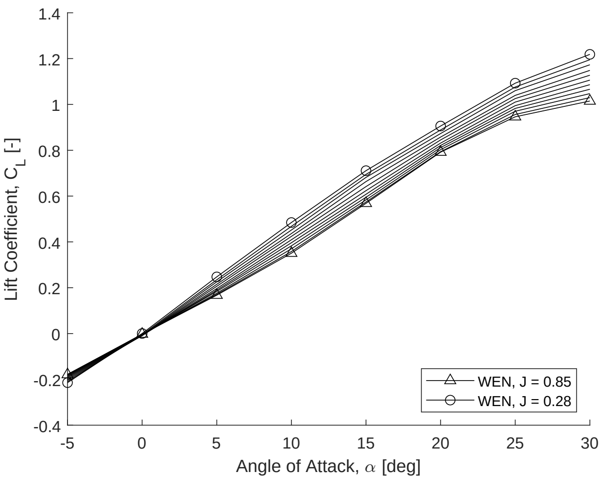

(a) C_L vs α for the wing+engine in power-on conditions $V_\infty = 15m/s$

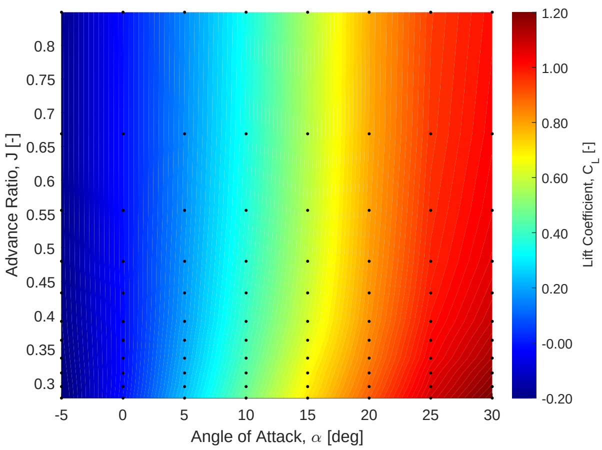

(b) Surface plot showing C_L for combinations of J and α (wing+engine, power-on conditions) $V_\infty = 15m/s$

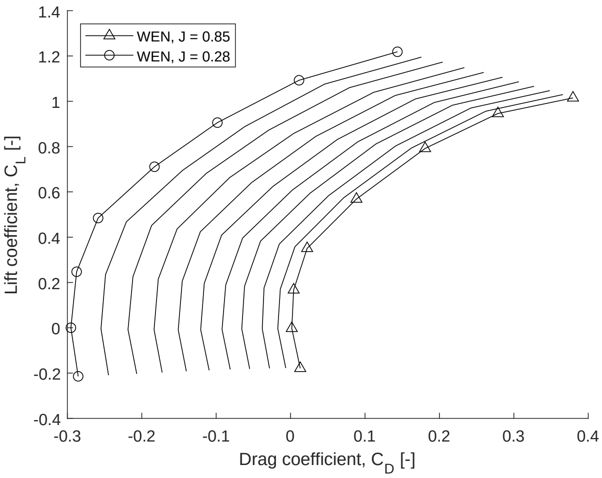

(c) C_L vs C_D for the wing+engine in power-on conditions $V_\infty = 15m/s$

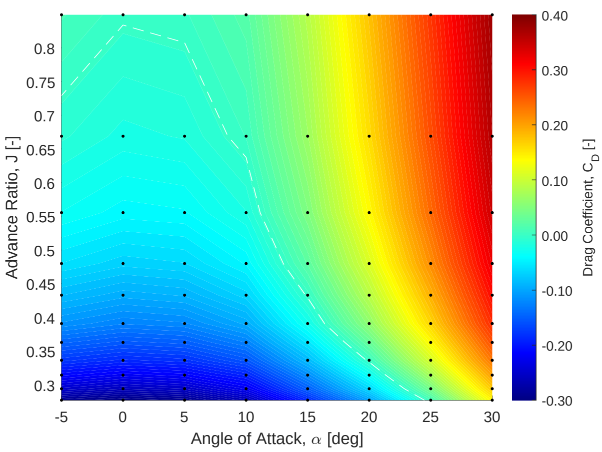

(d) Surface plot showing C_D for combinations of J and α (wing+engine, power-on conditions), white dashed line highlights T=D, $V_\infty = 15m/s$

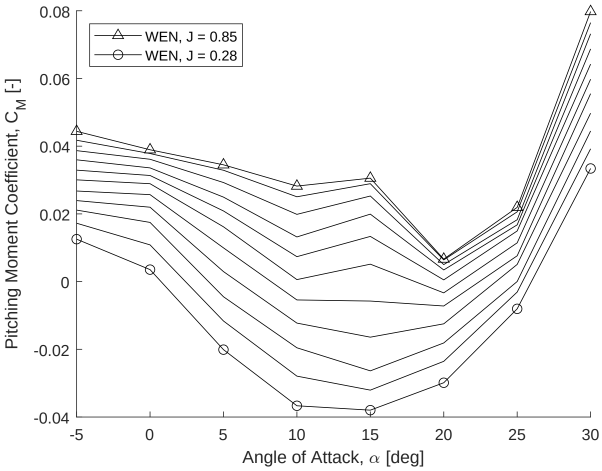

(e) C_M vs α for the wing+engine in power-on conditions $V_\infty = 15m/s$

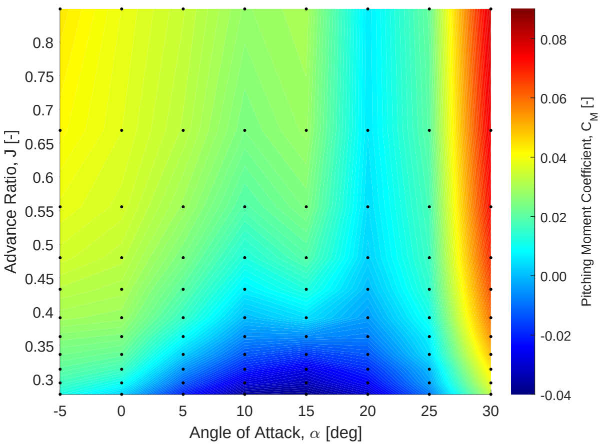

(f) Surface plot showing C_M for combinations of J and α (wing+engine, power-on conditions) $V_\infty = 15m/s$

Figure 5.6: Powered airframe lift, drag and pitching moment ($V_\infty = 15m/s$, $x_{CG} = 1.36m$)

5.4.1. Engine Installation

Not taking any interference into account, the contribution of the engine thrust to the lift, drag and pitching moment could be estimated with basic trigonometry. In terms of lift, one would expect the lift contribution of the engine to be the product of the thrust force coefficient (T_C, in body reference frame) and the sine of the incidence angle. Equally, the change in drag is expected to be proportional to the cosine of alpha. Finally, the change in pitching moment is expected to be the thrust force, multiplied by the relative moment arm of the engine to the balance in balance reference frame ($\Delta Y_{bal}/\bar{\bar{c}}$, Z-direction in body reference frame).

$$\Delta C_L = T_C \sin(\alpha) \tag{5.12}$$
$$\Delta C_D = T_C \cos(\alpha) \tag{5.13}$$
$$\Delta C_M = T_C \Delta Y/\bar{c} \tag{5.14}$$

The observations made in the previous section are depicted as the engine installation effect (Equation 5.15) below. From the Figure 5.7 it is clear that measured installation values for the complete engine deviate from a basic trigonometric contribution of thrust. Lift contribution does not continuously increase with angle of attack, nor does the contribution to pitching moment. Finally, comparing I_P at $15m/s$ and $20m/s$ confirms that the values match for identical α and J, as was suggested in the previous section. Apparently, the total engine contribution is not very sensitive to changes in velocity.

$$I_P = WEN - W = I_N + I_P \tag{5.15}$$

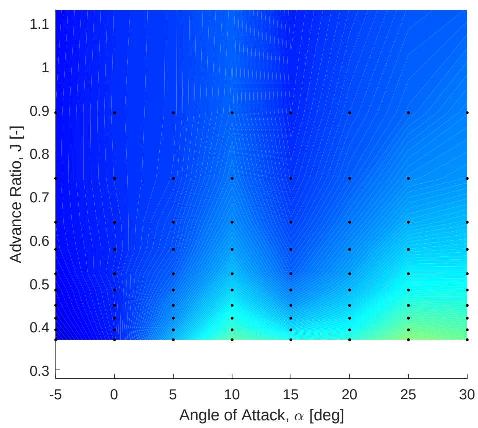

(a) Surface plot showing Engine Installation ΔC_L for combinations of J and α ($V_\infty = 20m/s$)

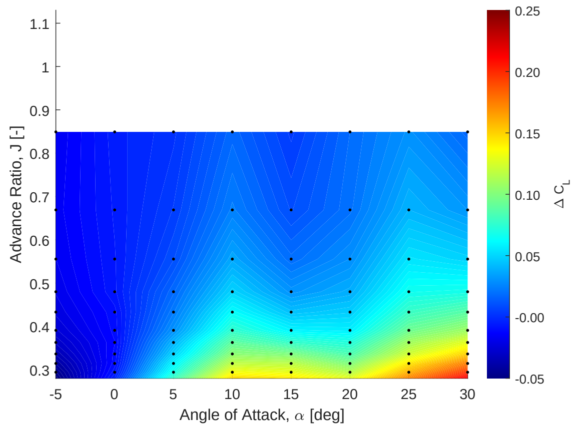

(b) Surface plot showing Engine Installation ΔC_L for combinations of J and α ($V_\infty = 15m/s$)

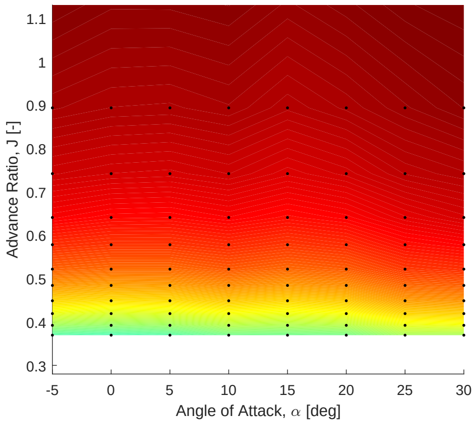

(c) Surface plot showing Engine Installation ΔC_D for combinations of J and α ($V_\infty = 20m/s$)

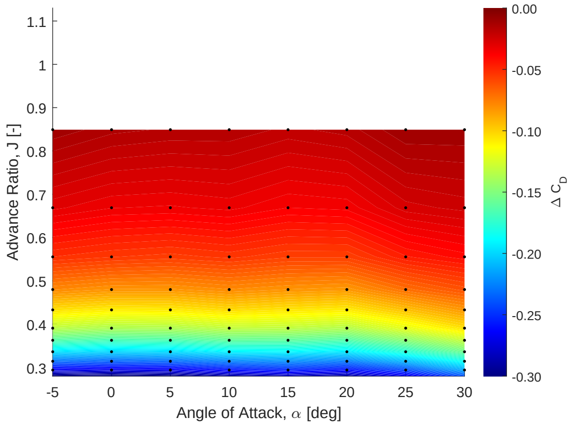

(d) Surface plot showing Engine Installation ΔC_D for combinations of J and α ($V_\infty = 15m/s$)

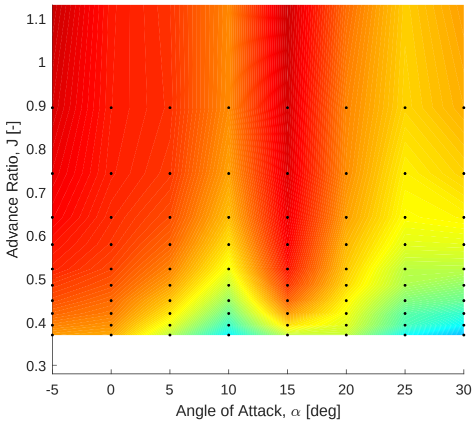

(e) Surface plot showing Engine Installation ΔC_M for combinations of J and α ($V_\infty = 20m/s$, $x_{CG} = 1.36m$)

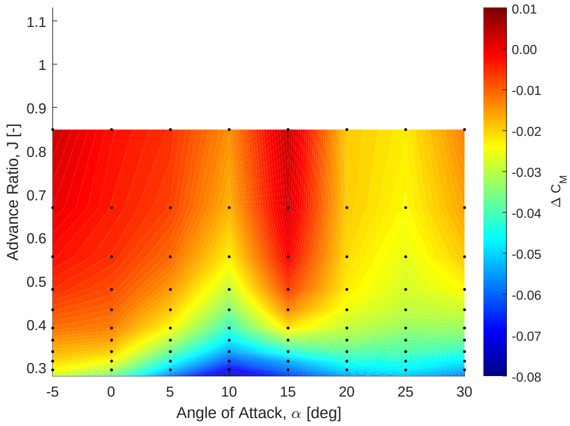

(f) Surface plot showing Engine Installation ΔC_M for combinations of J and α ($V_\infty = 15m/s$, $x_{CG} = 1.36m$)

Figure 5.7: Engine installation effect on lift, drag and pitching moment at $V_\infty = 20m/s$ (left) and $V_\infty = 15m/s$ (right)

5.4.2. Engine Interference

From the previous section it follows that there is significant interference between the wing and engine. The following plots show the interference effects observed between airframe and engine in power-on conditions. It should be noted that this is defined as the sum of the nacelle-wing interference and the engine jet-wing interference, as can be seen in Equation 5.16. The plots again show a linear interpolation between measurement points.

$$I_P = WEN - (W + EN) = I_N + I_E \tag{5.16}$$

In terms of lift the following can be observed from Figure 5.8a. First of all, in the low angle of attack range up to $15°$, the engine interference behaves as predicted. In this region, flow over the wing is still mostly attached, and no vortex lift is produced yet. This can be observed from the results of the isolated wing in Section 5.1. The interference between engine and wing results in some additional lift at these moderate incidence angles, with a maximum ΔC_L of +0.04 at maximum tested thrust setpoint and $\alpha = 10$. This increase in lift can most readily be explained by an increase of suction on the upper wing surface, reducing pressure in front of the engine intake and thus increasing lift, as explained and depicted in Section 2.2.3. The lift increase at high advance ratios at this angle can be accounted to wing-nacelle interference, which was already discussed in 5.2.2. The slight loss of lift at higher incidence angles is also mostly the result of wing-nacelle interference, as it does not seem to change much under the influence of changing thrust.

Due to the difference in relative velocity, a different range of advance ratios was tested for the different free stream velocities. The results obtained at 20m/s and 15m/s are now plotted side by side with matching range of advance ratios on the plots y-axis, so that the interference effects may be compared between free stream flow velocities. At $20m/s$ engine operation has a detrimental effect on wing-body drag above $\alpha = 5°$, resulting in a maximum drag penalty of 60 counts, at $10°$ and full thrust. At this incidence angle this equates to 16.5% of the isolated wing drag! Please do note that distinguishing between loss of engine thrust and increase in airframe drag is not possible with the used setup. However, as will be observed from intake measurements in Section 5.5 a large amount of intake distortion could contribute to an increase in interference drag.

At incidence angles lower than $5°$ engine operation is somewhat beneficial, with a maximum contribution to thrust due to interference of approximately 20 counts. At $V_\infty = 15m/s$ a quite different trend is observed. While some interference drag remains at $10°$, higher incidence angles show much more benefit due to interference. Drag is actually reduced by up to 100 counts (5% of wing drag) at $20°$ angle of attack, mostly due to jet interference. This can be confirmed from Figure 5.10d.

Finally, Figure 5.8e and 5.8f show pitching moment trends corresponding to the effects shown in lift. An additional nose down pitching moment is observed between $5°$ and $12.5°$ angle of attack, followed by an increase in nose up pitching moment from $12.5°$ to $22.5°$.

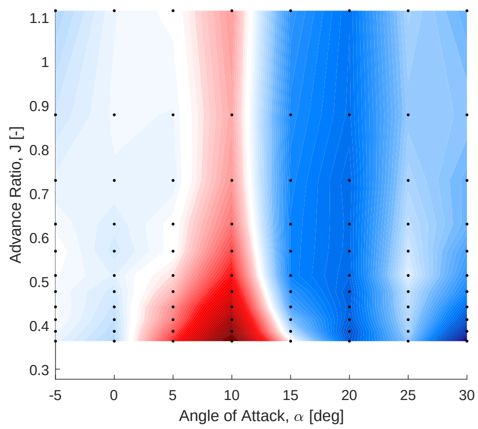

(a) Surface plot showing Engine Interference ΔC_L for combinations of J and α ($V_\infty = 20m/s$)

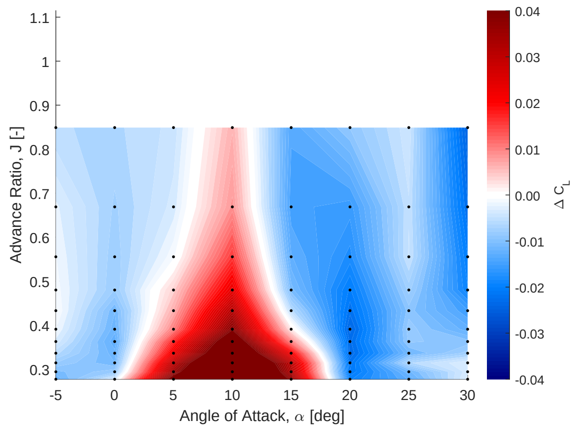

(b) Surface plot showing Engine Interference ΔC_L for combinations of J and α ($V_\infty = 15m/s$)

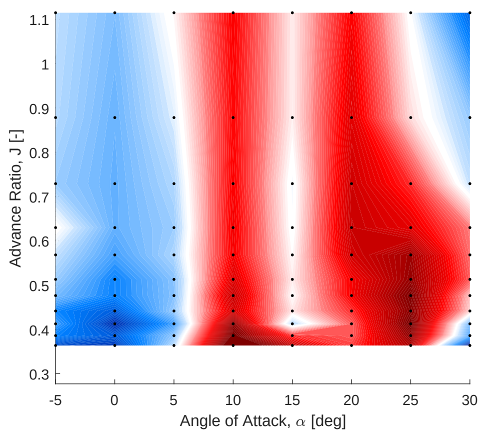

(c) Surface plot showing Engine Interference ΔC_D for combinations of J and α ($V_\infty = 20m/s$)

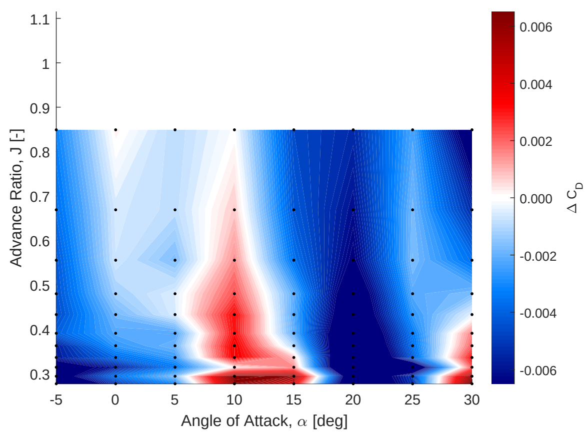

(d) Surface plot showing Engine Interference ΔC_D for combinations of J and α ($V_\infty = 15m/s$)

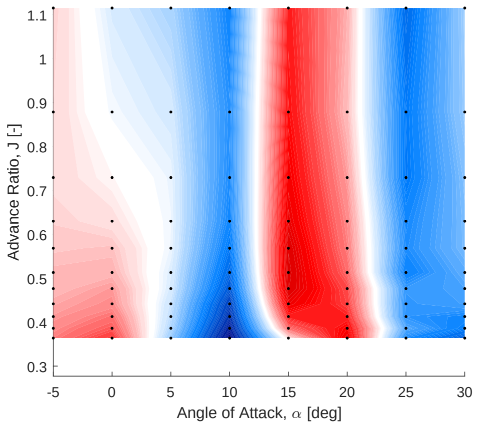

(e) Surface plot showing Engine Interference ΔC_M for combinations of J and α ($V_\infty = 20m/s$, $x_{CG} = 1.36m$)

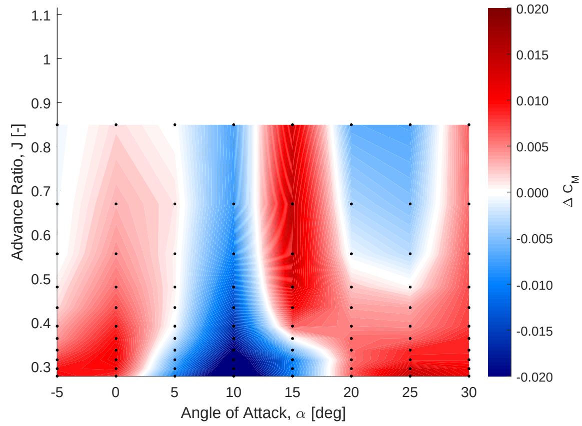

(f) Surface plot showing Engine Interference ΔC_M for combinations of J and α ($V_\infty = 15m/s$, $x_{CG} = 1.36m$)

Figure 5.8: Engine interference effect on lift, drag and pitching moment at $V_\infty = 20m/s$ (left) and $V_\infty = 15m/s$ (right)

5.4.3. Jet Installation Effects

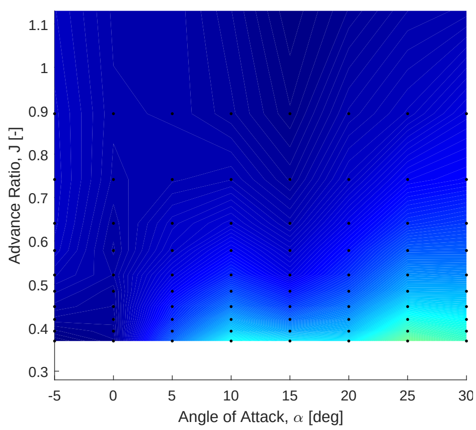

(a) Surface plot showing Jet Installation ΔC_L for combinations of J and α ($V_\infty = 20m/s$)

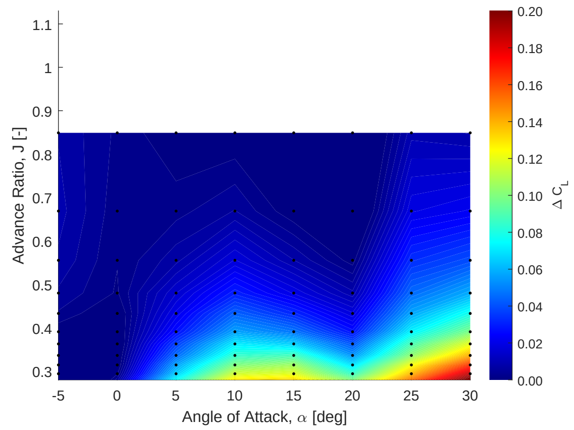

(b) Surface plot showing Jet Installation ΔC_L for combinations of J and α ($V_\infty = 15m/s$)

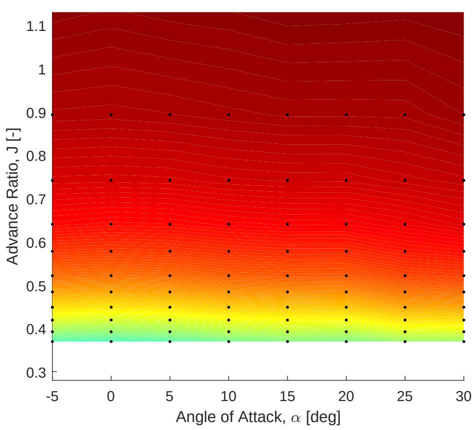

(c) Surface plot showing Jet Installation ΔC_D for combinations of J and α ($V_\infty = 20m/s$)

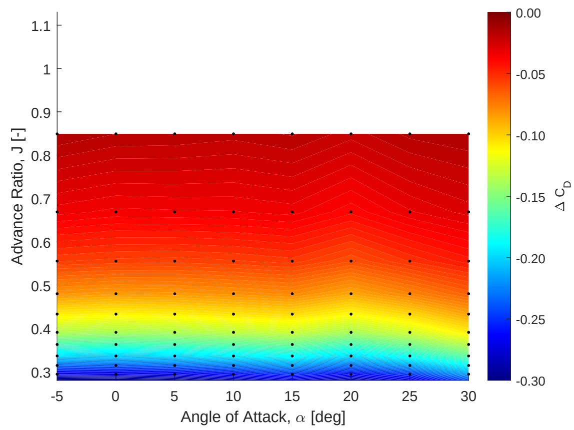

(d) Surface plot showing Jet Installation ΔC_D for combinations of J and α ($V_\infty = 15m/s$)

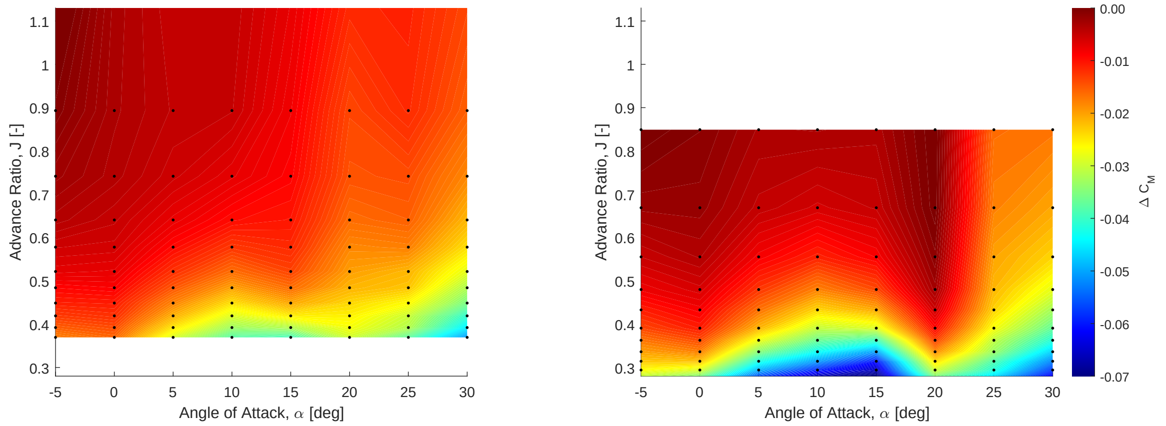

(e) Surface plot showing Jet Installation ΔC_M for combinations of J and α ($V_\infty = 20m/s$, $x_{CG} = 1.36m$)

(f) Surface plot showing Jet Installation ΔC_M for combinations of J and α ($V_\infty = 15m/s$, $x_{CG} = 1.36m$)

Figure 5.9: Jet installation effect on lift, drag and pitching moment at $V_\infty = 20m/s$ (left) and $V_\infty = 15m/s$ (right)

Subtracting the effect of the nacelle from the engine installation shows the installation effect purely generated by the jet (Eq. 5.17). The standard relations stated in 5.4.1 seems to hold better for the jet installation effect, than the total engine installation. The plots in Figure 5.9 confirm that at high advance ratios, installation of the jet is small. The measurements are mostly equal to TFN condition, except for some slight changes in pitching moment at higher incidence angles. At low advance ratios the figures clearly show the same behaviour as the full engine integration at low advance ratios.

$$I_E = WEN - WN \tag{5.17}$$

5.4.4. Jet Interference Effects

Interference effects of the engine jet If_E are shown in Figure 5.10.

$$If_E = (WEN - WN) - (EN - N) \tag{5.18}$$

First of all, Figure 5.10a confirms that the increase in lift observed around 10° at high thrust is generated through interference with the engine jet. From Figure 5.10c we can see a couple of things. Clearly the engine interference drag penalty is mostly angle of attack dependent. From an incidence angle of approximately 7°, all the way up to high angles of attack, there is an increase in perceived drag for the installed jet. A small, but significant decrease is visible in the range between $+5^\circ$ angle of attack and -5°, at high thrust setting.

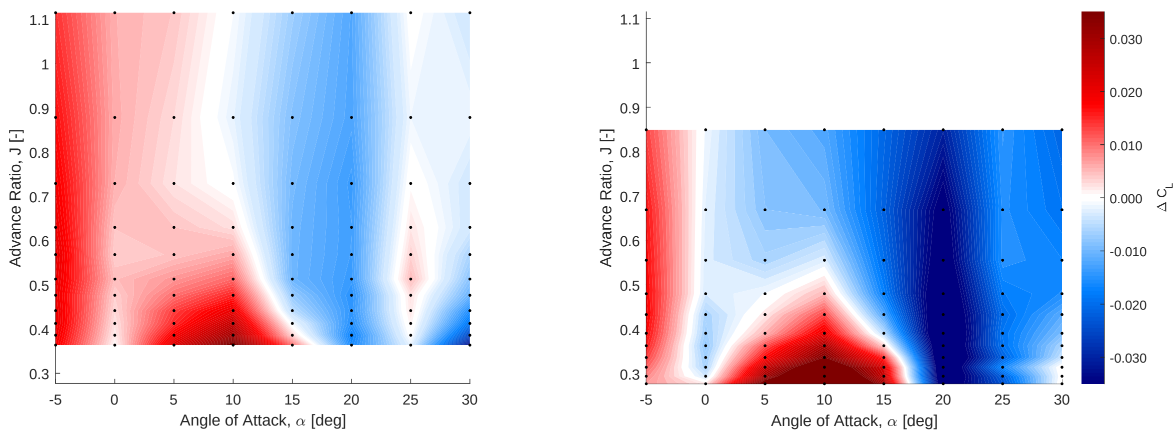

(a) Surface plot showing Jet interference ΔC_L for combinations of J and α ($V_\infty = 20m/s$)

(b) Surface plot showing Jet interference ΔC_L for combinations of J and α ($V_\infty = 15m/s$)

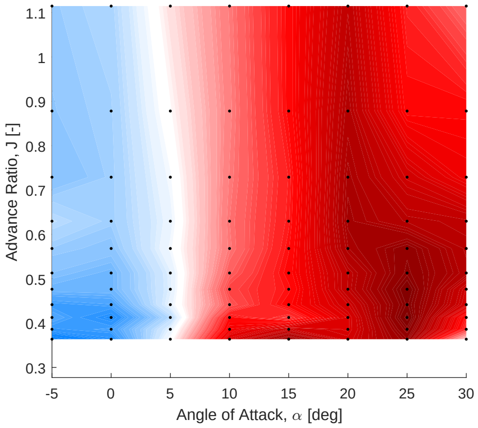

(c) Surface plot showing Jet interference ΔC_D for combinations of J and α ($V_\infty = 20m/s$)

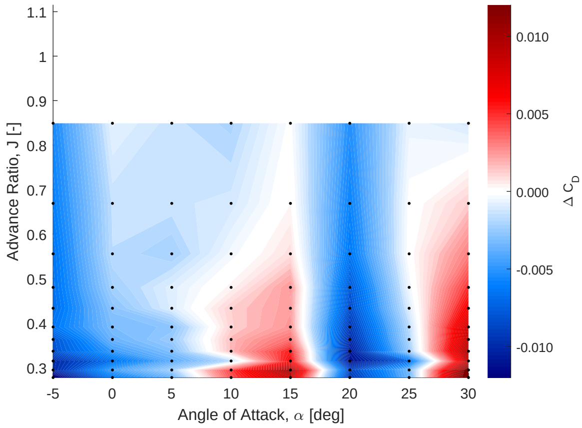

(d) Surface plot showing Jet interference ΔC_D for combinations of J and α ($V_\infty = 15m/s$)

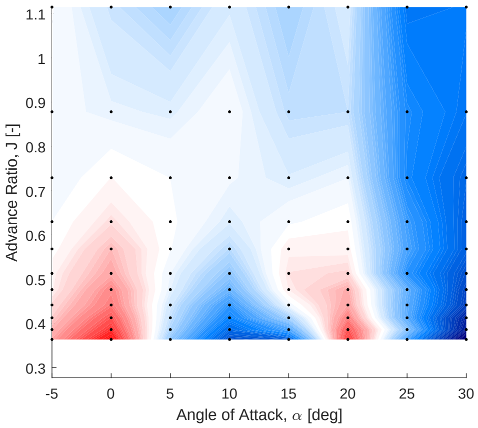

(e) Surface plot showing Jet interference ΔC_M for combinations of J and α ($V_\infty = 20m/s$, $x_{CG} = 1.36m$)

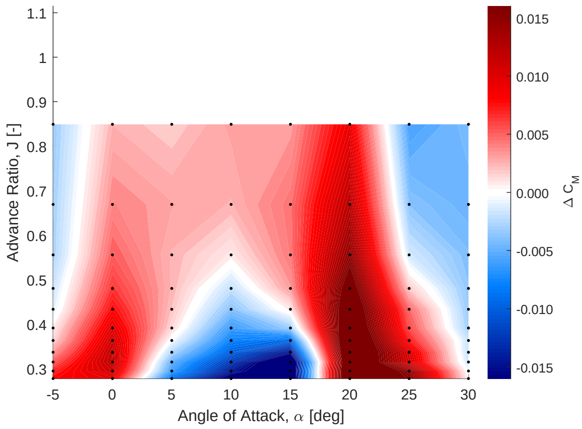

(f) Surface plot showing Jet interference ΔC_M for combinations of J and α ($V_\infty = 15m/s$, $x_{CG} = 1.36m$)

Figure 5.10: Jet interference effect on lift, drag and pitching moment at $V_\infty = 20m/s$ (left) and $V_\infty = 15m/s$ (right)

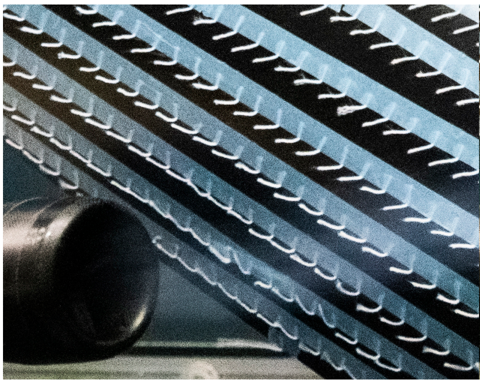

(a) $\alpha = 5°$, Power: Idle

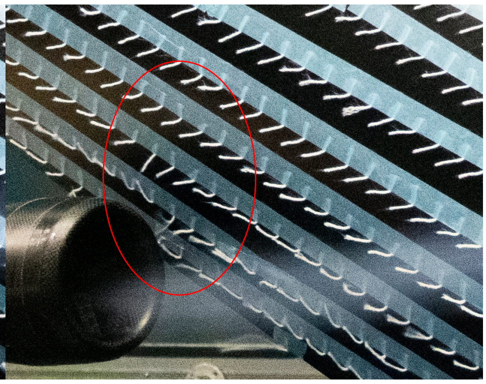

(b) $\alpha = 5°$, Power: On

Figure 5.11: Comparison of surface flow visalized by tufts between engine idle (left) and full thrust (right)

When looking at the moment plots of the jet interference effect at $20m/s$, it can be seen that for higher advance ratios, combined with low to moderate angles of attack, the jet interference is quite low. This is mostly favourable for cruise conditions. Only at higher thrust settings and incidence angles the thrust dependent effects become noticeable. The nose up tendencies observed centered around $\alpha = 0°$ and $\alpha = 20°$ for high thrust settings are of smaller magnitude than the nose down tendencies at $\alpha > 25°$

and centered around $\alpha = 12.5°$ for high thrust setpoints. Also here the difference between velocities is very noticable, with thrust effects showing a much larger magnitude at $V_\infty 15m/s$.

The photos in Figure 5.11 show some difference between near-idle and maximum power conditions on the suction side surface at $\alpha = 5°$. The displacement of the tufts show that the increased suction of the engine "pulls" the surface flow towards the engine inlet. At the relatively low flight velocity of $20m/s$ the region of influence extends quite far outboard, as highlighted by the red circle. Pressure differences further inboard are harder to distinguish from the tufts, since the general direction of the idle condition surface flow is already pointed towards the engine intake. Nevertheless, it can be concluded that the engine suction has some effect on the upper surface pressure distribution near the engine intake.

5.5. Intake Results

This Section deals with the intake total pressure measurements taken on a plane near the inlet of the nacelle. As explained in Section 2.2.4, inlet conditions of the nacelle are an important design driver for proper engine performance. In case of the Flying V, the flow over the wing affects the inflow of the engine. A wide variety of definitions have been used in literature to describe the conditions on the inlet plane of an engine. [32] Results are presented according to the following definitions for the distortion coefficient 5.19, and the average distortion over a sixty degree sector of the inlet plane DC(60) 5.20. It has to be noted that the distortion coefficient is relative to the average total pressure in the free stream, while DC(60) provides a value relative to the average total pressure on the measured plane.

$$DC = \frac{(p_{0_\infty} - p_0)}{\bar{q}} \tag{5.19}$$

$$DC(60) = \frac{(\bar{p}_0 - \bar{p}_{0_{(60)}})}{\bar{q}} \tag{5.20}$$

The dynamic pressure at the engine inlet face is estimated using the assumption of incompressible flow, and the momentum difference required to generate the measured thrust of the engine. (Section 2.2.2)

5.5.1. Total Pressure Recovery

This section shows the basic inlet measurement results in terms of total pressure. All figures show a front view of the inlet plane of the left wing engine. The wing is situated at the bottom of the figure. In other words, the view is rotated 90 degrees from the wind tunnel reference frame. The small black circles represent the measurement points on the inlet plane. The colour data shown on the figures is interpolated linearly between the measurement point, resulting in the conditions shown below. Walter and Starkey [56] show that linear interpolation is a very adequate method to reconstruct inlet conditions from measurement samples, provided that the density of points is high enough.

The careful reader will note that the maximum total pressure loss is limited to 0.5% of the free stream total pressure, while results from NASA shown in Section 2.3 include losses a full order of magnitude higher. While this may not seem like much, the dynamic pressure at which this test is conducted is approximately $245Pa$, while the NASA tests were conducted at free stream dynamic pressures between $480Pa$ and $3000Pa$. In a test case with free stream $V_\infty = 20m/s$, a 0.5% total pressure loss equates to 200% of the free stream dynamic pressure.

In the figures below, only pressure recovery and distortion plots are provided in wing-on conditions. To show that the incoming flow is undisturbed, irrespective of incidence angle and engine installation, total pressure measurements in wing-off conditions are included in Appendix D. Only some stall on the lower lip of the through-flow nacelle at $25°$ angle of attack. Stall is prevented when installing the engine due to the improved pressure gradient on the lip. Additionally, these figures show that the pressures recorded in TFN and idle conditions match. Only idle and power-on conditions are thus compared here to keep the section concise. Power-on conditions are the maximum power that could be reached using the current setup.

The full pressure recovery at the intake in wing-off conditions signifies that the pressure loss on the inlet plane in wing-on conditions is purely caused by the wing. In the following Figures (5.12a), the front view of the left wing nacelle is plotted, with the wing root left of the nacelle and the wing tip on the right. The engine position relative to the wing results in a right bottom quadrant situated closest to the wing. The left bottom quadrant has a slight gap from the wing trailing edge to the nacelle, visible in the top view of Figure 3.2.

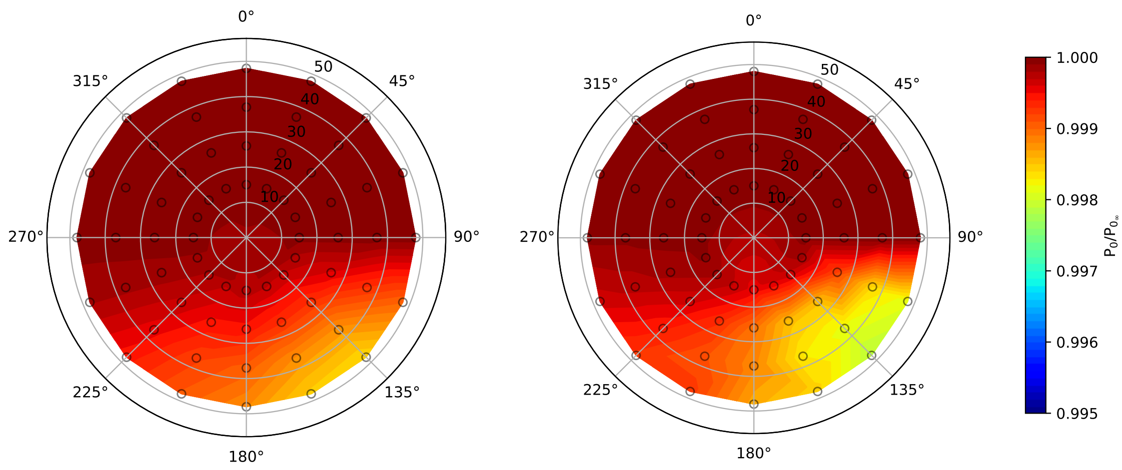

(a) $V_\infty = 20m/s$, $\alpha = 5^\circ$, Power:Idle

(b) $V_\infty = 20m/s$, $\alpha = 5^\circ$, Power:On

Figure 5.12: Intake total pressure recovery ($V_\infty = 20m/s$, $\alpha = 5^\circ$)

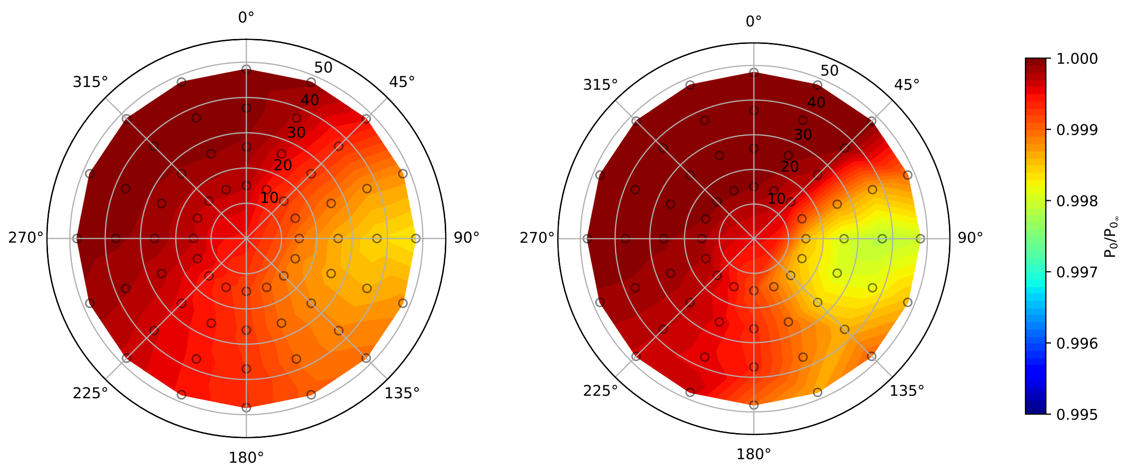

(a) $V_\infty = 20m/s$, $\alpha = 15^\circ$, Power:Idle

(b) $V_\infty = 20m/s$, $\alpha = 15^\circ$, Power:On

Figure 5.13: Intake total pressure recovery ($V_\infty = 20m/s$, $\alpha = 15^\circ$)

Consequently, the highest pressure losses at $\alpha = 5^\circ$ are incurred in the right bottom quadrant. At $V_\infty = 20m/s$ and $\alpha = 5^\circ$ the maximum pressure loss in idle conditions is approximately 0.15% of the total pressure. In power-on conditions the pressure loss increases to more than 0.2% of the total pressure (80% of the free stream dynamic pressure). At 15° the main region of pressure loss moves up according to increase in angle of attack (Figures 5.13a and 5.13b). The % pressure loss in idle and power-on conditions is equal to the loss incurred at 5°.

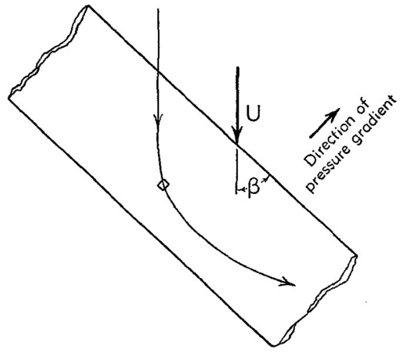

Figure 5.15: The effect of yaw β on the path of a particle in a separated boundary layer [2]

In the $\alpha = 25°$ condition, a much larger part of the intake suffers from a significant pressure loss. At idle thrust the bottom half of the intake receives lower energy flow, with maximum losses in the bottom right quadrant and minimum losses in the top right. Again, the losses are amplified by in increase of thrust. At this incidence angle, the flow around the wing has partially separated. The change of gradient on the engine intake could be a result of the outboard moving separated boundary layer of the swept wing (Figure 5.15), and the inboard motion of the outer flow. The photographs in Figure 5.17 show how the engine inflow is clearly curved progressively more inwards due to the swept wing at higher angles of attack. This might induce some sidewash on the outboard part of the nacelle lip at higher incidence angles. Note that while tufts are included in the pictures above, all pressure measurements on the inlet plane are done without the presence of tufts on the wing surface.

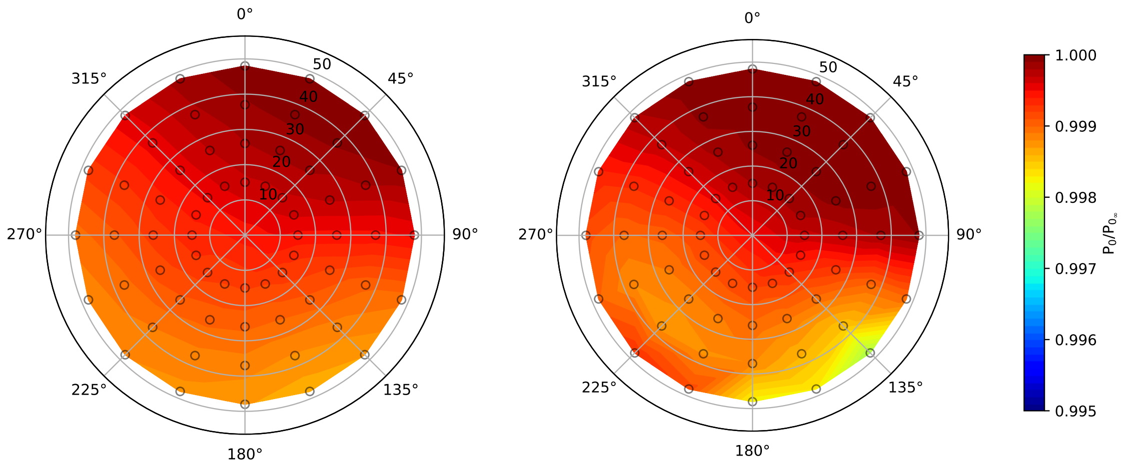

(a) $V_\infty = 20m/s$, $\alpha = 25°$, Power:Idle

(b) $V_\infty = 20m/s$, $\alpha = 25°$, Power:On

Figure 5.14: Intake total pressure recovery ($V_\infty = 20m/s$, $\alpha = 25°$)

Finally, comparing the results obtained at $V_\infty = 30m/s$ to those at $20m/s$ shows that total pressure losses increase with higher free stream velocity. While the area of highest pressure loss is still the same part of the bottom right quadrant, the maximum loss in power-on conditions is now 0.5% of free stream total pressure (93% of the free stream dynamic pressure at $V_\infty = 30m/s$). Judging from these results, the pressure losses incurred on the engine inlet may very well have have significant effect on the thrust delivered by the engine. In any case, the engine receives significantly less massflow than in on-design conditions. Unfortunately, no intake measurements were done at a freestream velocity of 15m/s. Thus, no direct conclusions can be made about the relation between inlet conditions and the difference in engine interference drag penalties incurred at $V_\infty = 15m/s$ and $V_\infty = 20m/s$.

[2]Source: Jones and Cohen [55]

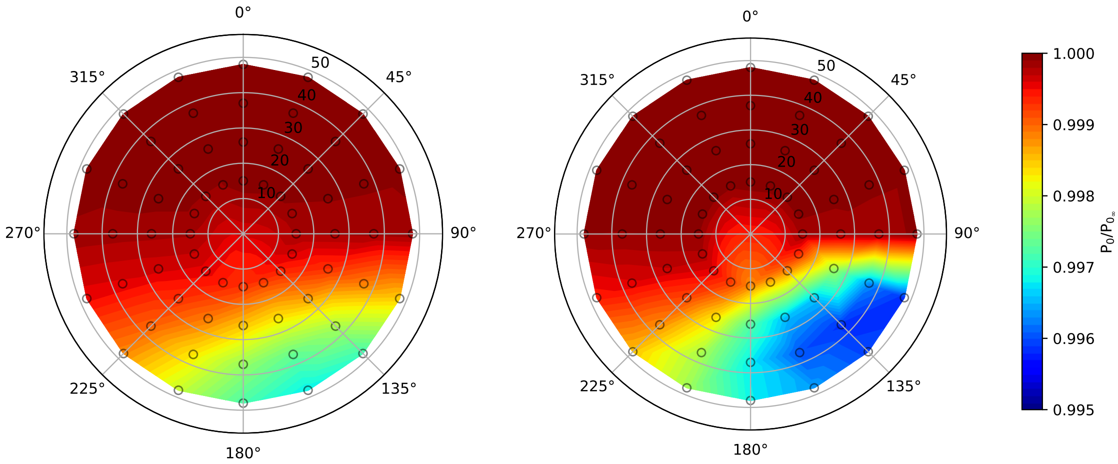

(a) $V_\infty = 30m/s$, $\alpha = 5^\circ$, Power:Idle

(b) $V_\infty = 30m/s$, $\alpha = 5^\circ$, Power:On

Figure 5.16: Intake total pressure recovery ($V_\infty = 30m/s$, $\alpha = 5^\circ$)

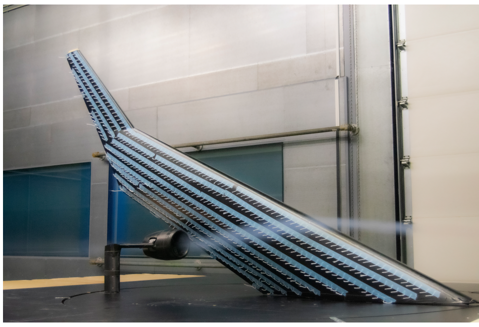

(a) $\alpha = 5^\circ$

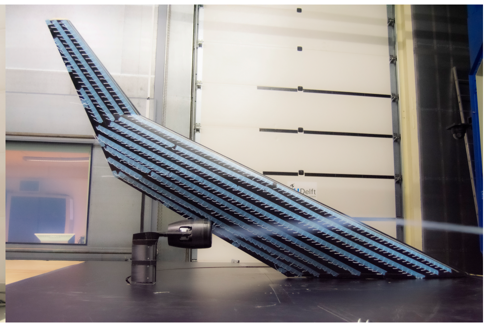

(b) $\alpha = 5^\circ$

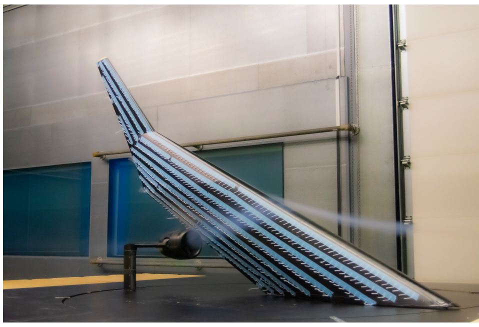

(c) $\alpha = 15^\circ$

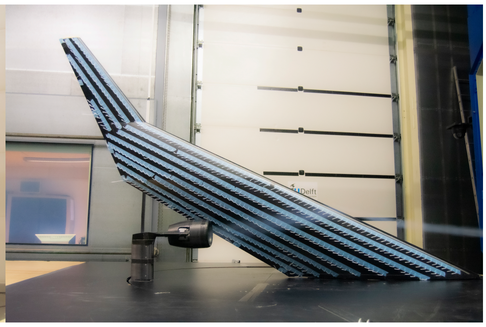

(d) $\alpha = 15^\circ$

(e) $\alpha = 25^\circ$

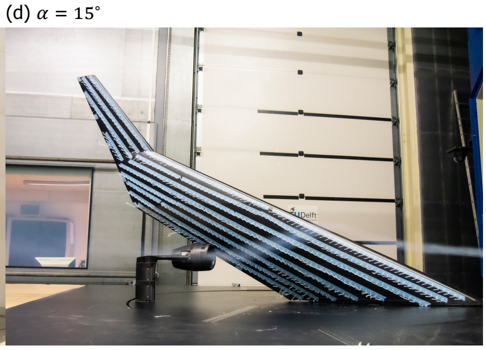

(f) $\alpha = 25^\circ$

Figure 5.17: Smoke visualization of the main trajectory followed by air ingested into the engine at $V_\infty = 20m/s$, $\alpha \in (5^\circ, 15^\circ, 25^\circ)$

5.5.2. Intake distortion

Next to the inlet total pressure loss, measurement results are shown as a distortion definition in this section. The definitions for Distortion Coefficient DC and DC60 as given in Equations 5.19 and 5.20, are used. The following figures thus show the loss of pressure on the intake face relative to the **local average dynamic pressure** $\bar{q}$ in the intake. Flow velocity on the inlet plane is computed using the engine C_T model (Eq. 5.7) and incompressible flow equations. As explained in Section 2.2.2, Trancossi [18] shows that the assumption of incompressible flow can readily be used to obtain an estimation of the average velocity in the nacelle inlet. Viscous losses in the engine are inherently included in the thrust measurements in the wind tunnel.

In the following figures (5.18 and 5.19) the sector of the engine intake with the highest distortion DC(60) is highlighted with a black line. The colour scale is used to project DC values. The sector with highest distortion was computed by looping over all 60 degree sectors and selecting the sector with the highest value for DC(60). Note that DC relates the pressure difference to free stream total pressure, while DC(60) uses the average total pressure on the measurement plane as a reference value.

While the previous section shows that total pressure recovery is lower at higher velocities and power setpoints, the trend in flow distortion is somewhat different. Indeed, the distortion DC increases with velocity (Figure 5.18). However, increasing thrust actually lowers distortion due to the increase in local dynamic pressure. Figure 5.19 shows idle and power-on conditions side by side. Note that the color scale for DC is altered to show the distorted area in both idle and power-on conditions. Apparently the increase in dynamic pressure due to thrust is greater than the relative loss in pressure at these higher intake flow speeds.

Finally, values for DC(60) are summarized in the table below. Seddon states that DC(60) values greater than 0.1 are generally deemed unacceptably high, and are likely to have an adverse effect on fan operation.[32] Clearly, the DC(60) values obtained at idle thrust and an α of 5° and 15° are thus quite high. Due to the overall lower total pressure and the definition of DC(60), the flow blanketing the engine at low power setpoints produces a lower value for DC(60). However, more important is DC(60) in on design conditions. Barely acceptable performance is measured in the conditions closer to cruise. However, the intake is expected to experience DC(60)>0.1 for actual cruise conditions, at lower than full power thrust setpoint and higher velocities.

V_∞ $[m/s]$	α $[^{\circ}]$	Thrust	DC(60) $[-]$
20	5	Idle	0.202
20	5	Power-On	0.039
30	5	Idle	0.242
30	5	Power-On	0.086
20	15	Idle	0.233
20	15	Power-On	0.044
20	25	Idle	0.134
20	25	Power-On	0.025

Table 5.1: DC(60) values for combinations of V_∞, α and Thrust

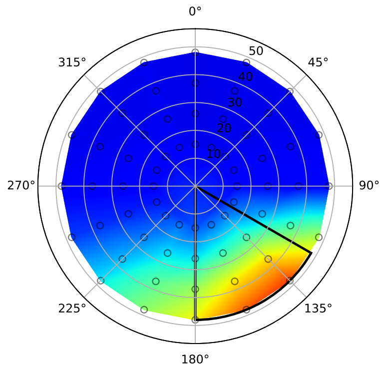

(a) $V_\infty = 20m/s$, $\alpha = 5°$, Power:Idle

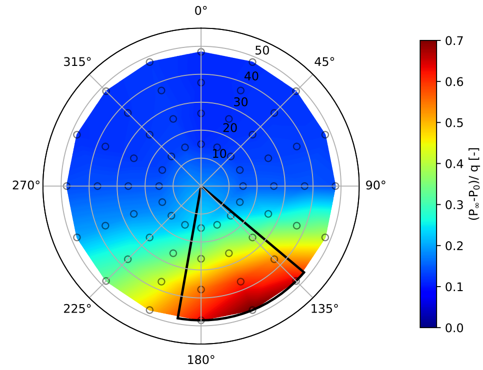

(b) $V_\infty = 30m/s$, $\alpha = 5°$, Power:Idle

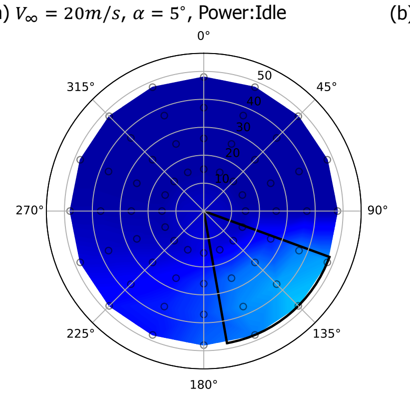

(c) $V_\infty = 20m/s$, $\alpha = 5°$, Power:On

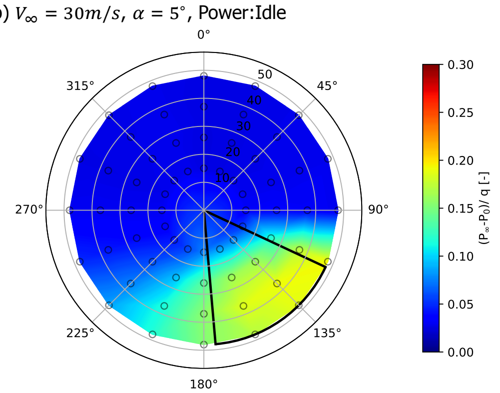

(d) $V_\infty = 30m/s$, $\alpha = 5°$, Power:On

Figure 5.18: Comparison of distortion measurements ($V_\infty \in (20m/s, 30m/s)$, $\alpha = 5°$)

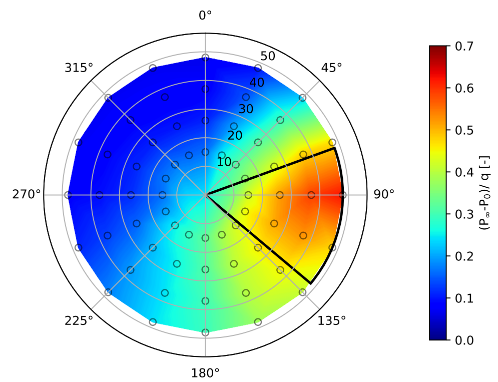

(a) $V_\infty = 20m/s$, $\alpha = 15°$, Power:Idle

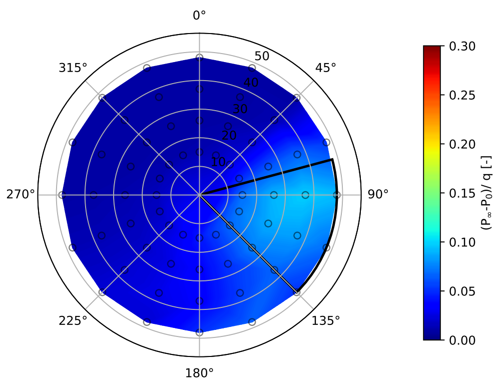

(b) $V_\infty = 20m/s$, $\alpha = 15°$, Power:On

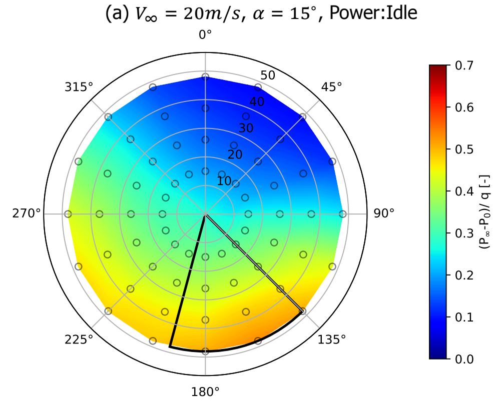

(c) $V_\infty = 20m/s$, $\alpha = 25°$, Power:Idle

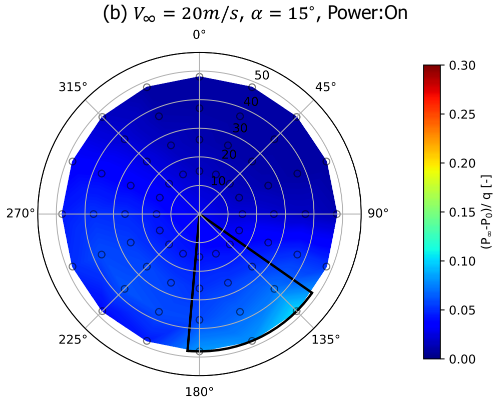

(d) $V_\infty = 20m/s$, $\alpha = 25°$, Power:On

Figure 5.19: Comparison of distortion measurements at idle and full thrust ($V_\infty = 20m/s$, $\alpha \in (15°, 25°)$)

5.6. Implications on Flight Performance

The interaction effect between engine and wing will have an effect on the flight characteristics of the model. This section provides an investigation into these effects. A conservative estimation of the free air flight performance can be made using the wind tunnel data. (Better overall L/D performance is expected at lower effective angle off attack for the flight model, as is explained in Section 2.4 on wind tunnel corrections.) To explain the effect of the engine on flight performance, two cases are further explored in this section; Trimmed steady flight and takeoff rotation.

Trimmed Flight

First of all, the influence of the engine on the trimmable flight regime is investigated in three flight scenarios; steady horizontal flight, maximum climbing flight and engine idle gliding flight. For each case, the combination of required engine power and control surface deflection are the main figures of interest. To investigate these flight conditions, a trim routine was implemented in MATLAB's fmincon. It combines gridded data of the measured engine-on aircraft performance (WEN) with a first order estimation of previously measured elevator control power.

To this end, the effect of control surfaces as measured by Palermo and Ruiz Garcia is linearized. From their results, the control effectiveness is constant in angle of attack and the change for velocity is small. [10][12] Their effect is assumed completely uncoupled from any engine effects. The outboard spanwise position of the control surfaces relative to the engine is assumed to be enough to justify the validity of this assumption. For the CG at 1.36m, the combined control power of the two most inboard control surfaces $C_{M_\delta} = C_{M_{\delta 1}} + C_{M_{\delta 2}} \approx -0.264 rad^{-1}$, in which it is assumed that both control surfaces have an equivalent deflection. The effect of control surface deflection on lift produced is taken into account as $C_{L_\delta} = C_{L_{\delta 1}} + C_{L_{\delta 2}} \approx 0.241 rad^{-1}$. The small effect of control surface deflection on drag is neglected in this analysis. A limit to the control surface deflection available for trim is given as $\delta \in [-10, 10]°$. The remaining control surface deflection of control surface two will be available for maneuvering, while the outboard control surface is reserved for roll control.

As additional bounds, the maximum speed of the fan is limited to 26800 RPM and idle engine condition is defined as an advance ratio of 1.045. This ensures that any chosen value is represented in the measured data. For any velocity lower than 20m/s, the measurement results (WEN) at 15m/s and 20m/s are linearly interpolated for a given combination of J and α. For any velocity higher than 20m/s, the values obtained at 20m/s are used. While the interference between engine and wing will change with increasing Reynolds numbers, this should provide a good first estimate. The model can be summarized in the following relations for the total lift, drag and pitching moment:

$$C_L = C_{L_{WEN}} + \delta C_{L_\delta} = f(J, \alpha, \delta) \tag{5.21}$$
$$C_D = C_{D_{WEN}} = f(J, \alpha) \tag{5.22}$$
$$C_M = C_{M_{WEN}} + \delta C_{M_\delta} = f(J, \alpha, \delta) \tag{5.23}$$

To find the power and trim required for the estimated flight envelope, first the minimum flight velocity is estimated. The pitch break at 20 degrees angle of attack is limiting the flight envelope, resulting in a minimum flight velocity V_{min} for the clean wing at $\alpha = 20°$:

$$V_{min} = \sqrt{\frac{W}{0.5 \rho C_{L_{20°}}}} = 16.5 m/s \tag{5.24}$$

Adding some margin, the trim routine will be used to find solutions in the velocity domain $V \in [17, 40] m/s$. The resulting minimization problem, has the variables [Fan Speed, angle of attack α, control surface deflection δ and climb gradient γ] as a design vector. For level flight γ is set to zero and for gliding flight the Fan Speed is set to match an advance ratio of 1.045. The objective functions for the optimization problems for the three flight scenarios are the following:

$$J_{horizontal} = \min T = \min J \tag{5.25}$$
$$J_{climb} = \min -RC \tag{5.26}$$
$$J_{glide} = \min -\gamma \tag{5.27}$$
$$\tag{5.28}$$

Subject to the equations for steady (climbing) flight [57]:

$$\sum F_Z = L - W\cos\gamma = 0 \tag{5.29}$$
$$\sum F_X = T - D - W\sin\gamma = 0 \tag{5.30}$$
$$\sum M = C_{M_{WEN}} + \delta C_{M_\delta} = 0 \tag{5.31}$$

Results of the trim routine are summarized in Figure 5.20. First let us take a look at the overall performance of the model with the tested engine system. Figure 5.20a shows the power requirement for cruise flight and the power available at maximum engine RPM. In this figure, the maximum thrust available is estimated using Equation 5.10. The minimum propulsive power required for cruise is 544W, achieved at a flight velocity of 27 m/s and a corresponding angle of attack $\alpha = 7.8°$. Plenty of power remains over the full velocity range, which allows the model to achieve positive rate of climb at any of the investigated velocities (Figure 5.20b). Maximum climb performance in terms of rate of climb is realized in the range between $25m/s$ and $30m/s$, with a rate of climb of $4.5m/s$. Figure 5.20c shows that the angle of attack for a given angle of attack varies slightly depending on thrust setting. As expected, at higher angle of attack (lower velocity) the contribution of thrust to lift becomes larger. This results in a lower angle of attack for the full thrust climbing flight than the gliding flight, with level flight at an angle of attack in between those values.

Finally, the most interesting observations can be made regarding the control surface deflection required to reach trimmed conditions. The trim characteristics in Figure 5.20 shows the three lines for level flight, maximum climb and best glide. Due to the additional positive pitching moment by the engine, more negative (upward) control surface deflection is required to reach equilibrium. The most positive values are required in gliding flight. While the full range of conditions considered proves to be trimmable, quite a large extent of the positive control surface deflection range is required. Therefore, it should be noted that windmilling or even blocked engines are not taken into consideration yet. The amount of nose up pitch generated by a windmilling engine was not measured, though looking at the presented results they are very likely to require more nose down elevator than the $10°$ limit imposed in this investigation.

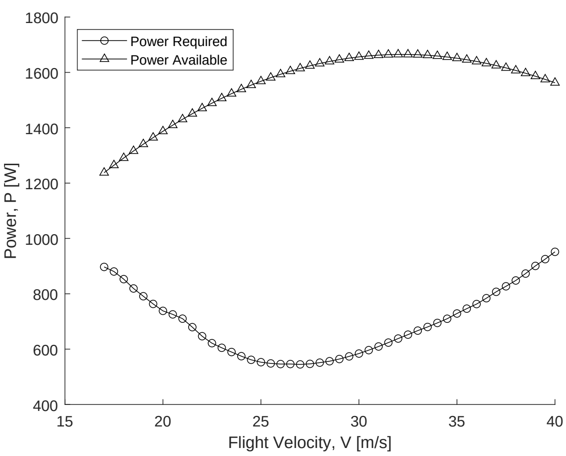

(a) Power required for level flight and power available

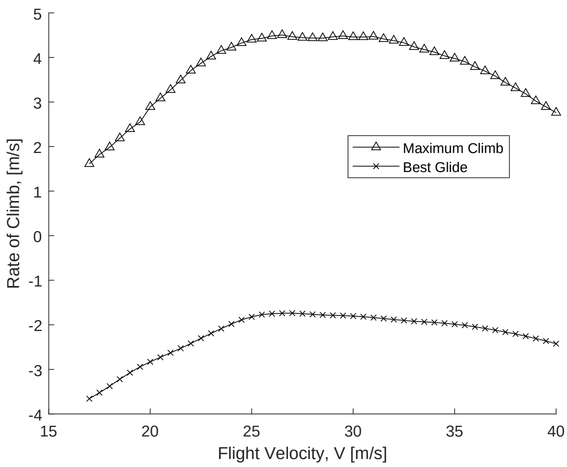

(b) Maximum rate of climb at full power and (rate of descend) at idle conditions

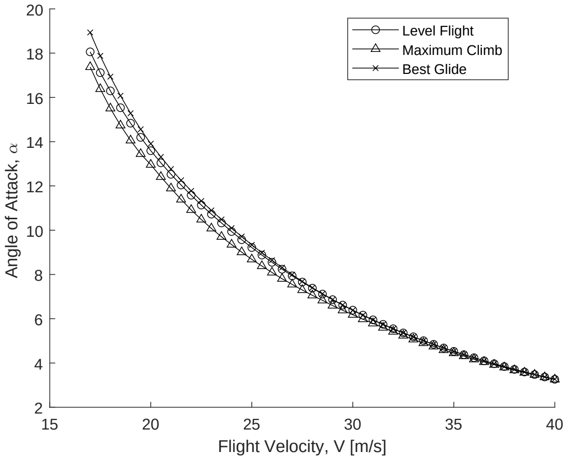

(c) Trimmed angle of attack α

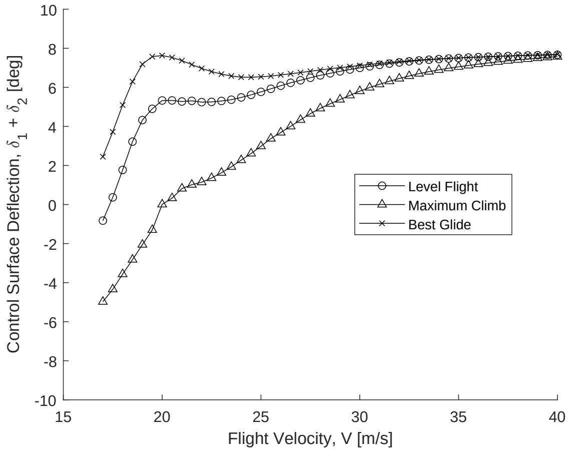

(d) Control surface deflection δ required for trim

Figure 5.20: Trimmed flight conditions for flight velocity $V \in [17, 40]$

Finally, it provides some insight to show how the interference between wing and engine influences the trim curve of the aircraft. Figure 5.21 shows the level flight trim curves for the aircraft with engine installed (the same condition as Figure 5.20) and the combination of isolated component test results. A very similar trim curve to the one obtained from isolated components is found when modelling the engine as a thrust vector acting at a height 0.091m above the center of gravity. Figure 5.21b shows that due to interference effects, the required control surface deflection for trim is reduced at flight velocities between 22m/s and 35m/s. On the other hand, at low velocities, some more elevator deflection is required. Finally, one can see from Figure 5.21a that the power required is increased significantly for most velocities, with only a minor decrease in power requirement above 31 m/s. These conclusions can quickly be verified when comparing them to the engine interference measurements of Figure 5.8a, 5.8c and 5.8e.

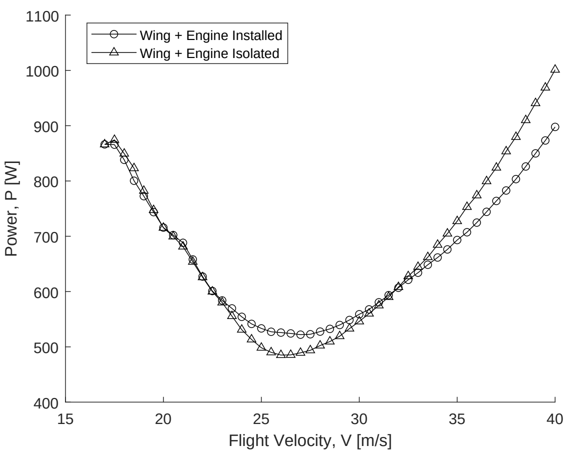

(a) Power required for trimmed flight

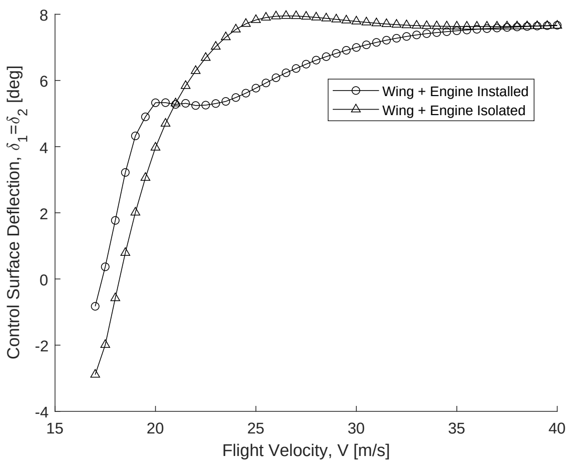

(b) Control surface deflection δ required for trim

Figure 5.21: Trimmed flight conditions for flight velocity $V \in [17, 40]$, showing the difference between isolated component measurements and the installed configuration

Minimum Rotation Velocity

Another limiting case is the minimum velocity required for rotation, with the axis of rotation being the axle of the main landing gear. In this scenario the objective is to find the minimum required velocity at which full negative elevator (up) deflection results in a zero net moment around the axis of rotation. Full deflection is again defined to be limited at $\delta = 10°$. All the forces and moments acting on the aircraft have to be translated from the center of gravity to this axis of rotation. The longitudinal distance between the CG and main landing gear x_{mlg} is approximately 0.15m. The vertical distance between the CG and main landing gear z_{mlg} is approximately 0.3m. Thus, the objective is to find minimum velocity at which:

$$\sum C_{M_{axle}} = C_M + (C_L - \frac{W}{qS})\frac{x_{mlg}}{\bar{\bar{c}}} + (C_D - C_T)\frac{z_{mlg}}{\bar{\bar{c}}} = 0 \tag{5.32}$$

Solving for this velocity using the dimensions of the current design, an installation angle of $0°$ and previously imposed bounds of $\delta \in (-10°, 10°)$ results in an unacceptably high minimum rotation velocity of $28m/s$! The lack of lift provided by the wing at this installation angle, combined with the high net thrust on a relatively long main landing gear and a lack of pitch up authority will make for a very long takeoff roll.

While at this stage of the takeoff roll $D < T$ and $L < W$, reducing the longitudinal distance from the center of gravity to the main landing gear, reducing the vertical distance from the center of gravity to the main landing gear and increasing the "installation angle" of the wing all result in a reduction of the velocity required for rotation. For example, $x_{mlg} = 0.05m$, $z_{mlg} = 0.2m$ and an installation angle $\alpha_{in} = 7°$ result in a much more reasonable $19.7m/s$ required for rotation. Alternatively, if a level aircraft fuselage is preferred or scrape angle constraints are not met, the longitudinal stability margin of the main landing gear can be further reduced to $x_{mlg} = 0.03m$ and maximum deflection of control surface two can be included to allow for rotation. This would lower the required speed to approximately $19.0m/s$, while keeping the landing hear height $z_{mlg} = 0.3m$ and installation angle $\alpha_{in} = 0°$, at the cost of a smaller landing gear stability margin.

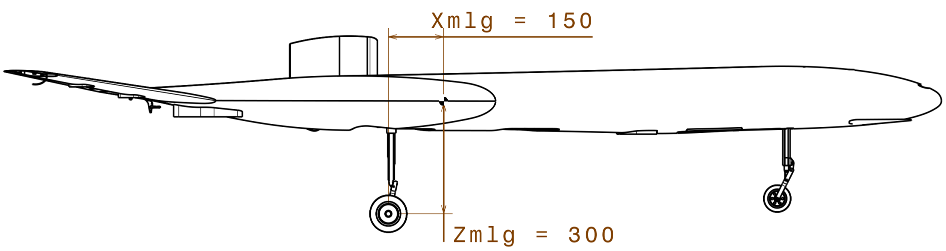

Figure 5.22: Distances between the approximated center of gravity and the main landing gear axle (dimensions in mm)

6 Conclusion

Engine integration effects were tested on a 4.6% scale half model of the Flying V in a low speed wind tunnel test. The main objective of the campaign was to quantify engine integration effects and assess their impact on the low speed performance of the Flying V sub-scale flight testing model.

Isolated measurements of the engine were used to model its performance. In the tested velocity domain, the thrust generated by the engine is proven to be only a function of the advance ratio J and free stream conditions. The sensitivity of the models acquired for thrust coefficients C_T and T_C with respect to free stream velocity were validated using measurements at velocities of 15m/s and 20m/s.

Bookkeeping the balance measurements of isolated components and the integrated setup allowed quantification and identification of the interference effects between the wing, nacelle and the engine jet. Statistical analysis has shown that the method used is accurate enough to produce significant results for the magnitude of the measured interference effects. Interference effects were broken down into contributions by the nacelle and contributions by the engine jet (thrust effects).

The following observations can be made about the complete engine interference. Additional lift is generated through jet inference, with maximum value of 400 counts of lift obtained at 10° angle of attack and full thrust. At $20m/s$ engine operation has a detrimental effect on wing-body drag above $\alpha = 5^{\circ}$, resulting in a maximum drag penalty of 60 counts (16.5% of the isolated wing drag!) at 10° and full thrust. Do note that distinguishing between loss of engine thrust and increase in airframe drag is not possible with the used setup. At incidence angles lower than 5° engine operation is somewhat beneficial, with a maximum contribution to thrust due to interference of approximately 20 counts. At $V_{\infty} = 15m/s$ a quite different trend is observed. While some interference drag remains at 10°, higher incidence angles show much more benefit due to interference. Drag is actually reduced by up to 100 counts (5% of wing drag) at 20° angle of attack, mostly due to jet interference. Finally, pitching moment is altered due to interference. An increased nose down pitching moment is observed between 5° and 12.5° angle of attack, followed by an increase in nose up pitching moment from 12.5° to 22.5°.

Total pressure measurements were taken on the engine inlet plane to assess intake flow distortion. The intake receives some flow with significantly reduced energy due to the wing. The highest pressure loss observed is between 80% and 90% of the free stream dynamic pressure, at full thrust conditions. Angular distortion (DC(60)) values observed at idle thrust and an α of 5° and 15° are approximately 0.2, much higher than an acceptable 0.1. Barely acceptable intake conditions are measured in the test conditions closer to cruise. However, the intake is expected to experience DC(60)>0.1 for actual cruise conditions, at lower than full power thrust setpoint and higher velocities.

Using linear interpolation of the measured data, the impact of integration effects on trimmed flight conditions were investigated. Maximum steady climb, level flight and optimum glide were computed with a center of gravity at $x_{CG} = 1.36m$ from the nose. The aircraft is shown to be trimmable with control surface deflections $\delta \in (-10°, 10°)$ on the two inboard control surfaces in these flight conditions. Interference effects are shown to have a direct effect on required control surface deflection and power consumption in cruise. Power requirement increases by up to 8% between flight velocities 22m/s and 31m/s, and reduces at velocities higher than $33m/s$, by up to 11% at $40m/s$. Finally, minimum speed required for takeoff rotation is shown to require repositioning of the main landing gear, assuming the same elevator deflection bounds. Reducing the main landing gear stability margin to 30mm and increasing allowable elevator deflection results in a rotation velocity below $19m/s$.

It should finally be noted that better results in terms of L/D are expected for the flight model than measured in the wind tunnel. Wind tunnel corrections show a large L/D performance increase, as well as a decrease in effective angle of attack relative to the wind tunnel geometric angle of attack. For example, lift to drag ratio for level flight at $35m/s$ is estimated to be 8.2% higher than measured, while optimum climb at $26m/s$ is expected to result in a 16.5% increase in L/D. However, validity of corrections at higher incidence angles become increasingly doubtful.

Recommendations

The presented work has produced as many new questions as the insights it has gained into the performance of the SSFT model configuration. The following improvements to the used setup are recommended to further the understanding of presented results.

First of all, addition of an encoder to the motor axle and a feedback loop to the speed controller, would allow testing at exact RPM numbers. This would reduce the uncertainty present in motor setpoint. The increased precision may allow the investigation of boundary layer ingestion on the thrust and power consumption of the engine at different engine locations.

Including a separate engine balance would further aid these investigation. It allows more elaborate bookkeeping to further trace the sources of interference contributions. The additional information allows changes in thrust to be recorded, so that interference effects on the airframe and the engine can be decoupled in thrust on conditions. The additional information would also allow the effect of the distortion on engine performance to be quantified. While the exact effect of the measured distortion on the engine is unknown, adding an engine balance allows the tolerance of the engine to distortion to be tested

Possible topics of further interest that come to mind are:

- Visualization of the interference effects.
- Further investigation of engine inflow to understand source of distortion. This could include inflow measurements with a swirl rake to further understand the nature of the flow distortion.
- CFD simulations could be used to understand both the nature of the observed interference and inlet distortion. A sidenote to this is that the boundary layer behaviour and development of vortex structures depend heavily on the computational method and choice of discretization.
- Experimentally, investigation of side-slip conditions would definately provide added value.
- Engine windmilling conditions are not included in the presented results. Control surface deflection required for operation in OEI conditions is therefore still an unknown. Also, the amount of pitch up moment due to drag, generated by two windmilling or even blocked engines is to be investigated.
- Investigation of pylon design and effect on integration.
- While these tests are conducted to further the chances of a succesfull flight test, data could be used the other way around as well. Flight testing results could be used to check correlation with wind tunnel data.
- Investigation of half model configuration vs full span model testing in the wind tunnel.

A

Bookkeeping Definitions

This appendix provides the definitions used throughout the rest of this work. Results of different measurement runs are combined to investigate the interaction between components. This appendix describes the bookkeeping done to arrive at the installation and interference effects of the propulsion system.

Bookkeeping Engine Strut

First of all, the forces and moments acting on the strut are subtracted from measurements taken on the isolated nacelle and engine. This is done for both idle and powered conditions to arrive at the forces and moments acting on the isolated nacelle and engine respectively (Equations A.1,A.2,A.3 and A.4).

$$N = NS - S \tag{A.1}$$

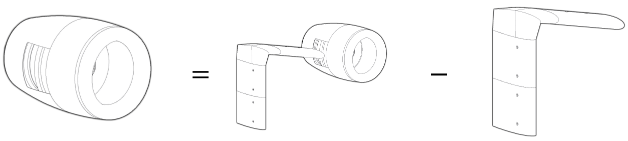

(A.2)

$$EN = ENS - S \tag{A.3}$$

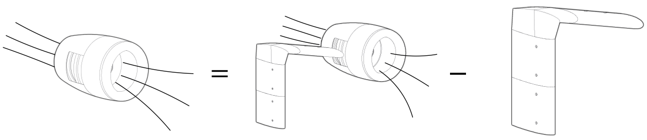

(A.4)

Next, something similar can be done for the strut in wing-on conditions. The measured results and deltas between wing-on and wing off conditions are treated in Appendix B for completeness. In the following definitions, it is assumed that the downstream effects of the wing on the strut are much larger than the upstream effect of the strut on the wing. This allows the forces of the engine strut, **under influence of the wake of the wing**, to be taken as:

$$S_w = WS - W \tag{A.5}$$

$S_w =$ 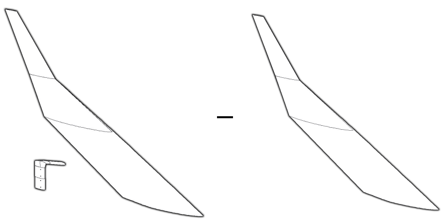 (A.6)

Then, these newly defined forces acting on the engine strut are subtracted from the wing-on measurements of TFN and engine in the following way (Equations A.7, A.8, A.9 and A.10) resulting in the forces and moments acting on the Wing/TFN and Wing/Engine combinations.

$$WN = WNS - S_w = WNS - (WS - W) \tag{A.7}$$

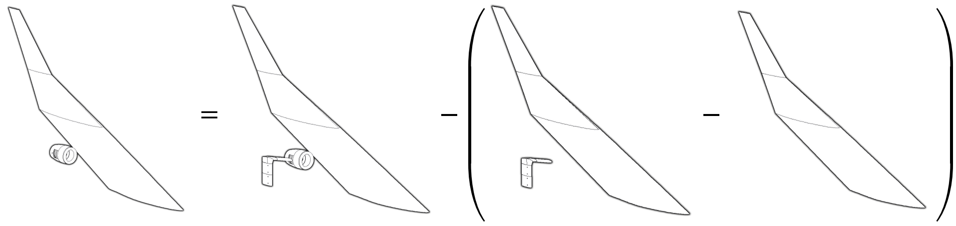

(A.8)

$$WEN = WENS - S_w = WENS - (WS - W) \tag{A.9}$$

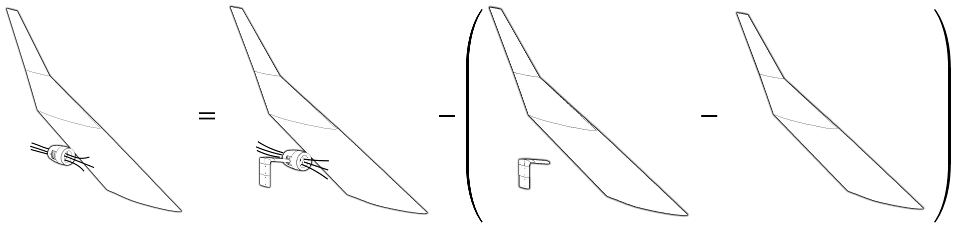

(A.10)

Installation and Integration Definitions

Combining the previously determined definitions, it is possible to obtain the installation and interference effects of the wing, nacelle and jet. The installation effect at TFN conditions is defined as the addition drag due to the installation of the engine at flow-through nacelle (idle) conditions.

Installation Effects

The installation effect of a nacelle or propulsion system is defined as the measurements of wing and engine, minus the measurements of the isolated wing. It can be subdivided into the installation effect of the nacelle (A.11, A.12) and the addition of thrust (A.13, A.14). Together they form the total installation effect of the engine (A.15, A.16).

Installation Nacelle

$$I_N = WN - W \tag{A.11}$$

$I_N =$

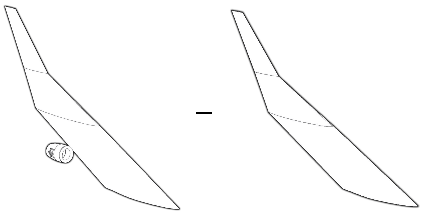

(A.12)

Installation Jet

$$I_E = WEN - WN \tag{A.13}$$

$I_E =$

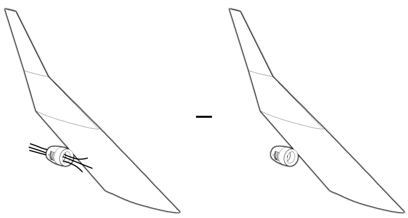

(A.14)

Installation Engine

$$I_P = WEN - W = I_N + I_E \tag{A.15}$$

$I_P =$ 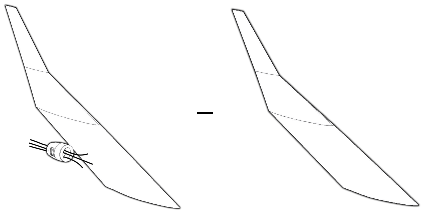 (A.16)

Interference effects

The interference effects of a nacelle or propulsion system are defined as the difference between the installed system and the measurements of the isolated components. It can be subdivided into the interference effect of the nacelle (A.17, A.18) and the interference effect of the jet (A.19, A.20). Addition results in the interference effect of the engine (A.21,A.22).

Nacelle Interference

$$If_N = WN - (W + N) \tag{A.17}$$

$If_N =$ 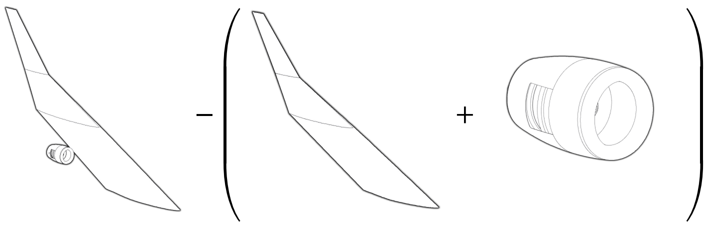 (A.18)

Jet Interference Effect

$$If_E = (WEN - WN) - (EN - N) \tag{A.19}$$

$If_E =$ 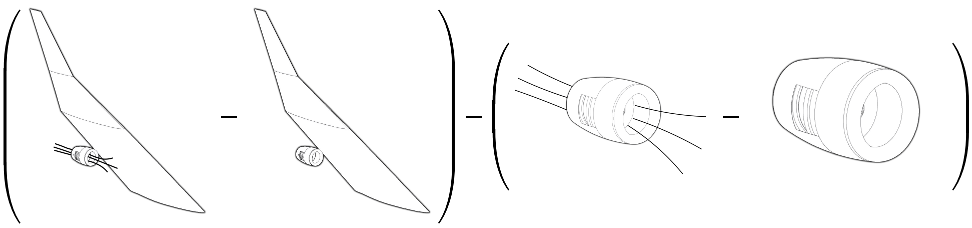 (A.20)

Engine Interference

$$If_P = WEN - (W + EN) \tag{A.21}$$

$If_P =$ 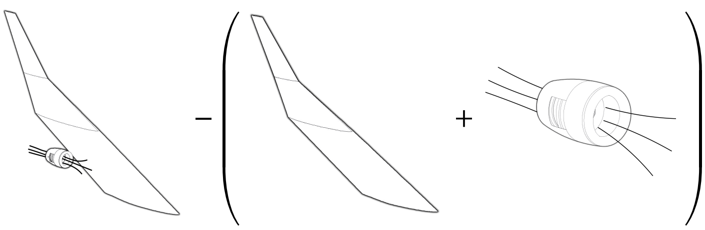 (A.22)

B

Measurement Precision

Addition of this section is mainly meant to show the precision of all recorded values, as well as the non-dimensional forces and moments generated by individual measurements that do not deserve a designated place in the main body of this work. To this end, plots are shown of all the domains of recorded values, with a confidence interval of three times the sample standard deviation ($3s$) at each measurement point.

The largest standard deviations recorded in all measurement sets are summarized in the tables below. For unpowered testing conditions:

Maximum Standard Deviation (α = [-5,30])	C_L	C_D	C_M
W	0.00336	0.00161	0.00120
S	0.00054	0.00017	0.00021
WS	0.00481	0.00115	0.00155
NS	0.00066	0.00031	0.00049
WNS	0.00417	0.00157	0.00174

For powered testing domains the maximum recorded standard deviations are:

Maximum Standard Deviation (α = [-5,30], J = [0.37,1.13])	C_L	C_D	C_M
ENS	0.00622	0.00379	0.00423
WENS	0.00914	0.00712	0.00833

Whilst the addition of thrust does increase the sample standard deviation somewhat, it is encouraging to see that the maximum observed standard deviation is of the same order of magnitude as the unpowered measurements. The rest of the figures in this Appendix are for the readers reference. It can be noted that in most cases, the average standard deviation of the set are significantly lower than the largest recorded value. The contour plots on Figures B.6a up to B.7c, show that at most measurement points, the sample standard deviation is around 10-20 counts for all values. This observation allows the setup to be used for engine interference measurements without the addition of an encoder for more accurate thrust setpoints.

Wing (W)

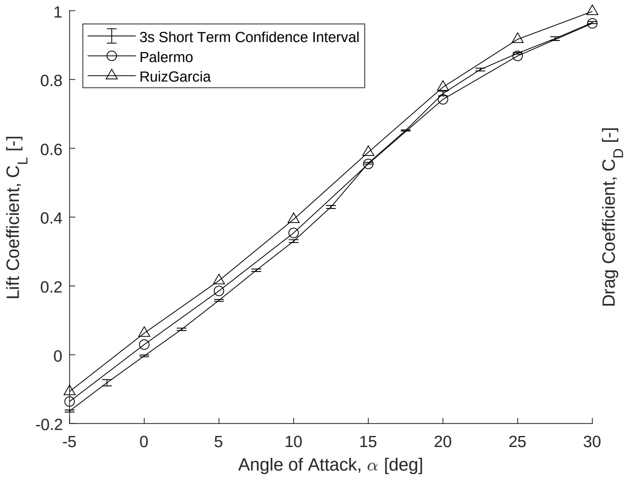

(a) W short term repeatability confidence interval (C_L)

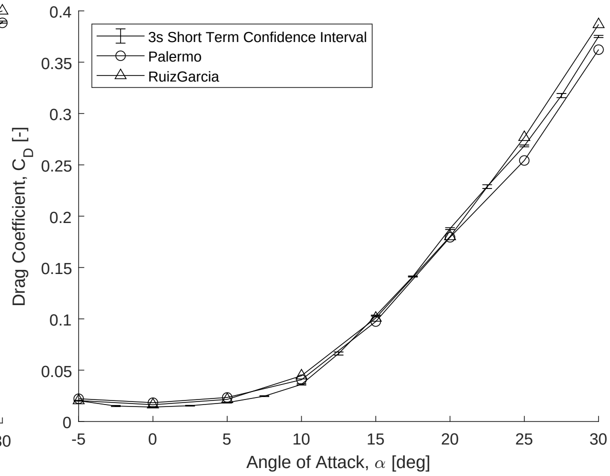

(b) W short term repeatability confidence interval (C_D)

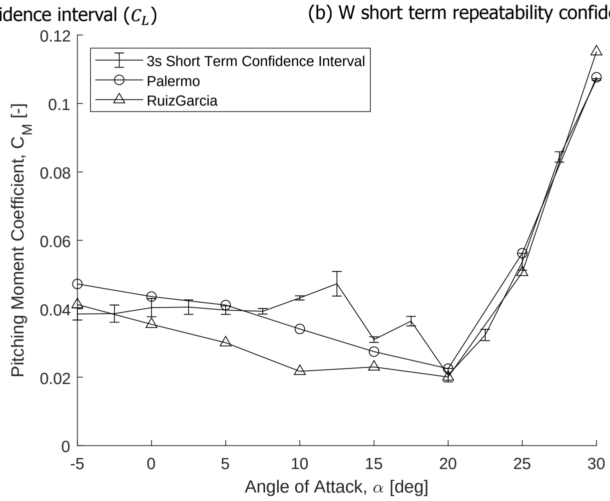

(c) W short term repeatability confidence interval (C_M)

Engine Strut (S)

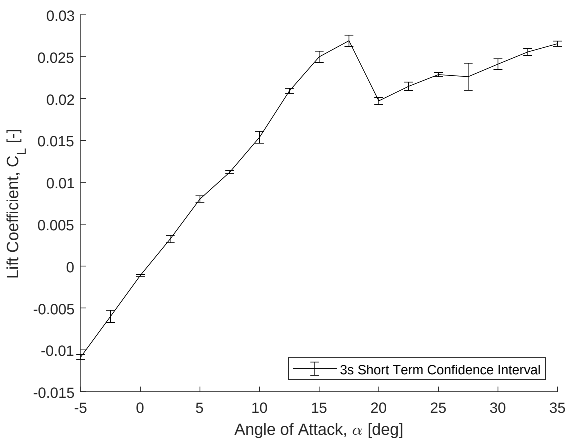

(a) S short term repeatability confidence interval (C_L)

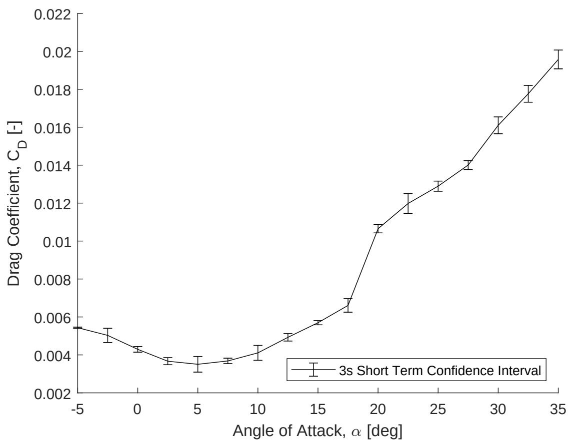

(b) S short term repeatability confidence interval (C_D)

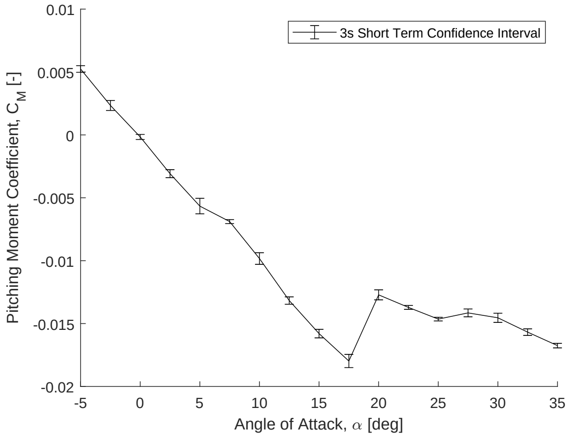

(c) S short term repeatability confidence interval (C_M)

Wing + Strut (WS)

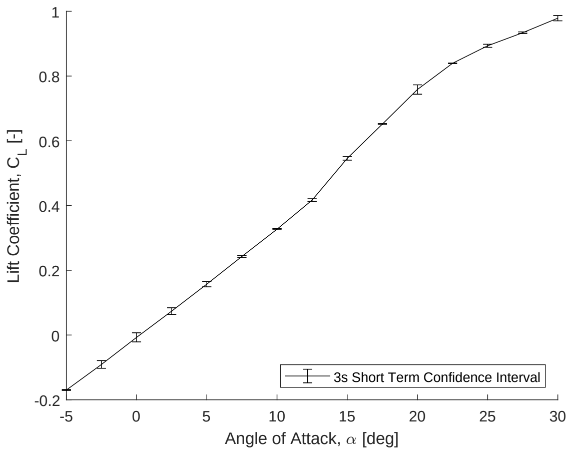

(a) WS short term repeatability confidence interval (C_L)

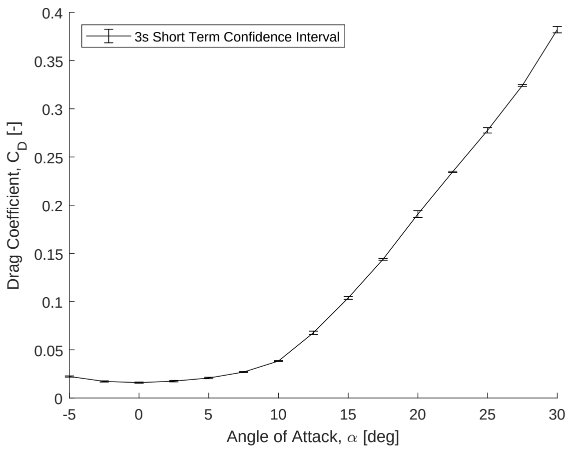

(b) WS short term repeatability confidence interval (C_D)

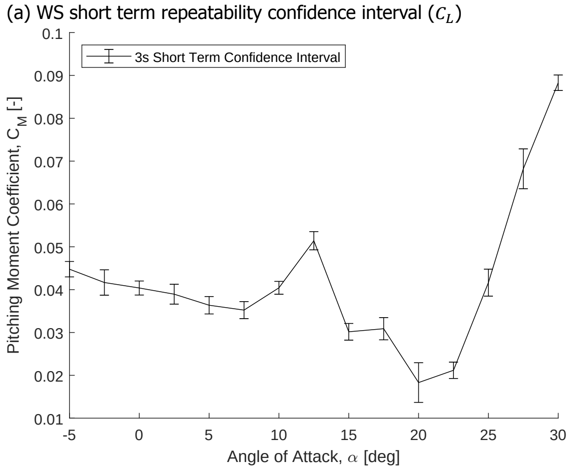

(c) WS short term repeatability confidence interval (C_M)

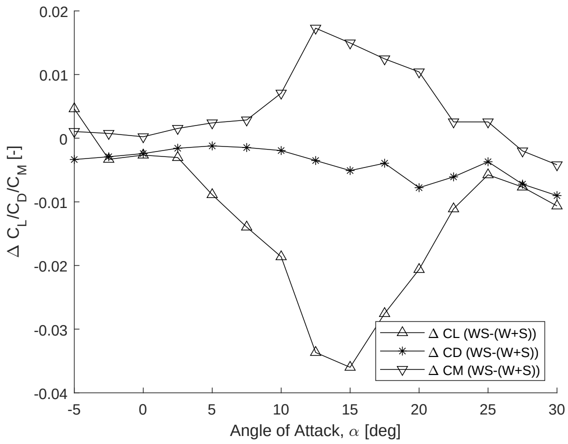

(d) Interference effects between the wing and strut (WS-(W+S))

Measurements of WS and comparison with W+S reveal that the wing has a non negligible effect on the engine strut used in the experiment, which has to be accounted for in further results. The interference effects are displayed in Figure B.3d. The choice was made to account the deltas between WS and W+S fully to the strut in all other Wing-on results.

The main reasoning behind this, is that the circulation of the wing has a large influence of the angle of attack experienced by the strut, reducing the angle and therefore the lift it generates. The delta between WS and W+S reveals that dCD is relatively constant between Wing on and Wing off. Though, the lift of the strut is almost negligible due to the wake of the wing up to moderate angles of attack.

Nacelle + Strut (NS)

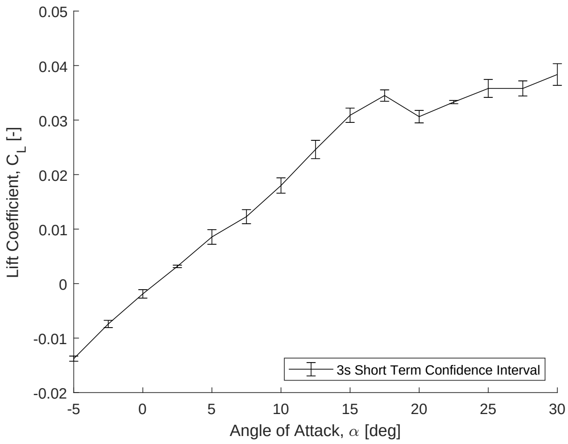

(a) NS short term repeatability confidence interval (C_L)

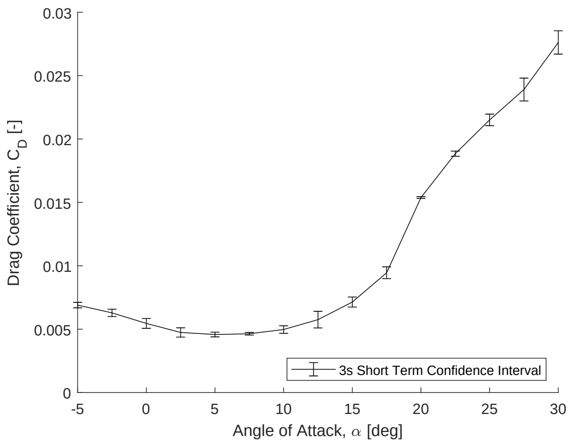

(b) NS short term repeatability confidence interval (C_D)

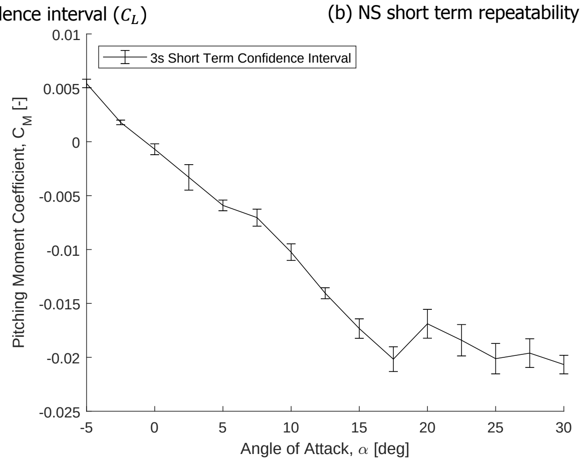

(c) NS short term repeatability confidence interval (C_M)

Wing + Nacelle + Strut (WNS)

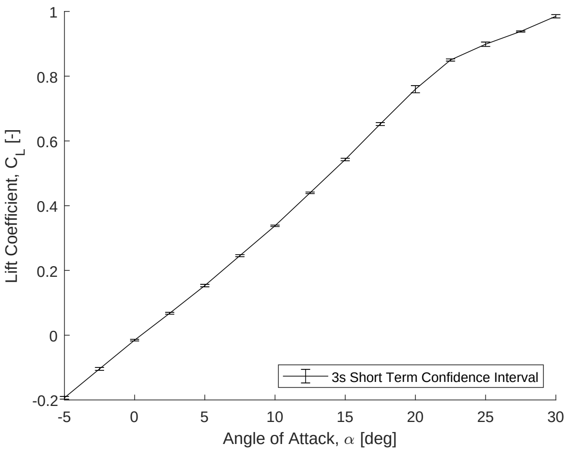

(a) WNS short term repeatability confidence interval (C_L)

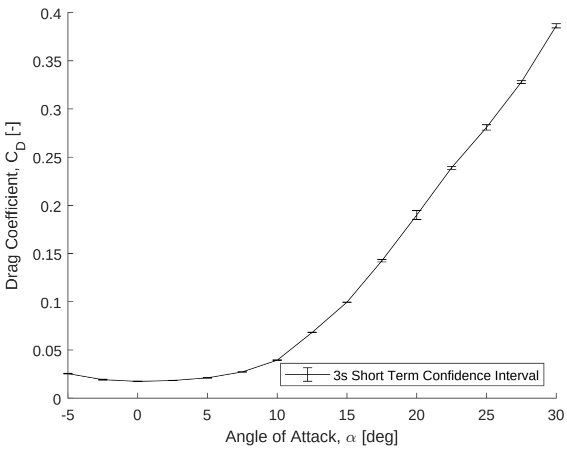

(b) WNS short term repeatability confidence interval (C_D)

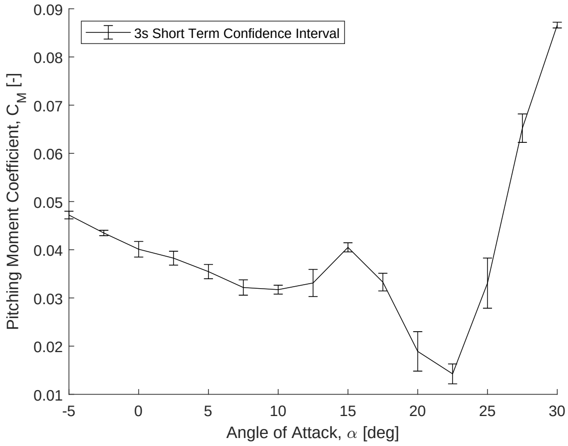

(c) WNS short term repeatability confidence interval (C_M)

Engine + Nacelle + Strut (ENS)

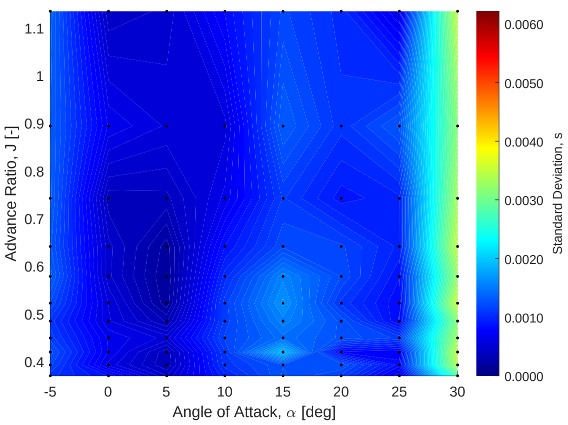

(a) ENS short term repeatability confidence interval (C_L)

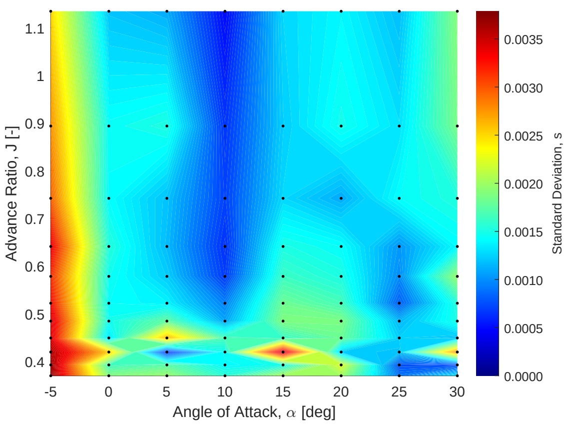

(b) ENS short term repeatability confidence interval (C_D)

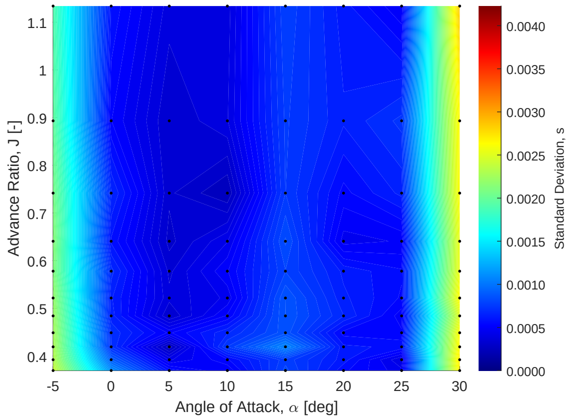

(c) ENS short term repeatability confidence interval (C_M)

Wing + Engine + Nacelle + Strut (WENS)

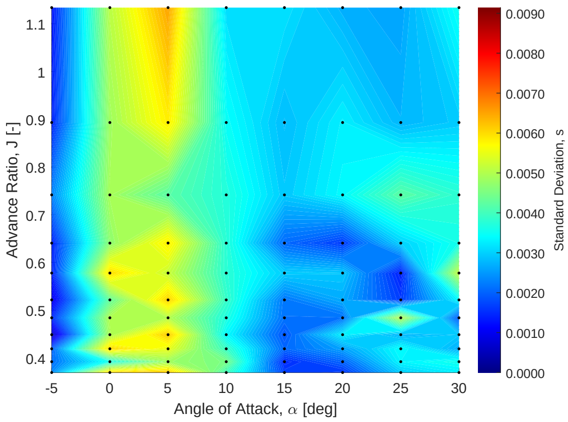

(a) WENS short term repeatability confidence interval (C_L)

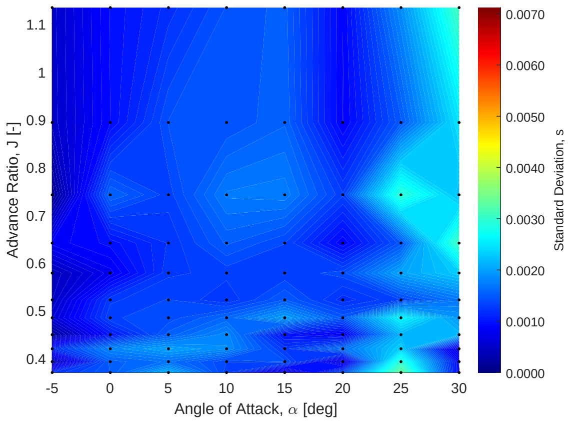

(b) WENS short term repeatability confidence interval (C_D)

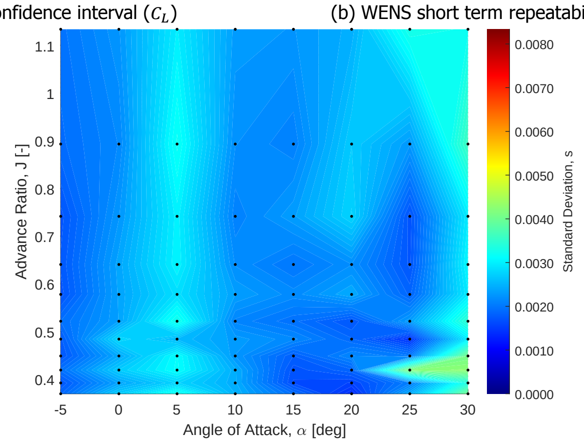

(c) WENS short term repeatability confidence interval (C_M)

C
Engine Data

Some averaged engine data recorded by the ESC is presented in the table below. The recorded value for the fan speed was verified to be accurate using a stroboscope. Comparing multiple runs also confirmed that fan speed is quite constant for an input PWM duty cyle %, even for varying free stream velocities. However, values for current and power varied quite significantly depending on the temperature of the motor and its controller. Thus, the setup can be effectively used for balance measurements, but no observations can be made regarding the efficiency of energy conversion for a test condition.

V = 15							
PWM %	ESC %	Speed [x100 rpm]	Current [A]	Power [W]	Thrust [N]	T_C	Advance Ratio J [-]
20	18.63	88.02	3.27	163.6	1.86	0.0147	0.8490
25	24.51	112.22	6.57	328.6	4.14	0.0328	0.6688
30	29.41	134.34	9.23	461.5	6.76	0.0536	0.5554
35	35.29	155.75	14.10	704.9	10.17	0.0805	0.4799
40	40.20	172.58	18.62	930.8	13.44	0.1064	0.433
45	45.10	189.34	23.90	1194.9	17.02	0.1348	0.3908
50	50.98	207.01	30.60	1529.9	20.79	0.1645	0.3628
55	55.88	222.54	37.76	1888.2	24.76	0.1958	0.3363
60	61.77	238.95	46.92	2346.2	28.96	0.2288	0.3143
65	67.65	253.22	55.65	2782.3	33.85	0.2674	0.2941
70	72.55	268.72	67.17	3358.3	38.79	0.3062	0.2771

V= 20							
PWM %	ESC %	Speed [x100 rpm]	Current [A]	Power [W]	Thrust [N]	T_C	Advance Ratio J [-]
20	18.63	88.69	3.64	181.8	0.78	0.0037	1.1147
25	24.51	112.88	6.24	312.1	2.65	0.0122	0.8781
30	29.41	134.61	8.90	444.9	5.14	0.0238	0.7289
35	35.29	156.52	13.75	687.5	8.25	0.0381	0.6297
40	40.20	173.82	18.46	922.9	11.18	0.0517	0.5681
45	45.10	190.25	23.58	1179.1	14.39	0.0665	0.5129
50	50.98	207.10	30.10	1505.1	18.06	0.0834	0.4763
55	55.88	222.78	37.90	1895.0	21.8271	0.1007	0.4416
60	61.77	236.12	46.04	2301.9	25.83	0.1191	0.4126
65	67.65	253.86	56.08	2804.1	30.41	0.1403	0.3860
70	72.55	268.80	66.79	3339.4	35.02	0.1615	0.3636

D

Intake Data

This Appendix is added to provide the basic measurement results in terms of total pressure (P_0/P_{0_∞}) for the inlet rake measurements. From the wing-off measurements it can be seen that free-stream total pressure is nicely recovered. Only some inlet lip separation can be observed on the lower inlet lip from Figure D.1c. Even the improved pressure gradient in close-to-idle conditions is enough to ensure attached flow with the engine installed.

Wing-Off

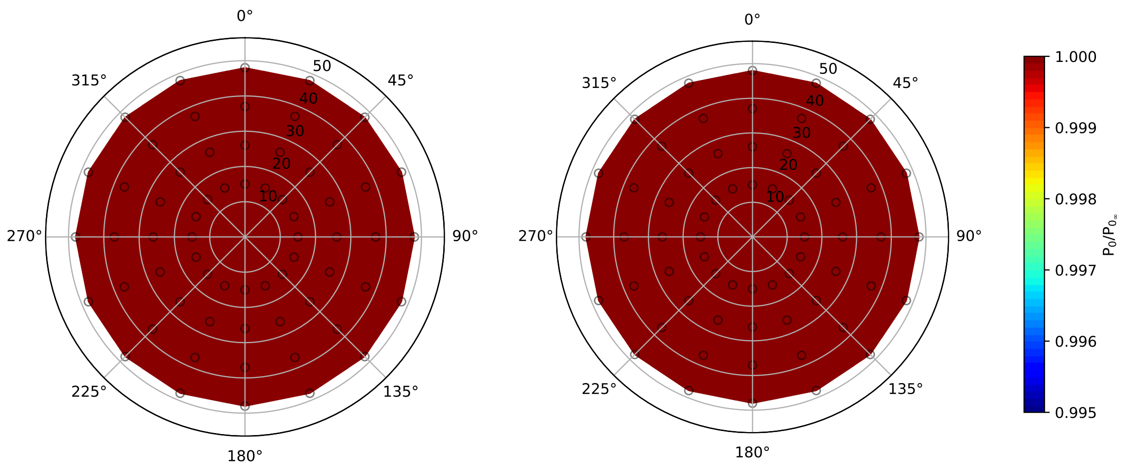

(a) $V_\infty = 20m/s$, $\alpha = 5°$, TFN

(b) $V_\infty = 20m/s$, $\alpha = 15°$, TFN

Figure D.1: Inlet pressure measurements of the nacelle in wing-off conditions

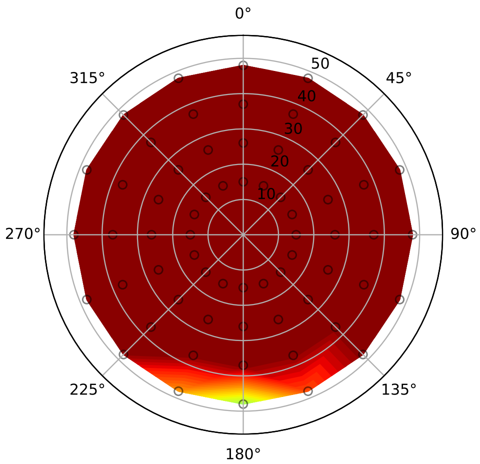

(c) $V_\infty = 20m/s$, $\alpha = 25^\circ$, TFN

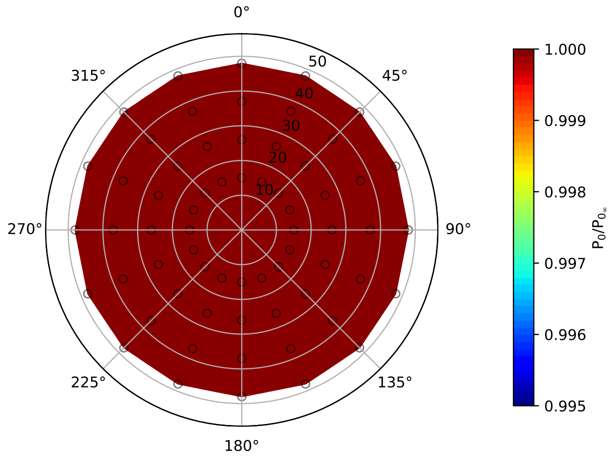

(d) $V_\infty = 20m/s$, $\alpha = 5^\circ$, Power:Idle

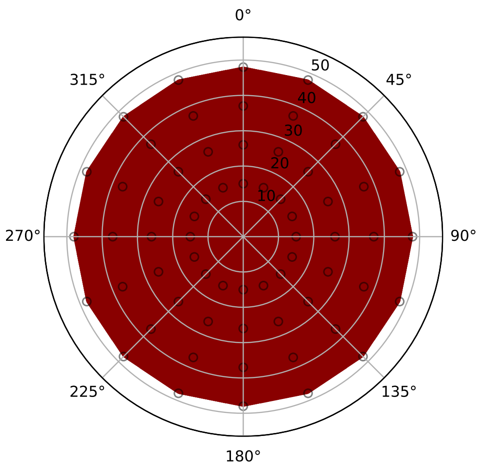

(e) $V_\infty = 20m/s$, $\alpha = 15^\circ$, Power:Idle

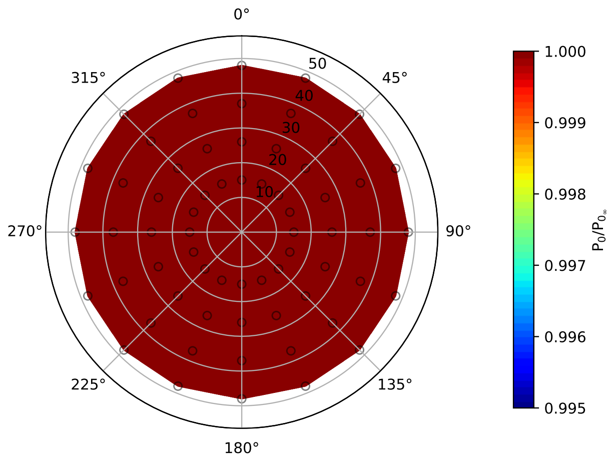

(f) $V_\infty = 20m/s$, $\alpha = 25^\circ$, Power:Idle

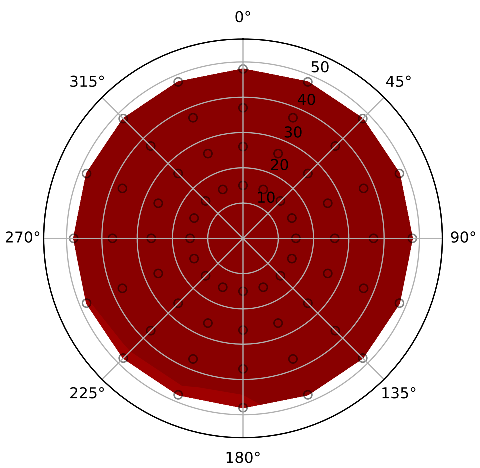

(g) $V_\infty = 20m/s$, $\alpha = 5^\circ$, Power:On

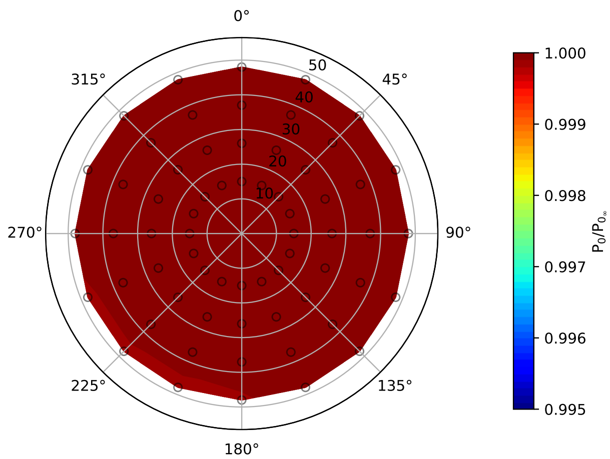

(h) $V_\infty = 20m/s$, $\alpha = 15^\circ$, Power:On

Figure D.1: Inlet pressure measurements of the nacelle in wing-off conditions, Continued

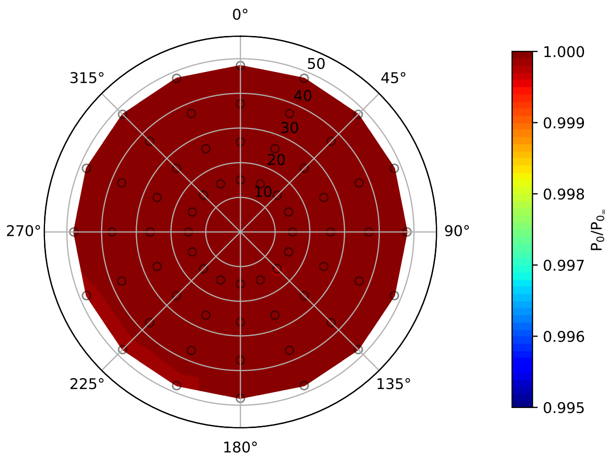

(i) $V_\infty = 20m/s$, $\alpha = 25°$, Power:On

Figure D.1: Inlet pressure measurements of the nacelle in wing-off conditions, Continued

Wing-On 20m/s

Total pressure loss in the wing-on configuration is treated in the main body of this work. While also available there, the following measurement results are added to this Appendix for completeness.

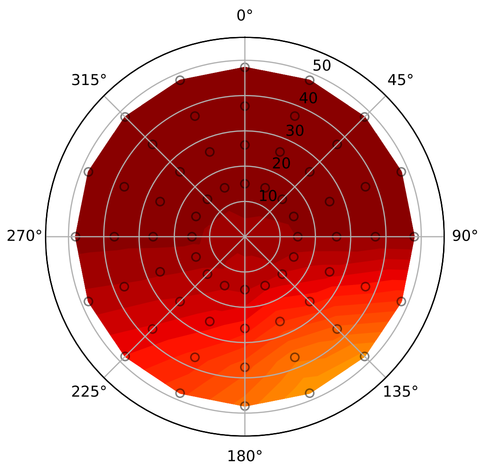

(a) $V_\infty = 20m/s$, $\alpha = 5°$, TFN

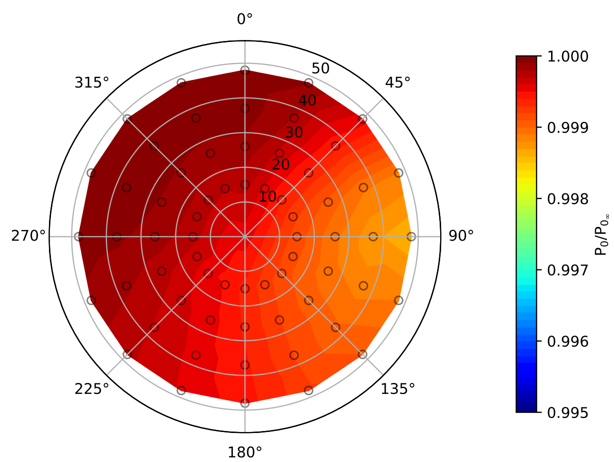

(b) $V_\infty = 20m/s$, $\alpha = 15°$, TFN

Figure D.2: Inlet pressure measurements of the nacelle in wing-on conditions

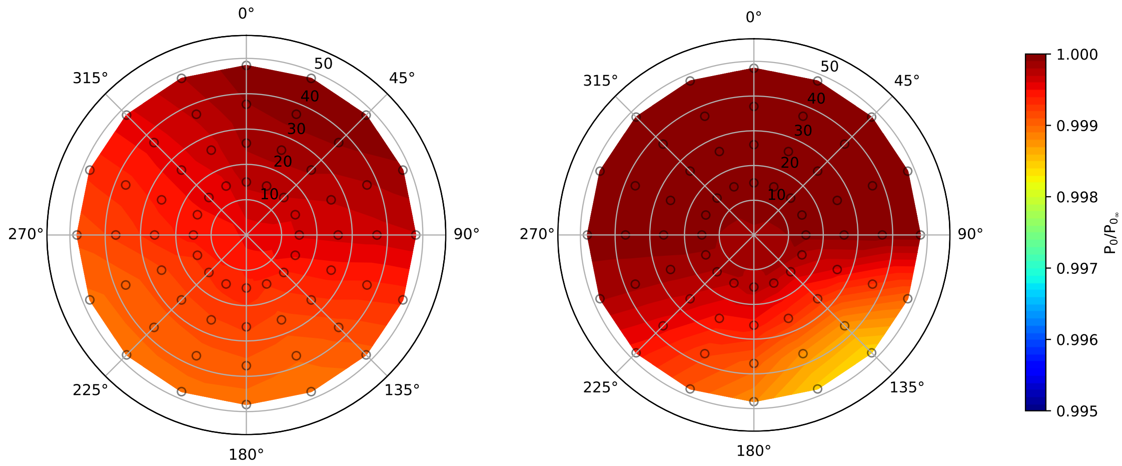

(c) $V_\infty = 20m/s$, $\alpha = 25^\circ$, TFN

(d) $V_\infty = 20m/s$, $\alpha = 5^\circ$, Power: Idle

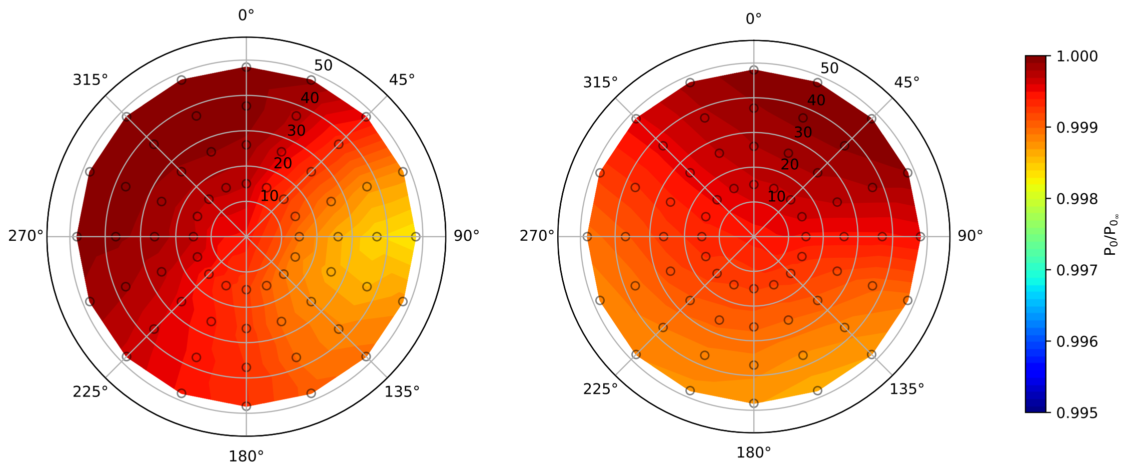

(e) $V_\infty = 20m/s$, $\alpha = 15^\circ$, Power: Idle

(f) $V_\infty = 20m/s$, $\alpha = 25^\circ$, Power: Idle

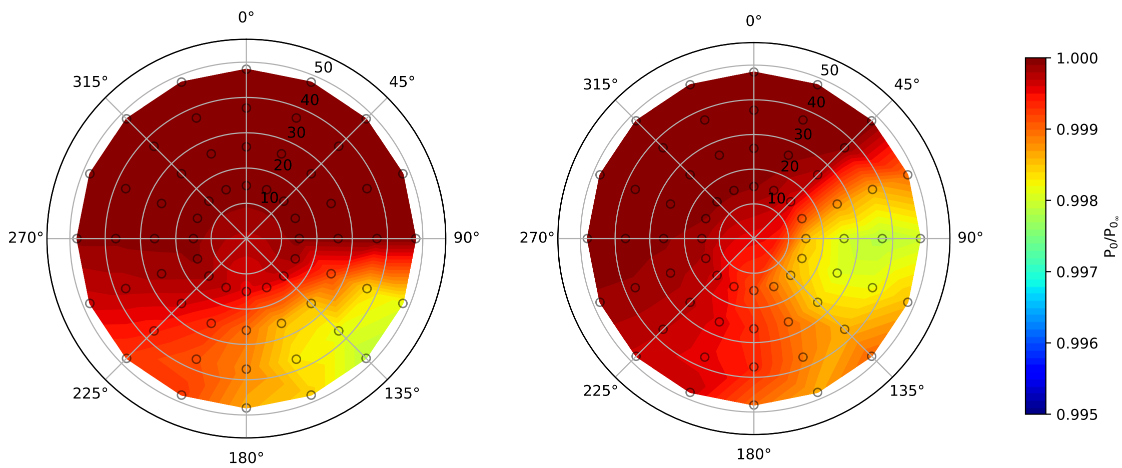

(g) $V_\infty = 20m/s$, $\alpha = 5^\circ$, Power: On

(h) $V_\infty = 20m/s$, $\alpha = 15^\circ$, Power: On

Figure D.2: Inlet pressure measurements of the nacelle in wing-on conditions, Continued

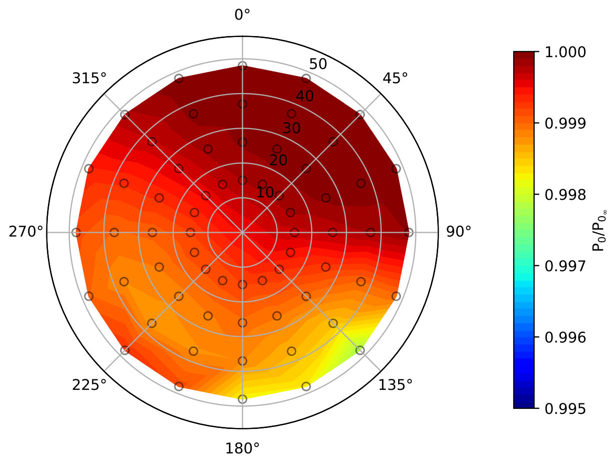

(i) $V_\infty = 20m/s$, $\alpha = 25°$, Power: On

Figure D.2: Inlet pressure measurements of the nacelle in wing-on conditions, Continued

Wing-On 30m/s

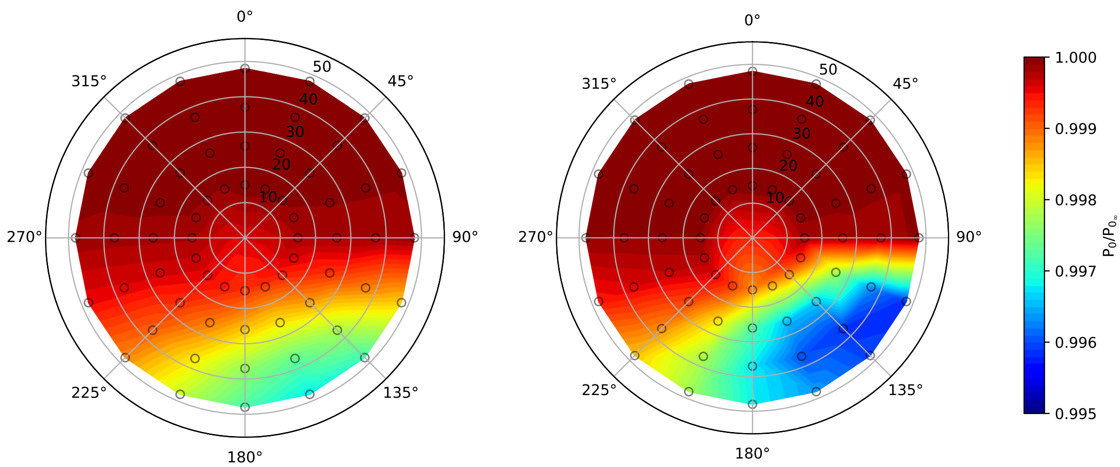

(a) $V_\infty = 30m/s$, $\alpha = 5°$, Power: Idle

(b) $V_\infty = 30m/s$, $\alpha = 5°$, Power: On

Figure D.3: Inlet pressure measurements of the nacelle in wing-on conditions ($V_\infty = 30m/s$), Continued

E

Test Matrix

Balance Measurements

Alpha [deg]	Tested Hardware Combinations	Velocity [m/s]
-5	W, WS, WNS, S, NS	15/20
-2.5	W, WS, WNS, S, NS	15/20
0	W, WS, WNS, S, NS	15/20
2.5	W, WS, WNS, S, NS	15/20
5	W, WS, WNS, S, NS	15/20
7.5	W, WS, WNS, S, NS	15/20
10	W, WS, WNS, S, NS	15/20
12.5	W, WS, WNS, S, NS	15/20
15	W, WS, WNS, S, NS	15/20
17.5	W, WS, WNS, S, NS	15/20
20	W, WS, WNS, S, NS	15/20
22.5	W, WS, WNS, S, NS	15/20
25	W, WS, WNS, S, NS	15/20
27.5	W, WS, WNS, S, NS	15/20
30	W, WS, WNS, S, NS	15/20

Alpha [deg]	Tested Hardware Combinations [% PWM Duty Cycle Setpoints]	Velocity [m/s]
-5	WENS/ENS [20 ,25, 30, 35, 40, 45, 50, 55, 60, 65, 70]	15/20
0	WENS/ENS [20 ,25, 30, 35, 40, 45, 50, 55, 60, 65, 70]	15/20
5	WENS/ENS [20 ,25, 30, 35, 40, 45, 50, 55, 60, 65, 70]	15/20
10	WENS/ENS [20 ,25, 30, 35, 40, 45, 50, 55, 60, 65, 70]	15/20
15	WENS/ENS [20 ,25, 30, 35, 40, 45, 50, 55, 60, 65, 70]	15/20
20	WENS/ENS [20 ,25, 30, 35, 40, 45, 50, 55, 60, 65, 70]	15/20
25	WENS/ENS [20 ,25, 30, 35, 40, 45, 50, 55, 60, 65, 70]	15/20
30	WENS/ENS [20 ,25, 30, 35, 40, 45, 50, 55, 60, 65, 70]	15/20

Intake Pressure Measurements

Alpha [deg]	Tested Hardware Combinations [% PWM Duty Cycle Setpoint]	Velocity [m/s]
5	WENS [20,70]	30
5	WENS/ENS/NS/WNS [20,70]	20
15	WENS/ENS/NS/WNS [20,70]	20
25	WENS/ENS/NS/WNS [20,70]	20

Bibliography

[1] Torenbeek, E., *Advanced Aircraft Design*, 2013.

[2] Benad, J., "THE FLYING V - A NEW AIRCRAFT CONFIGURATION FOR COMMERCIAL PASSENGER TRANSPORT," *Deutscher Luft- und Raumfahrtkongress*, 2015, pp. 1–8.

[3] Faggiano, F., Vos, R., Baan, M., and Van Dijk, R., "Aerodynamic design of a flying V aircraft," *17th AIAA Aviation Technology, Integration, and Operations Conference, 2017*, 2017.

[4] Martinez-Val, R., "Flying Wings. A New Paradigm for Civil Aviation?" *Acta Polytechnica*, Vol. 47, No. 1, 2007.

[5] Van Der Schaft, L. A., "Development, Model Generation and Analysis of a Flying V Structure Concept," 2017.

[6] Vicroy, D., "X-48B Blended Wing Body Ground to Flight Correlation Update," 2011.

[7] Van Gorcum, J. J., *Ready For Take-off: Scaled Flight Testing (MSc Thesis)*, Delft University of Technology, 2017.

[8] Pettersson, K. and Rizzi, A., "Aerodynamic scaling to free flight conditions: Past and present," *Progress in Aerospace Sciences*, Vol. 44, No. 4, 2008, pp. 295–313.

[9] Vicroy, D. D., Dickey, E., Princen, N., Beyar, M. D., Researcher, S., Branch, F. D., Fellow, A., Engineer, S., Technology, V., Engineer, S., Control, V., Technology, V., Engineer, A., and Technology, V., "Overview of Low-speed Aerodynamic Tests on a 5.75% Scale Blended-Wing-Body Twin Jet Configuration," 2016.

[10] Palermo, M., *The Longitudinal Static Stability and Control Characteristics of a Flying V Scaled Model: An Experimental and Numerical Investigation (MSc Thesis)*, Delft University of Technology, 2019.

[11] Viet, R. A., *Analysis of the flight characteristics of a highly swept cranked flying wing by means of an experimental test (MSc Thesis)*, Delft University of Technology, 2019.

[12] Ruiz Garcia, A., *Aerodynamic Model Identification of the Flying V using Wind Tunnel Data (MSc Thesis)*, Delft University of Technology, 2019.

[13] Rubio Pascual, B., *Engine-Airframe Integration for the Flying V (MSc Thesis)*, Delft University of Technology, 2018.

[14] BLACK, D. and ROHRBACH, C., "Shrouded propellers - A comprehensive performance study," , No. 68, 1968.

[15] Graf, W. E., *Effects of Duct Lip Shaping and Various Control Devices on the Hover and Forward Flight Performance of Ducted Fan UAVs*, Ph.D. thesis, Virginia Polytechnic Institute and State University, 2005.

[16] Lv, P., Rao, A. G., Ragni, D., and Veldhuis, L., "Performance analysis of wake and boundary-layer ingestion for aircraft design," *Journal of Aircraft*, Vol. 53, No. 5, 2016, pp. 1517–1526.

[17] Mendenhall, M. and Spangler, S., "Theoretical Study of Ducted Fan Performance," 1970.

[18] Trancossi, M. and Madonia, M., "The efficiency of an electric turbofan vs. inlet area: A simple mathematical model and CFD simulations," *SAE Technical Papers*, Vol. 10, No. November 2016, 2012.

[19] Hennecke, M., Moore, R., and Swan, H., "Performance of Propellers," .

[20] Hill, G. A. and Kandil, O. A., "Aerodynamic investigations of an advanced over-the-wing nacelle transport aircraft configuration," *Collection of Technical Papers - 45th AIAA Aerospace Sciences Meeting*, Vol. 12, No. January, 2007, pp. 8124–8139.

[21] Savoni, L., Rudnik, R., Ronzheimer, A., and Heykena, C., "High lift design and aerodynamic assessment for an over-the-wing pylon-mounted engine configuration with STOL capabilities," *2018 Applied Aerodynamics Conference*, 2018, pp. 1–13.

[22] White, F., *Viscous Fluid Flow*, McGraw-Hill, 3rd ed., 2006.

[23] Sabo, K. and Drela, M., "Benefits of boundary layer ingestion propulsion," *53rd AIAA Aerospace Sciences Meeting*, , No. January, 2015, pp. 1–14.

[24] Hall, D. K., Huang, A. C., Uranga, A., Greitzer, E. M., Drela, M., and Sato, S., "Boundary layer ingestion propulsion benefit for transport aircraft," *Journal of Propulsion and Power*, Vol. 33, No. 5, 2017, pp. 1118–1129.

[25] Liebeck, R. H., "Design of the Blended Wing Body Subsonic Transport," *Journal of Aircraft*, Vol. 41, No. 1, 2004, pp. 10–25.

[26] Dickey, E. D., Princen, N. H., Bonet, J. T., and Ige, G. K., "Wind tunnel model design and fabrication of a 5.75% scale blended-wing-body twin jet configuration," *54th AIAA Aerospace Sciences Meeting*, , No. January, 2016, pp. 1–24.

[27] Kawai, R. T., Friedman, D. M., and Serrano, L., "Blended Wing Body (BWB) Boundary Layer Ingestion (BLI) inlet configuration and system studies," *NASA Contract Report*, Vol. 214534, No. December, 2006, pp. 1–26.

[28] Sóbester, A., "Tradeoffs in jet inlet design: A historical perspective," *Journal of Aircraft*, Vol. 44, No. 3, 2007, pp. 705–717.

[29] Cavcar, M., "Blade Element Theory," 2004.

[30] Bugajski, G. T., Pečinka, J., Jílek, A., and Kmoch, P., "TJ100 inlet distortion testing," *ICMT 2015 - International Conference on Military Technologies 2015*, , No. 1, 2015.

[31] SAE, "SAE-ARP-1420-B-Gas Turbine Engine Inlet Flow Distortion Guidelines," 1978.

[32] Seddon, J. and Goldsmith, E., *Intake Aerodynamics*, Collins Professional and Technical Books, 1985.

[33] Yildirim, A., Gray, J. S., Mader, C. A., and Martins, J., "Aeropropulsive Design Optimization of a Boundary Layer Ingestion System," , No. June, 2019, pp. 1–17.

[34] Morrison, G. L., Schobeiri, M. T., and Pappu, K. R., "Five-hole pressure probe analysis technique," *Flow Measurement and Instrumentation*, Vol. 9, No. 3, 1998, pp. 153–158.

[35] Schuh, M. J., Garcia, J. A., Carter, M. B., Deere, K. A., Stremel, P. M., and Tompkins, D. M., "NASA environmentally responsible aviation hybrid wing body flow-through nacelle wind tunnel CFD," *54th AIAA Aerospace Sciences Meeting*, 2016.

[36] Hoheisel, H., "Aerodynamic Aspects of Engine-Aircraft Integration of Transport Aircraft," *Aerospace Science and Technology*, Vol. 1, No. 7, 1997, pp. 475–487.

[37] Hoheisel, H., Frhr, H., and Geyr, V., "The influence of engine thrust behaviour on the aerodynamics of engine airframe integration," *CEAS Aeronautical Journal*, Vol. 3, No. 1, 2012, pp. 79–92.

[38] Kooi, J. W., de Haij, L., and Hegen, G. H., "Engine simulation with turbofan powered simulators in the german-dutch wind tunnels," *22nd AIAA Aerodynamic Measurement Technology and Ground Testing Conference*, , No. June, 2002, pp. 1–12.

[39] Hegen, G. H. and R, K., "Experiences with ultra-high bypass simulators from calibration and isolated engine testing," *International Forum on Turbine Powered Simulation*, 1995.

[40] Harris, A. E. and Paliwal, K. C., "Civil Turbofan Propulsion System Integration Studies Using Powered Testing Techniques At Ara, Bedford," *AIAA Paper*, 1984, pp. 74–98.

[41] Burgsmüller, W. and Hoheisel, H., "ENIFAIR — EU research into engine integration on future transport aircraft," *Air & Space Europe*, Vol. 2, No. 2, 2000, pp. 81–85.

[42] Campomanes, C. S., *External Flow Effects in the Engine/Airframe Integration Testing Technique A new Thrust/Drag Bookkeeping Approach at the German-Dutch Wind Tunnels (MSc Thesis)*, Delft University of Technology.

[43] J.B. Barlow, W.H. Rae, A. P., *Low-Speed Wind Tunnel Testing*, John Wiley & Sons Inc, 3rd ed., 1999.

[44] Garner, H., Rogers, E., Acum, W., and Maskell, E., "Subsonic Wind Tunnel Wall Corrections (AGARDograph 109)," 1966.

[45] Krynytzky, A. and Ewald, B., "Conventional Wall Corrections for Closed and Open Test Sections - AGARDograph 336 Chapter 2," .

[46] Horsten, B. J. and Veldhuis, L. L., "A new hybrid method to correct for wind tunnel wall- and support interference on-line," *World Academy of Science, Engineering and Technology*, Vol. 58, No. 2, 2009, pp. 507–514.

[47] Mokhtar, W. A. and Britcher, C. P., "Boundary interference assessment and correction for open test section wind tunnels using panel methods," *AIAA Paper*, , No. January, 2004, pp. 5927–5941.

[48] Mokhtar, W. A. and Britcher, C. P., "Wind-tunnel boundary corrections for a full-scale 1903 wright flyer replica," *Journal of Aircraft*, Vol. 43, No. 1, 2006, pp. 64–71.

[49] Kriegsman, R. and Reede, B., "Aerospace Engineering: The Open Jet Facility," 2016.

[50] Wolowicz, C. H. and Bowman, J. S., "NASA Technical Paper 1435 Similitude Requirements and Scaling Relationships as Applied to Model Testing," , No. August, 1979.

[51] Eder, S., Hufnagel, K., and Tropea, C., "SEMI-SPAN TESTING IN WIND TUNNELS," , pp. 1–9.

[52] Skinner, S. N. and Zare-Behtash, H., "Semi-span wind tunnel testing without conventional peniche," *Experiments in Fluids*, Vol. 58, No. 12, 2017, pp. 1–18.

[53] Yu, W., Hong, V. W., Ferreira, C., and van Kuik, G. A., "Experimental analysis on the dynamic wake of an actuator disc undergoing transient loads," *Experiments in Fluids*, Vol. 58, No. 10, 2017.

[54] Lacey, M., "Statistical Topics (Yale) http://www.stat.yale.edu/Courses/1997-98/101/stat101.htm," 1997.

[55] Jones, R. T. and Cohen, D., "High Speed Wing Theory," 1960.

[56] Walter, S. F. and Starkey, R. P., "Interpolation methods for inlet distortion determination," *54th AIAA Aerospace Sciences Meeting*, , No. January, 2016, pp. 1–13.

[57] Ruijgrok, G. J. J., "Elements of Airplane Performance," *VSSD*, 2009.